AD NUMBER

AD055205

NEW LIMITATION CHANGE

TO

Approved for public release, distribution unlimited

FROM

Distribution authorized to U.S. Gov't. agencies and their contractors; Administrative/Operational Use; Nov 1954. Other requests shall be referred to Director, Wright Air Development Center, Wright-Patterson AFB, OH 45433.

AUTHORITY

AFAL ltr, 17 Aug 1979

Unclassified
~~CONFIDENTIAL~~

WADC TECHNICAL REPORT 53-161
PART 2
AD0055205

UNCLASSIFIED

(Title -- UNCLASSIFIED)

SUBSONIC FLUTTER MODEL TESTS OF WINGS CARRYING HEAVY TIP PODS

Part 2. Swept Wings

W. G. BRADY

H. G. MAIER

WALTER P. TARGOFF

CORNELL AERONAUTICAL LABORATORY, INC.

20030708012

NOVEMBER 1954

WRIGHT AIR DEVELOPMENT CENTER

~~CONFIDENTIAL~~

54WCLSA-416-3

UNCLASSIFIED

**Statement A
Approved for Public Release**

NOTICE

When Government drawings, specifications, or other data are used
for any purpose other than in connection with a definitely related Govern-
ment procurement operation, the United States Government   thereby in-
curs no responsibility nor any obligation whatsoever; and the   fact   that
the Government may have formulated, furnished, or in any way supplied
the said drawings, specifications, or other data, is not to be regarded
by implication or otherwise as in any manner licensing the holder   or
any other person or corporation, or conveying any rights or permission
to manufacture, use, or sell any patented invention that may in any   way
be related thereto.

(Title -- UNCLASSIFIED)

SUBSONIC FLUTTER MODEL TESTS OF WINGS CARRYING HEAVY TIP PODS

Part 2. Swept Wings

W. G. Brady
H. G. Maier
Walter P. Targoff

Cornell Aeronautical Laboratory, Inc.

November 1954

Wright Air Development Center
Air Research and Development Command
United States Air Force
Wright-Patterson Air Force Base, Ohio

54WCLSA-416 -3

FOREWORD

The research described in this report was conducted by the Cornell Aeronautical Laboratory, Inc., Buffalo, New York under U.S. Air Force Contract No. AF33(038)-3551.

This project is part of a continuing program of aircraft flutter research initiated and sponsored by the Aircraft Laboratory, Wright Air Development Center. The project was administered by Messrs. W. J. Mykytow and L. A. Tolve of the Dynamics Branch, Aircraft Laboratory and conducted under ARDC Project, Task No. 1370-13472, "Subsonic Wind Tunnel Tests on Straight and Sweptback Wings Carrying Tip Weights".

This report reveals information relating to flutter research with military implications to aircraft design. Since the safeguarding of this information is necessary in the interests of national security, this report, exception the title, has been classified "Confidential" in its entirety in accordance with paragraphs 2.s and 24.a(9) of AFR 205-1.

WADC TR 53-161, Part 2

54WCLSA-416

ABSTRACT

A wind tunnel model was designed, constructed, and tested in order to accumulate experimental data on the effects of systematic changes of various tip pod mass parameters and of rigid body degrees of freedom on wing flutter characteristics, and to compare these data with the results of theoretical analyses. A tapered wing with quarter chord swept back 40° was tested with heavy tip pods in cantilever, symmetric, and antisymmetric configurations.

Flutter analyses were made of two selected configurations in each of the cantilever, symmetric, and antisymmetric modes. Computed results from analyses based on strip theory aerodynamics, with one exception, gave good agreement with experimental results, whereas analyses based on finite wing aerodynamics in general yielded appreciably unconservative flutter speeds.

All phases of the project were conducted at the Cornell Aeronautical Laboratory, Inc., Buffalo, New York. The wind tunnel tests were performed in the Laboratory's $8\frac{1}{2}$ x 12 ft. Variable Density Tunnel during June 1953.

PUBLICATION REVIEW

This report has been reviewed and is approved.

FOR THE COMMANDER:

D. D. McKEE
Colonel, USAF
Chief, Aircraft Laboratory
Directorate of Laboratories

CONFIDENTIAL

TABLE OF CONTENTS

PAGE

CONFIDENTIAL

CONFIDENTIAL

LIST OF ILLUSTRATIONS

CONFIDENTIAL

LIST OF TABLES

SYMBOLS

b	Semichord of wing normal to elastic axis, in inches
b_r	Semichord of wing at reference station (3/4 span) normal to elastic axis = 8.74 inches
ℓ	Length of wing measured along the elastic axis from roll axis to tip pod centerline = 76.63 inches
x	Distance along elastic axis from roll axis, in inches
Λ	Sweep angle of elastic axis = 38° 15'
EI	Wing flexural rigidity, in lb.-in.^{2}
GJ	Wing torsional rigidity, in lb.-in.^{2}
W	Weight of wing per unit span, in lb. per inch
S_α	Static moment of wing about the elastic axis per unit span, positive for aft c.g., in lb.
I_α	Moment of inertia of wing about the elastic axis per unit span, in lb.-in.
$W_{T,F}$	Weight of tip pod and fuselage* respectively, in lb.
$S_{T,F}$	Static moment of tip pod about an axis normal to the tip pod centerline through the intersection of the elastic axis and tip pod centerline, and static moment of fuselage about an axis normal to the fuselage centerline through the intersection of roll axis and elastic axis, respectively, positive for aft c.g., in lb.-in.
$I_{T,F}$	Moment of inertia of tip pod about an axis normal to the tip pod centerline through the intersection of the elastic axis and tip pod centerline, and moment of inertia of fuselage about an axis normal to the fuselage centerline through the intersection of roll axis and elastic axis, respectively, in lb.-in.^{2}
I_φ	Fuselage roll inertia about fuselage centerline, in lb.-in.^{2}
$h^{(i)}$	Normalized mode shape for the ith mode. Superscripts (1), (0), (p), and (r) refer respectively to first cantilever bending, translation, pitch, and roll modes.

---

* Note that as the model described in this report was a half-span model, all fuselage properties as defined here would correspond to the properties of a half-fuselage for a full-scale aircraft.

$\alpha^{(1)}$ — Normalized first cantilever torsion mode shape

$\varphi^{(1)}/H_T^{(1)}$ — Normalized slope of the first cantilever bending mode, in radians per inch, negative for positive $h^{(1)}$

$\varphi_T^{(1)}/H_T^{(1)}$ — Normalized slope of the first cantilever bending mode at the tip, in radians per inch, negative for positive $h^{(1)}$

$H_T^{(i)}$ — Generalized coordinate in the ith mode. Superscripts (1), (α), (0), (p), and (r) refer respectively to first uncoupled cantilever bending, first uncoupled cantilever torsion, translation, pitch, and roll modes. Note that the dimensions of all generalized coordinates are in inches, except $H_T^{(\alpha)}$ which is non-dimensional (radians)

m_{ij} — Non-dimensional mass terms defined in Appendix I

η_m — "Effective c.g. location" $= m_{12}/m_{11}$, positive aft

η_T — Tip pod c.g. location $= S_T \cos\Lambda/W_T\, b_r$, positive aft

$K_T\, \varphi_T^{(1)}/H_T^{(1)}$ — Tip pod rotary inertia coupling term in m_{12}, in lb.-in., where $K_T = I_T \sin\Lambda\cos\Lambda$ = product of inertia of tip pod with respect to the elastic axis and the normal to the elastic axis at the tip

V_N — Component of velocity normal to the elastic axis, in mph

V_{cr} — Flutter velocity in the free stream direction, in mph

ρ — Density of air, in lb. per cubic inch

ω — Flutter frequency, in radians per second

ω_i — Frequency of the ith mode, in radians per second

n — Frequency, in cps

g_i — Structural damping coefficient of the ith mode

Subscripts (h), (α), (h₀), (p), and (r) on frequencies and structural damping coefficients refer respectively to first uncoupled cantilever bending, first uncoupled cantilever torsion, translation, pitch, and roll modes.

All other symbols are defined locally, or as in Ref. 5.

SUMMARY

This project was initiated in order to accumulate experimental data on the effect of various tip pod mass parameters on the flutter characteristics of wings with heavy tip pods, and to compare these data with the results of theoretical analyses for selected configurations. The results of this investigation for straight, tapered wings are dealt with in Part 1 of this report. This, the second and final part, considers a tapered wing with quarter chord swept back 40°.

A flutter model, aeroelastically typical of modern high-speed fighter-type aircraft, was designed, constructed, and tested in the wind tunnel. In order to obtain an understanding of the fundamental interactions of the parameters under study in this program, air speeds were limited to the low Mach Number range to avoid further complications due to compressibility effects. A suspension system provided the desired rigid body modes and fuselage mass properties. A complete summary of test results with fuselage and tip pod mass properties for all configurations is found in Appendix III.

Generally, flutter was violent for the symmetric configurations. Although large amplitude flutter was the rule in the antisymmetric configurations, the onset of flutter was more gradual. For most of the configurations, considerable coupling between elastic and rigid body modes was present during flutter, with the flutter frequency in many cases being below the frequency of the first elastic normal mode.

The lowest values of $V_N/b_r(\omega_\alpha)_{cant}$ for the symmetric and cantilever configurations tested were obtained with those cases which had effective c.g. locations, η_E, near zero. The antisymmetric cases showed decreasing stability with increasingly positive effective c.g. locations. It appears that configurations with appreciably negative effective c.g.'s are more stable for both symmetric and antisymmetric root conditions than configurations with correspondingly positive effective c.g.'s.

The tip pod c.g. location, η_T, as reflected in the location of the intersection point of the first two coupled mode nodal lines, is a fundamental parameter in the antisymmetric flutter mode of swept wings with heavy tip pods. Test configurations were stable for intersection points forward of the wing quarter chord, and were increasingly unstable for intersection points aft of the quarter chord.

Computed results from analyses based on strip theory aerodynamics, with one exception, gave good agreement with experimental results, whereas analyses based on finite wing aerodynamics in general yielded appreciably unconservative flutter speeds.

Tunnel testing technique proved satisfactory in all respects. Suspension system, instrumentation, and flutter brake all performed well, allowing flutter data to be obtained with minimum difficulty.

All phases of the work were performed at the Cornell Aeronautical Laboratory, Inc., Buffalo, New York. The wind tunnel tests were performed in the Laboratory's $8\frac{1}{2}$ x 12 ft. Variable Density Tunnel during June 1953.

INTRODUCTION

For the past several years, considerable interest has been shown in the use of large wing tip pods as external fuel or armament stores and for anti-icing equipment. One of the difficulties associated with the design of such airplane configurations has been the lack of pertinent flutter data, which together with the uncertainties in the theoretical analyses of such configurations, indicated the need for an experimental investigation. Accordingly, the present program was initiated.

Previous work on straight wings with concentrated weights located at varying spanwise and chordwise positions is reviewed in Part 1 of this report. Considerable work has been done by Broadbent and others on the effects of rigid body degrees of freedom on the flutter of swept wings. However, for swept wings with concentrated weights, published work has been confined primarily to cantilever root conditions. Ref. 1 considers the effect of variation of spanwise location of a concentrated weight, both at the elastic axis and at the leading edge of a uniform wing. Ref. 2 assesses the effect of variations in the local rigidity of the swept wings near their root on cantilever configurations similar to those of Ref. 1. Ref. 3 investigates a high aspect ratio, non-uniform sweptback wing, with two concentrated weights located at two fixed stations along the span. The flutter analyses of Ref. 3, based on the first uncoupled cantilever bending and torsion modes, resulted in good correlation of theory and experiment. None of the above references considered wings with tip pods, nor were the effects of rigid body degrees of freedom investigated.

This project is part of a program to determine experimentally the effects of large tip pods with varying mass parameters on the flutter speed of straight and sweptback wings. Part 1 of this report is concerned with the investigation of a straight tapered wing with heavy tip pods. This, the second and final part, deals with a tapered wing with the quarter chord sweptback 40°, with particular reference to the symmetric and antisymmetric flutter modes. True symmetric root conditions were obtained, with freedom in both rigid body translation and pitch.

The formal objectives of this program may be noted as:

1. Experimental investigation of the effects of variation of tip pod mass parameters on the flutter speed of a wing-fuselage configuration in cantilever, symmetric, and antisymmetric modes.

2. Comparison of the measured data with theory for selected configurations.

I. DESCRIPTION OF MODEL AND EQUIPMENT

The model tested under Part 2 of this program was a half-span, tapered wing, with the quarter chord line swept back 40°. A large tip pod was mounted at the wing tip. The model was mounted vertically in the Cornell Aeronautical Laboratory 8½ x 12 ft. Variable Density Wind Tunnel, the tunnel ceiling acting as a reflection plane. Figs. 2 and 3 show the model as mounted in the wind tunnel.

The model semi-span measured 60 in. from the model suspension roll axis to the tip pod centerline. The theoretical root chord normal to the elastic axis at the roll axis was 28 in. and the theoretical tip chord normal to the elastic axis at the tip pod centerline was 14 in., which resulted in a taper ratio of 0.5, and an aspect ratio of 5.2 based on the exposed wing area. The airfoil contour was the NACA Series "0010" over the entire span. The model plan form is shown in Fig. 4.

Model construction was identical in all respects to the model described in Part 1 of this report, except for details involving sweep. These included the wing root fitting for attachment of the wing to the suspension system, and the tip fitting for attachment of the tip pod to the wing tip. The balsa blocks, which provided airfoil contour, were bonded to the dural chord sheet normal to the spar, which was located along the 40% chord line. Tip pods differed from those used in Part 1 of this program only in length, this variation being provided by cylindrical extensions at the nose and tail. Wing mass and tip pod inertial properties of the various test configurations are summarized in Tables 1 and 2 to 4, respectively. Tip pod plan forms are summarized in Table 5.

ADJUSTABLE WEIGHT
PITCH PLATE IN AFT POSITION
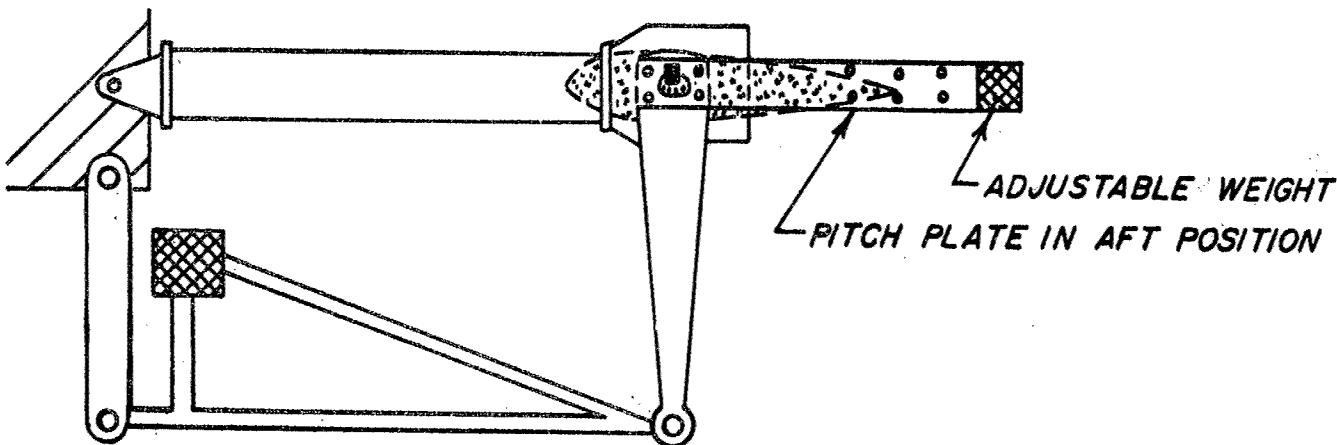
Fig. 1   SUSPENSION SYSTEM SCHEMATIC
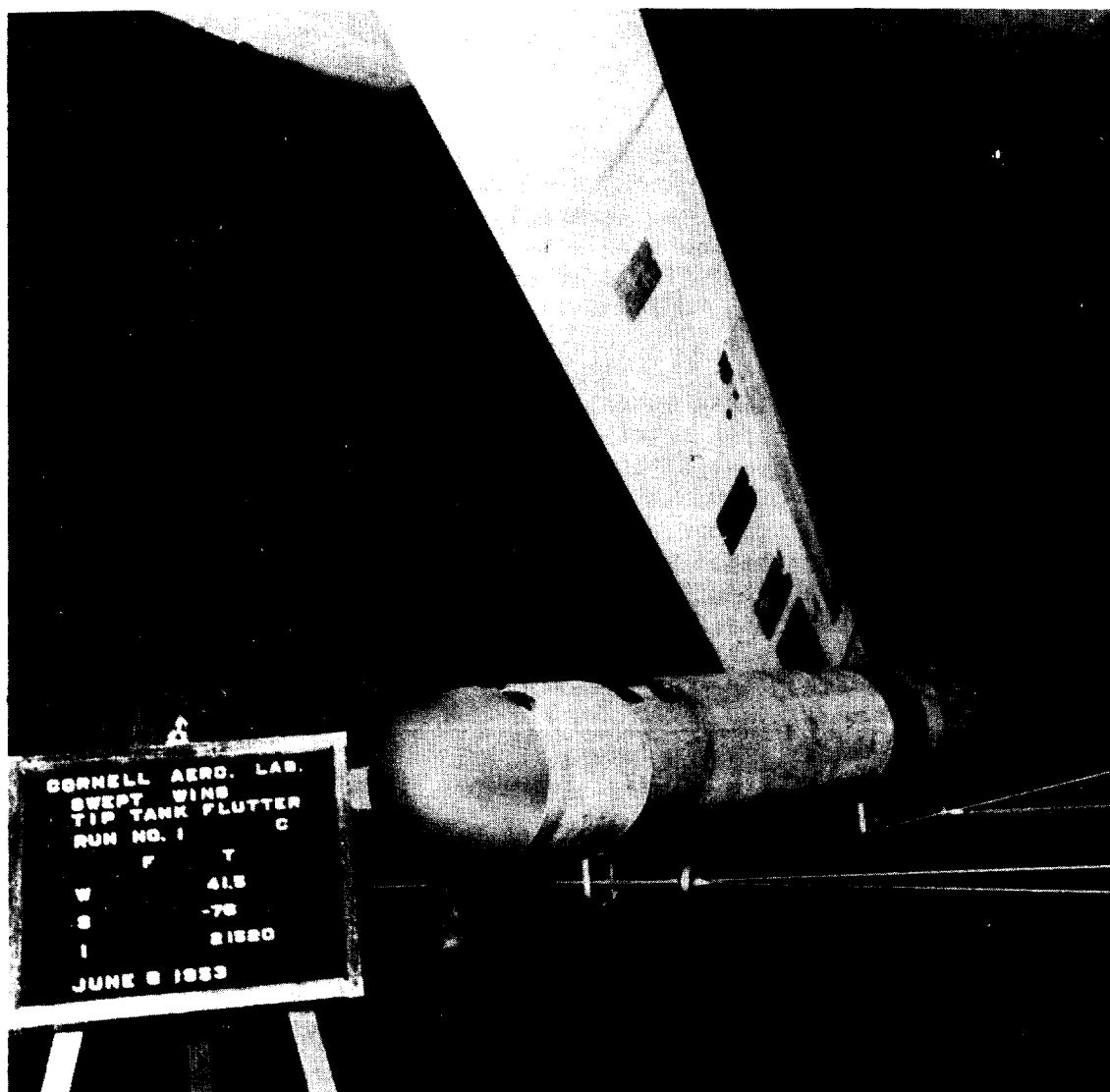
Fig. 2   TUNNEL INSTALLATION OF COMPLETE
MODEL
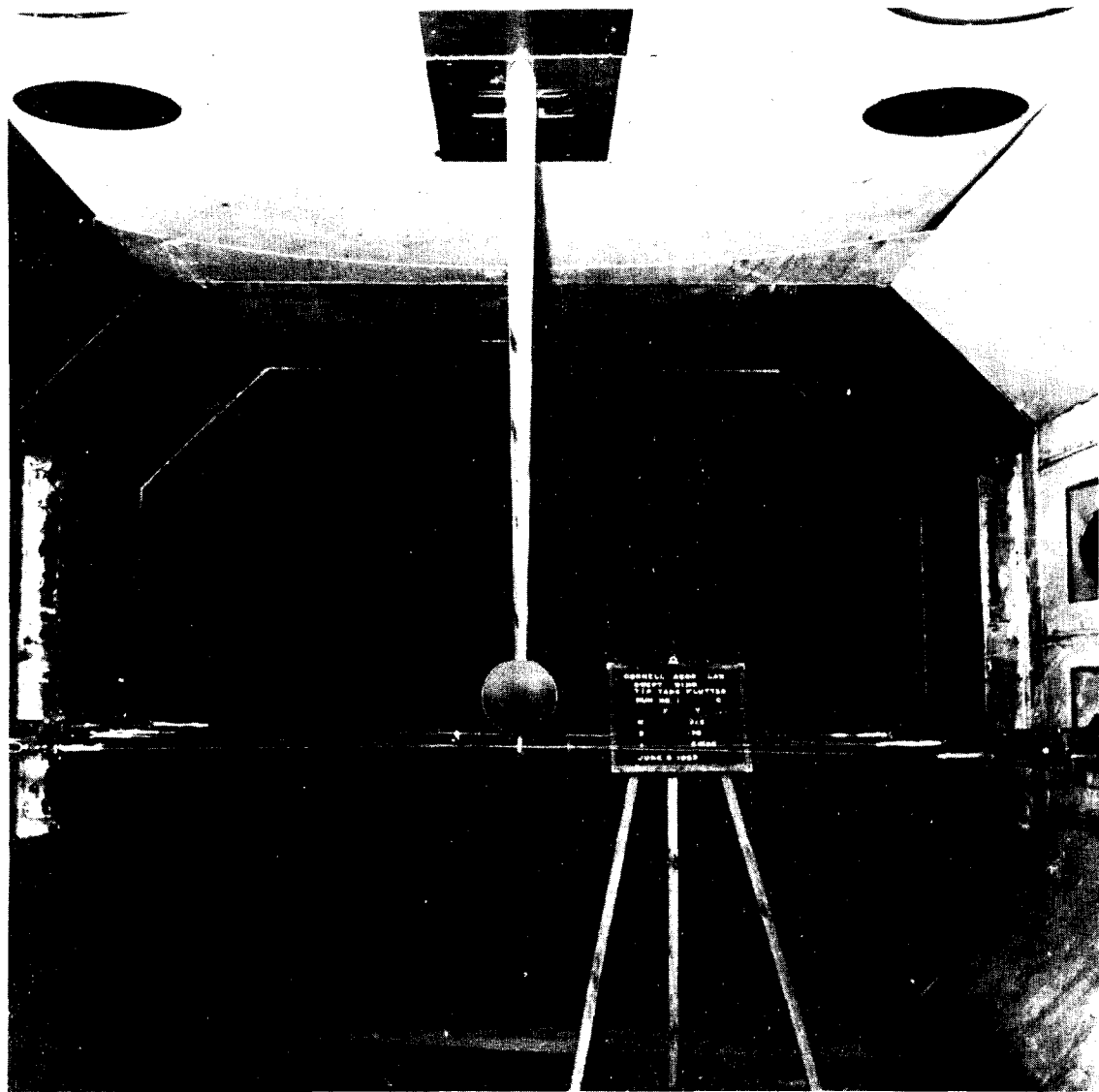
Fig. 3   TUNNEL INSTALLATION OF COMPLETE
MODEL LOOKING DOWNSTREAM
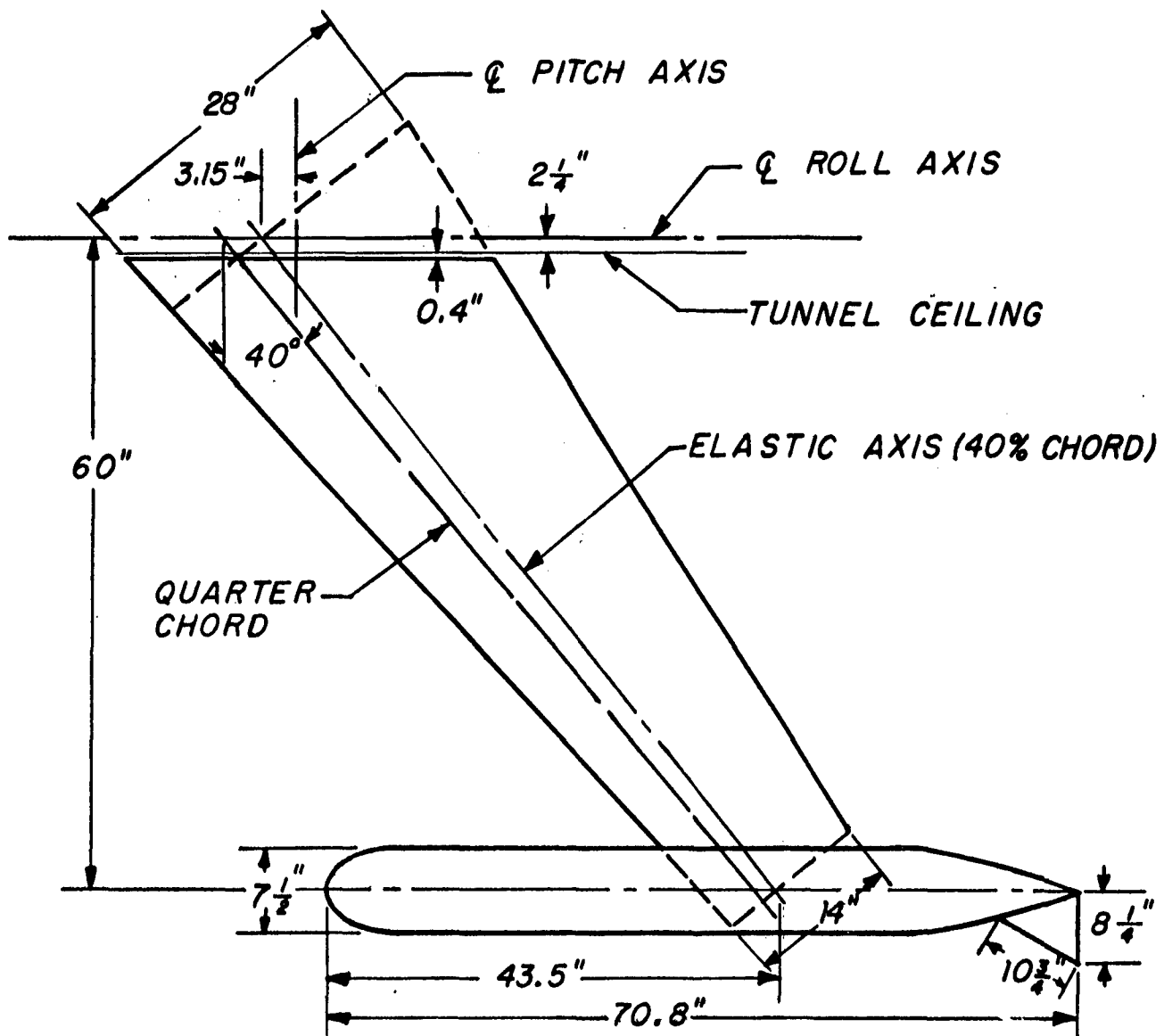
Fig. 4   SWEPT WING PLAN FORM WITH
TYPICAL TIP POD

TABLE I

SUMMARY OF WING MASS PROPERTIES

Station for Concentrated Load	$W\triangle x$	$S_\alpha\triangle x$	$I_\alpha\triangle x$
Inches From Roll Axis Along Elastic Axis	lb.	lb.-in.	lb.-in.^{2}
20.00	9.56	10.13	396.3
35.00	6.41	6.97	215.2
50.00	4.34	3.89	104.7
65.00	3.31	5.19	45.0
76.63	0.49	2.61	16.8

TABLE 2

SUMMARY OF TIP POD AND FUSELAGE MASS PROPERTIES - SYMMETRIC CASES

CASE	W_T lb.	S_T lb.-in.	I_T lb.-in.^{2}	W_F lb.	S_F lb.-in.	I_F lb.-in.^{2}
3	42.7	- 44.5	23040	157.1	+ 22.0	88760
4	51.2	- 423	39520	157.1	+ 22.0	88760
4A	61.0	- 412	46160	157.1	+ 22.0	88760
12	34.9	- 214	17240	157.1	+ 22.0	88760
22	36.3	- 767	31610	157.1	+ 22.0	88760
22A	50.3	-1257	48690	157.1	+ 22.0	88760
33	52.6	+ 416	19820	157.1	+ 22.0	88760
33A	52.6	+ 416	19820	155.7	-1287	88660
33B	Same as 33A - Pitch Locked			155.7	--	--
33C	Same as 33A - Translation Locked			--	--	88660
100	24.2	- 267	10500	157.1	+ 22.0	88760

TABLE 3

SUMMARY OF TIP POD MASS PROPERTIES - CANTILEVER CASES

CASE	W_T lb.	S_T lb.-in.	I_T lb.-in.^{2}
3	42.7	- 44.5	23040
4	51.2	-423	39520
4A	61.0	-412	46160
10	33.2	-320	15050
13	38.9	-135	18770

TABLE 4

SUMMARY OF TIP POD AND FUSELAGE MASS PROPERTIES - ANTISYMMETRIC CASES

CASE	W_T lb.	S_T lb.-in.	I_T lb.-in.^{2}	I_φ lb.-in.^{2}
3	42.7	- 44.5	23040	33130
4	51.2	-423	39520	33130
10	33.2	-320	15050	33130
13	38.9	-135	18770	33130
15	46.5	+166	21890	33130
15A	46.5	+166	21890	57200
15B	46.5	+166	21890	17130
18	41.2	-468	12040	33130
18-1	41.2	-468	12040	17130
18-2	41.2	-468	12040	41470
19	41.2	-282	8350	33130
19A	55.6	+ 52	15010	33130
22	36.3	-767	31610	33130
28	55.6	-133	18700	41470
28-1	55.6	-133	18700	33130
30	51.0	-635	14690	57200
31	21.8	-180	7530	33130

CONFIDENTIAL

TABLE 5

SUMMARY OF TIP POD PLAN FORMS
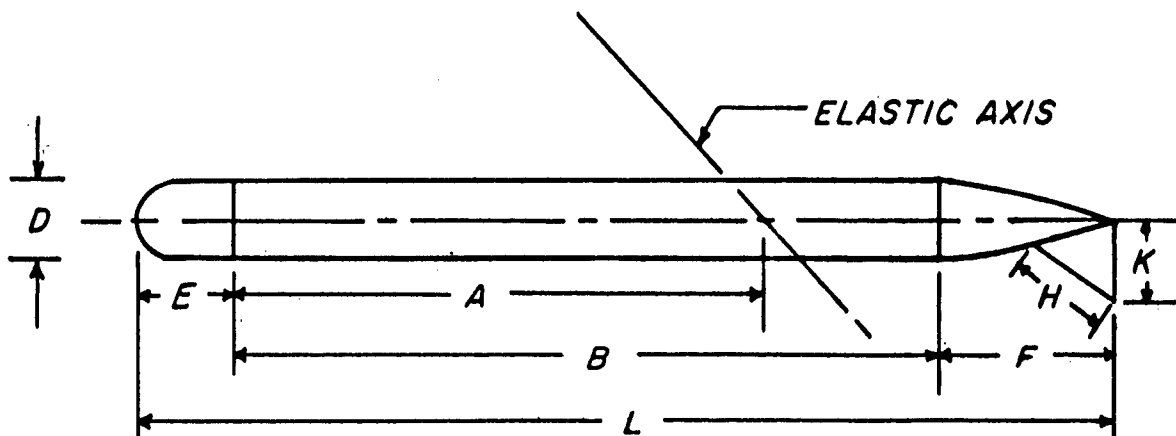
DIMENSION	CASE	
	4, 4A, 22, 22A	ALL OTHERS
A	34.9	34.9
B	46.2	46.2
D	7.5	7.5
E	8.6	5.6
F	16.0	16.0
H	10.75	10.75
K	8.25	8.25
L	70.8	67.8

All dimensions in inches.
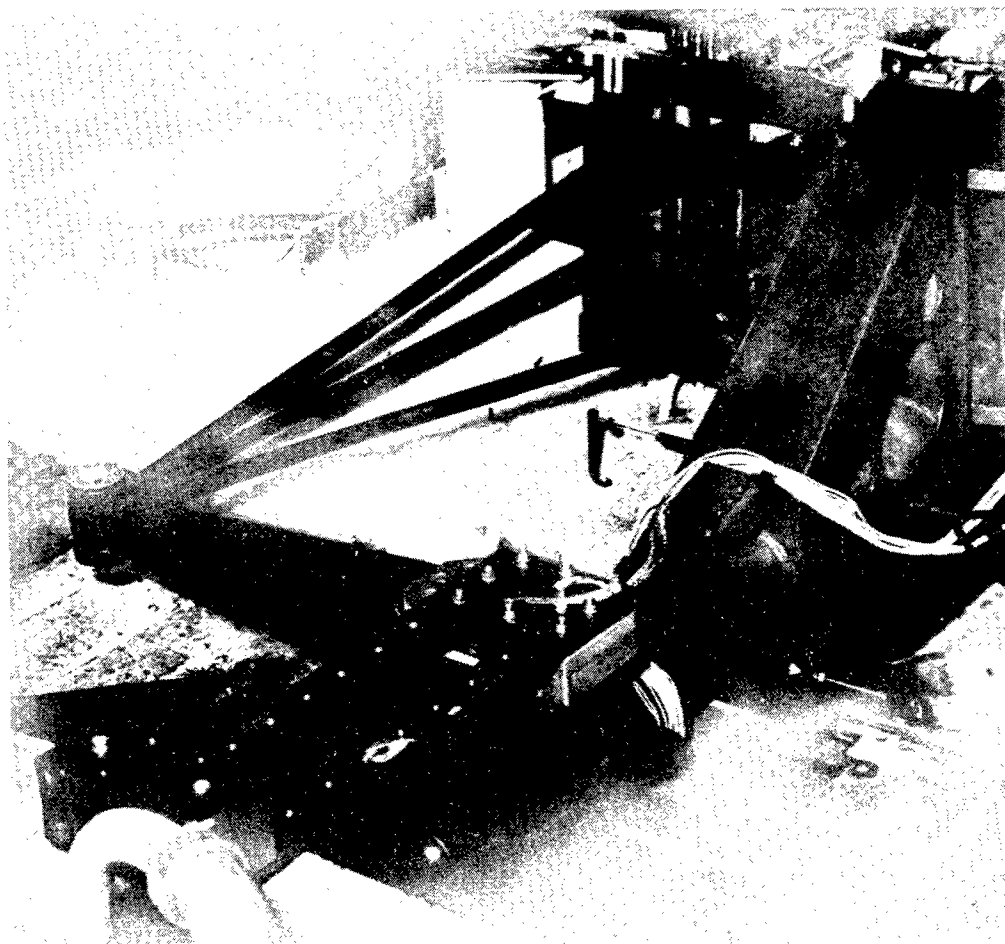
CONFIDENTIAL

CONFIDENTIAL

*Fig. 5 SUSPENSION SYSTEM SHOWING PITCH
PLATE AND WEIGHT IN FURTHEST AFT POSITION*

CONFIDENTIAL

The wind tunnel model suspension differed from that used in Part 1 of this program in the addition of extension plates to the suspension head assembly, as shown in Fig. 5, and schematically in Fig. 1, p. 1. These plates could be extended either fore or aft of the suspension head assembly. By attaching weights to these extension plates at varying distances from the pitch axis, a larger variation in fuselage static unbalance could be achieved than for the straight wing tests. Also, the Houdaille damper previously incorporated in the suspension was removed. The effective fuselage mass properties for the various configurations are summarized in Tables 2 to 4, pp. 6 and 7.

The flutter brake was identical to that used in the flutter tests of Part 1 of this program. Model instrumentation was likewise identical, except for the use of Consolidated instead of Martin type accelerometers.

A complete summary of test results, together with tip pod and fuselage mass properties for all configurations, is found in Appendix III.

II. PRELIMINARY TESTS

Preliminary tests were of three types: static tests of the model to check the theoretical flexural and torsional stiffness distributions, dynamic tests of the model to determine the coupled mode frequencies and coupled mode nodal lines, and accelerometer and displacement pickup calibration tests.

A. Static Tests

Static tests, which were made with the wing model cantilevered at the root, indicated that the theoretical flexural and torsional stiffness distributions were satisfactory as shown by a comparison of experimental and computed normalized deflection curves. However, it was found that, to obtain good correlation of experimental and computed coupled mode frequencies, small adjustments in the magnitudes of the rigidities were required. Inasmuch as no attempt was made to duplicate the stiffness properties of an actual wing, this procedure was deemed satisfactory. The flexural and torsional rigidities, as used in the vibration and flutter analyses, are shown in Figs. 6 and 7, and normalized deflection curves resulting from these rigidities are compared with static test results in Figs. 8 and 9.
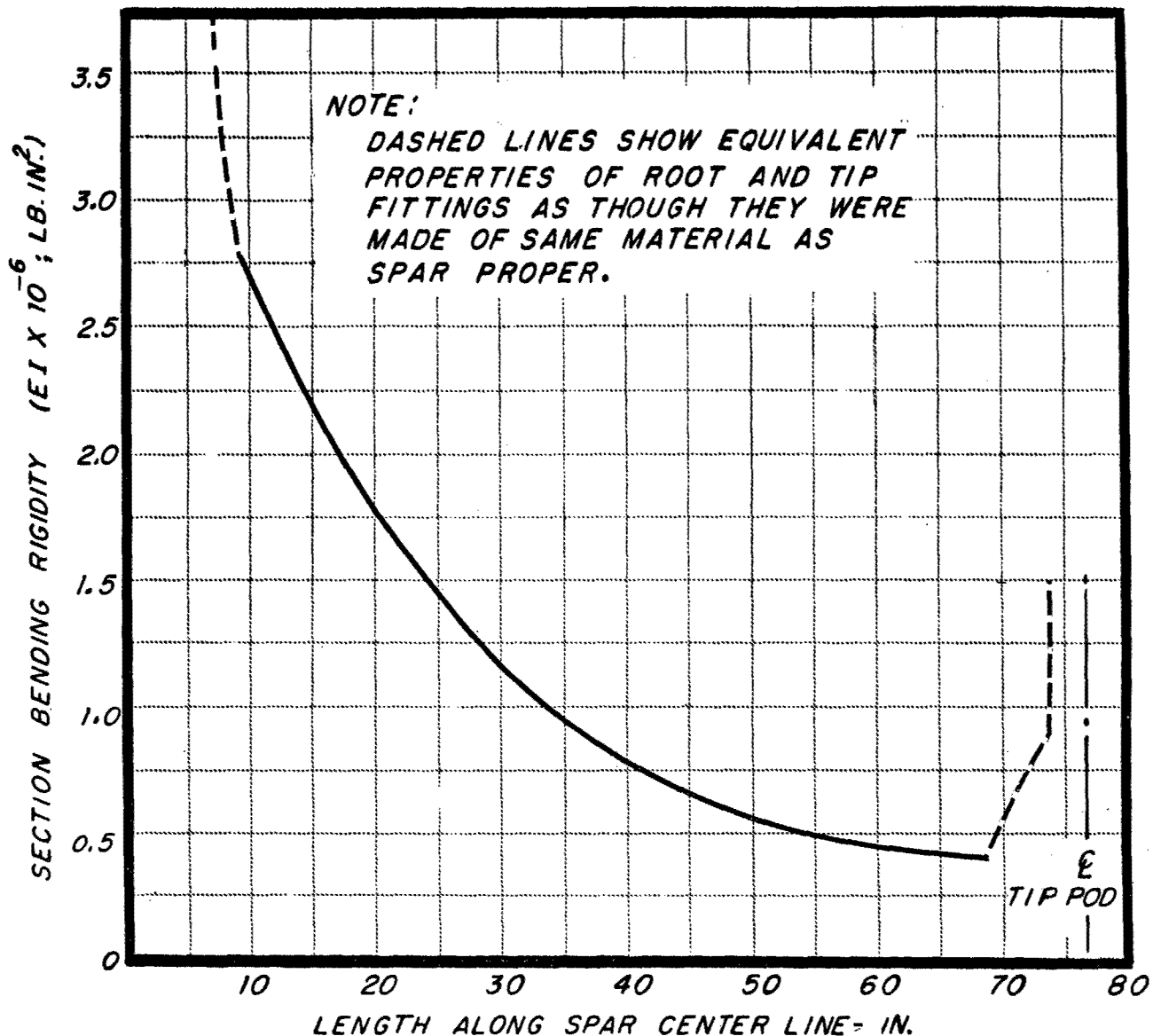
Fig. 6 BENDING STIFFNESS VARIATION WITH SPAN FOR WING MODEL

NOTE:
DASHED LINES SHOW EQUIVALENT
PROPERTIES OF ROOT AND TIP
FITTINGS AS THOUGH THEY WERE
MADE OF SAME MATERIAL AS
SPAR PROPER
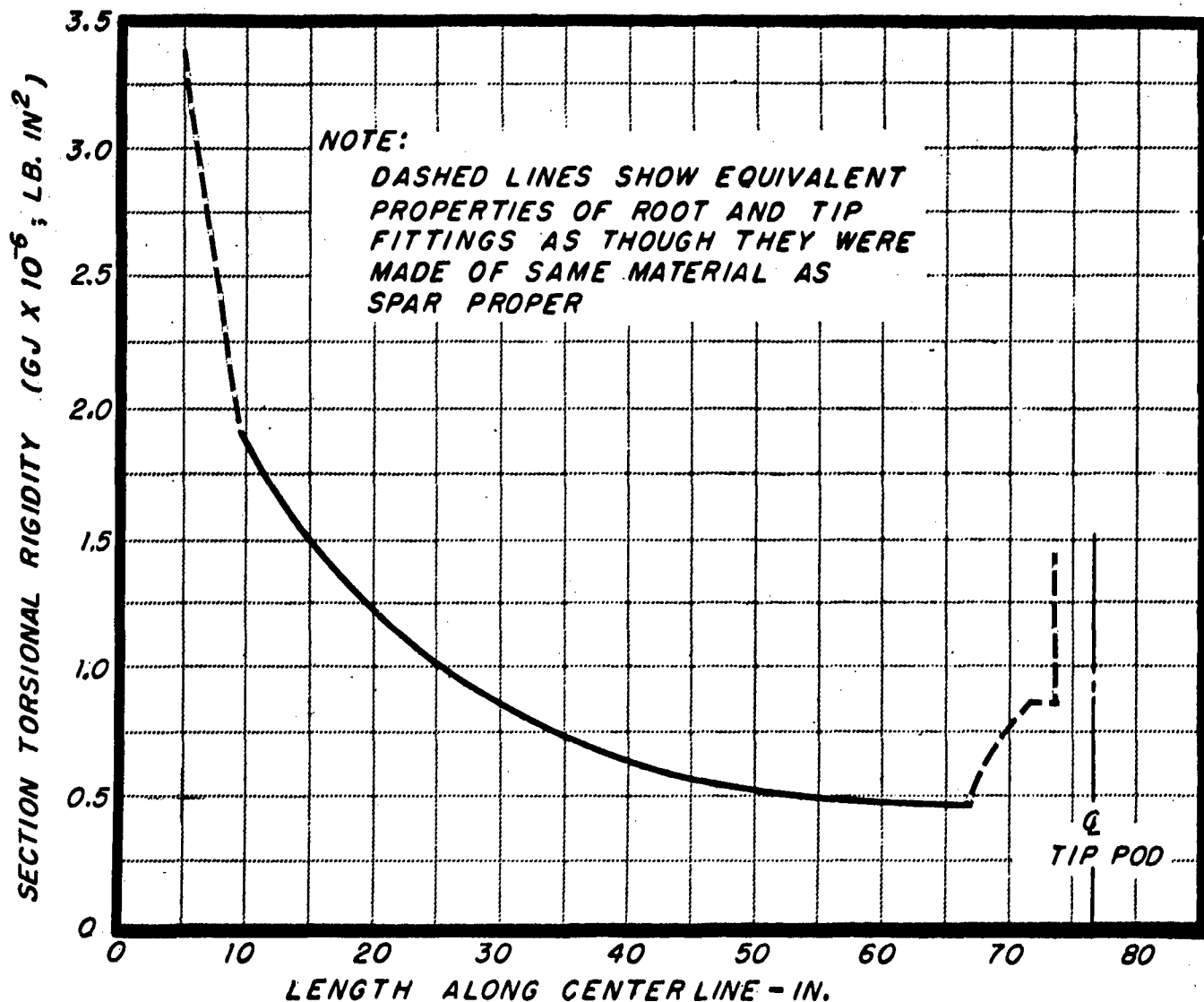
Fig. 7 TORSIONAL STIFFNESS VARIATION WITH SPAN
FOR WING MODEL

Fig. 8 COMPARISON OF COMPUTED AND EXPERI-
MENTAL STATIC BENDING DEFLECTION UNDER UNIT
SHEAR LOAD APPLIED AT INTERSECTION OF TIP POD
CENTER LINE AND ELASTIC AXIS
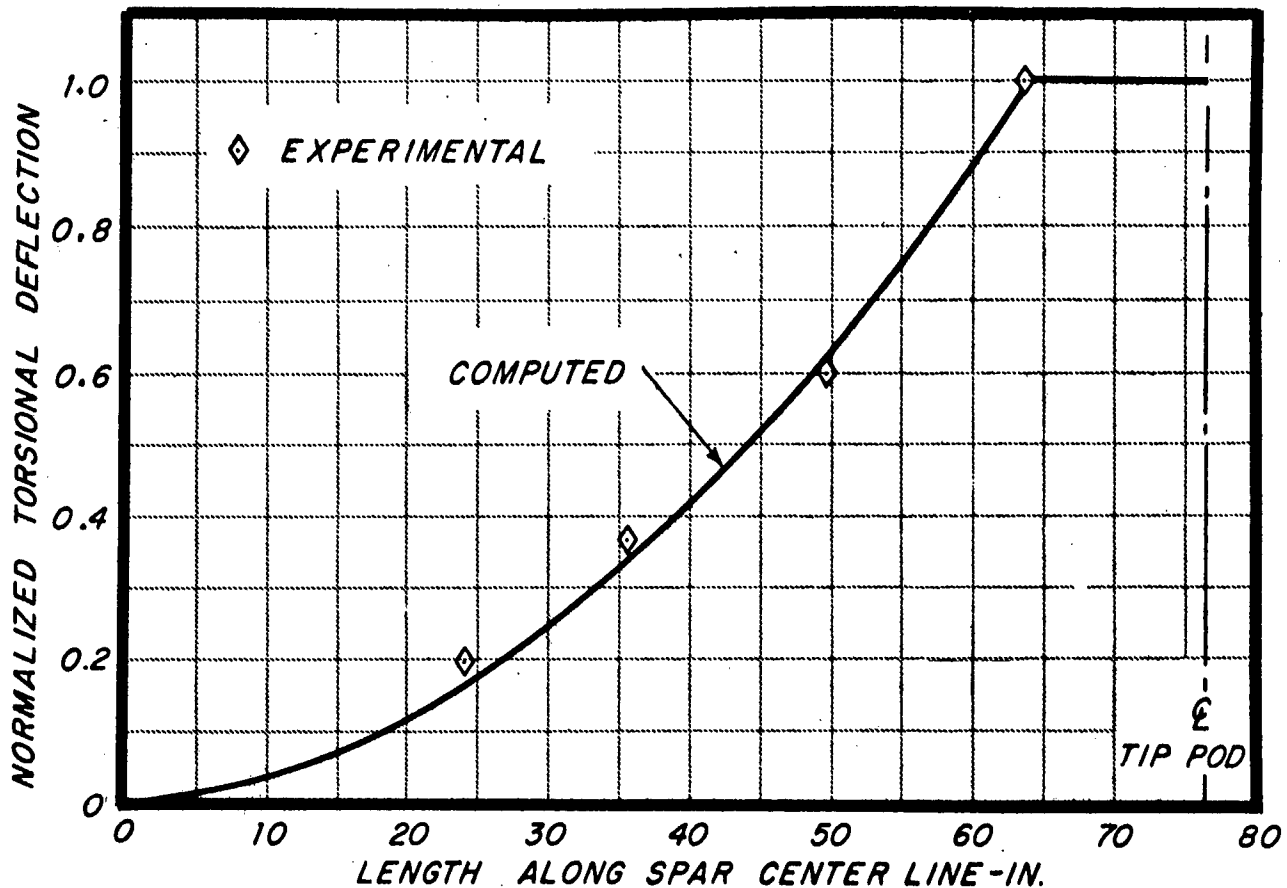
Fig. 9   COMPARISON OF COMPUTED AND
EXPERIMENTAL STATIC TORSIONAL DEFLECTION
UNDER TORQUE APPLIED 13 INCHES INBOARD
FROM TIP ALONG ELASTIC AXIS

B. **Vibration Tests**

Coupled mode frequencies and nodal lines were obtained for all configurations but one (case 15 antisymmetric). The model was excited manually in the proper mode and nodes as observed visually on the wing and on the tip pod were recorded. The model vibration was then allowed to damp out and an oscillograph recording made of the various displacement pickup and accelerometer displacement data. The results of these tests are shown in Figs. 10 to 41.

It should be noted that nodal lines obtained on the tip pod of a swept wing are generally isolated nodal lines, and not necessarily continuous with nodal lines on the wing itself. Whereas a point on a wing coupled mode nodal line is completely defined by the bending and torsional deflection of the elastic axis at that station, tip pod nodal lines are determined by the tip bending slope as well as the tip bending and torsional deflections. In Figs. 10 to 41, nodal lines on the tip pod are shown as isolated points on the tip pod centerline, unless the wing nodal line passes directly through the wing tip.
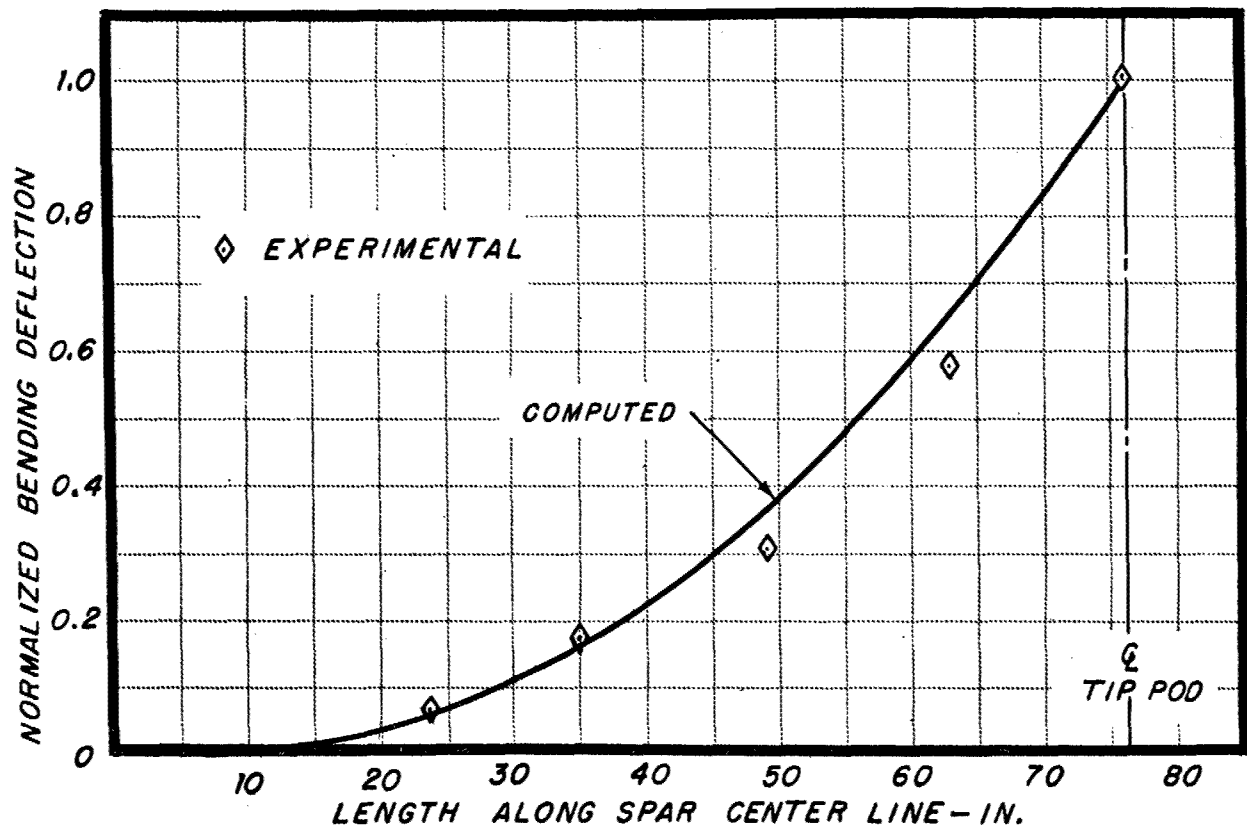
During preliminary vibration tests, an attempt was made to obtain cantilever uncoupled mode frequencies in the manner described in Part 1 of this report. The results were not satisfactory, in that this method did not introduce proper restraint of the tip bending slope, and consequently did not eliminate the rotary inertia coupling of the system.

C. **Calibration Tests**

Fuselage displacement pickups were calibrated in orthodox fashion. A different type of accelerometer calibration was used than in Part 1, in that the accelerometers were calibrated together with their associated channels, rather than independently. Both dynamic calibration, using a vibrating beam at various frequencies, and the usual 2g static acceleration difference calibrations were made.

III. TUNNEL TESTS

All flutter tests were run in the Cornell Aeronautical Laboratory $8\frac{1}{2}$ x 12 ft. Variable Density Wind Tunnel under ambient atmospheric conditions which approximate standard sea level density. The maximum air speed to which any of the tests was carried was approximately 275 mph.

CLASSIFIED

W_T LB.	S_T LB.-IN.	I_T LB.-IN.^{2}	V_{cr} mph	n_{cr} cps	$V_N/b_r\omega$
42.7	-44.5	23,040	124	2.3	14

C/4   E.A.

$n_1(EXP) = 1.4$ cps

$n_1(CALC) = 1.38$ cps

$n_2(EXP) = 2.9$ cps

$n_2(CALC) = 2.89$ cps

c.g.
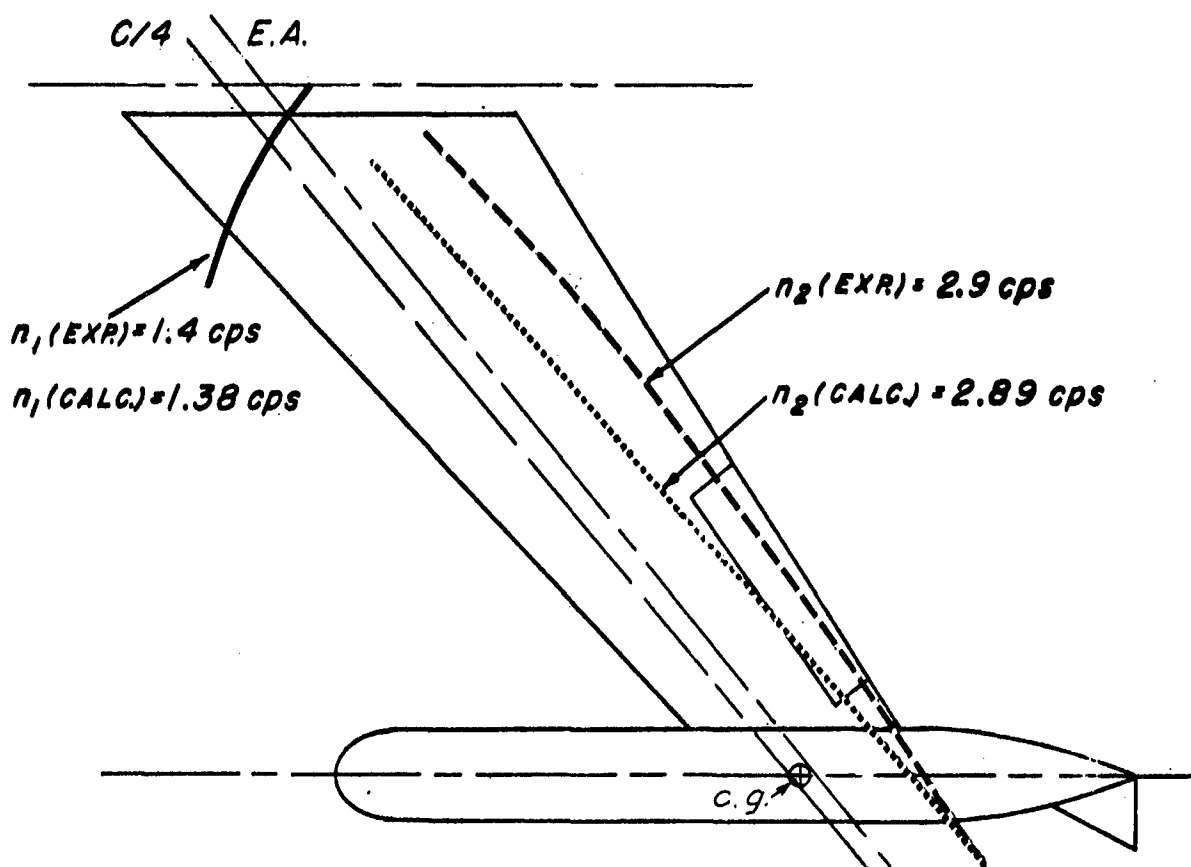
Fig. 10   COUPLED MODE NODAL LINES
CASE 3 CANTILEVER

W_T LB.	S_T LB.-IN.	I_T LB.-IN.^{2}	V_{cr} mph	n_{cr} cps	$V_N/b_r\omega$
51.2	-423	39,520	89	1.9	12
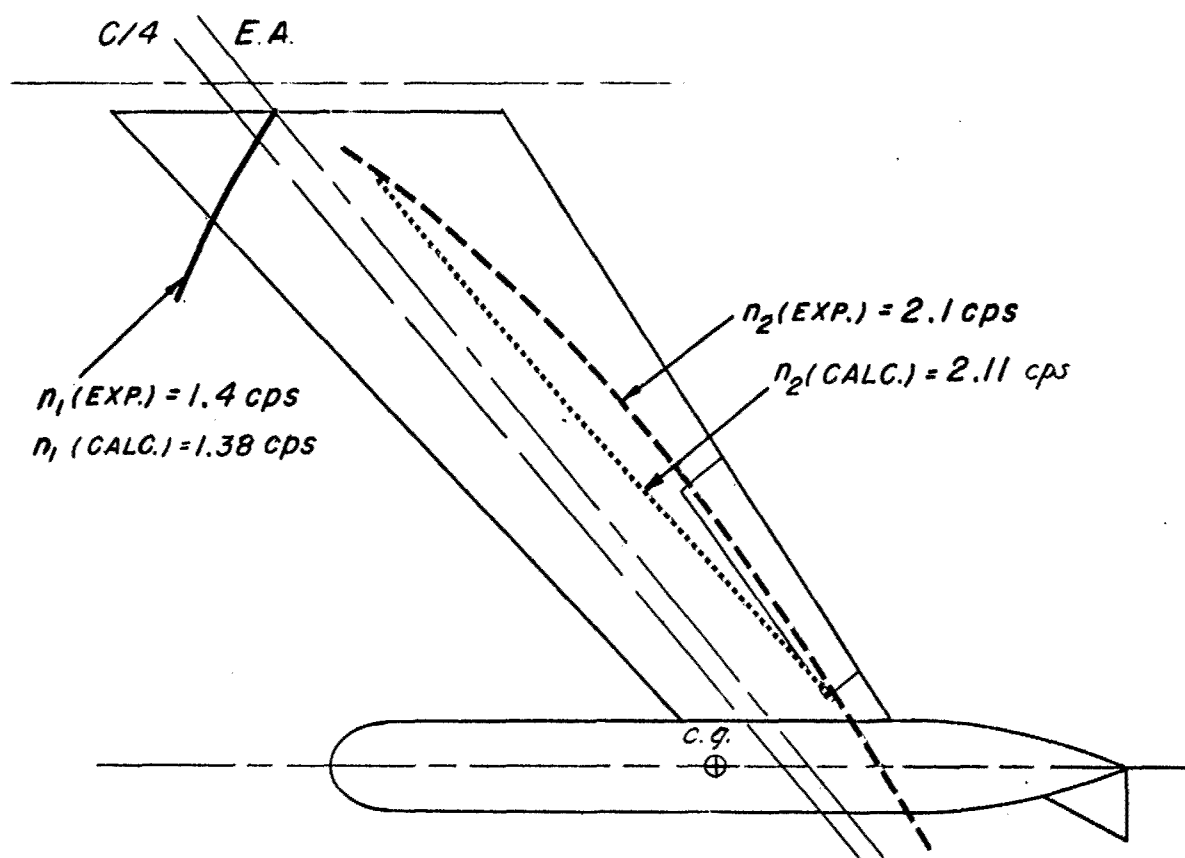
Fig. 11 COUPLED MODE NODAL LINES
CASE 4 CANTILEVER

W_T LB.	S_T LB.-IN.	I_T LB.-IN.^{2}	V_{cr} mph	n_{cr} cps	$V_N/b_r\omega$
61.0	−412	46,160	90.	1.7	13

C/4   E.A.

n_1 (EXP.) = 1.3 cps

n_2 (EXP.) = 1.9 cps

c.g.

Fig. 12 COUPLED MODE NODAL LINES
CASE 4A CANTILEVER

UNCLASSIFIED

W_T LB.	S_T LB.-IN.	I_T LB.-IN.^{2}	V_{cr} mph	n_{cr} cps	$V_N/b_r\omega$
33.2	-320	15,050	130	3.0	11

C/4   E.A.

n_2 (EXP.) = 3.3 cps

n_1 (EXP.) = 1.8 cps

c.g.
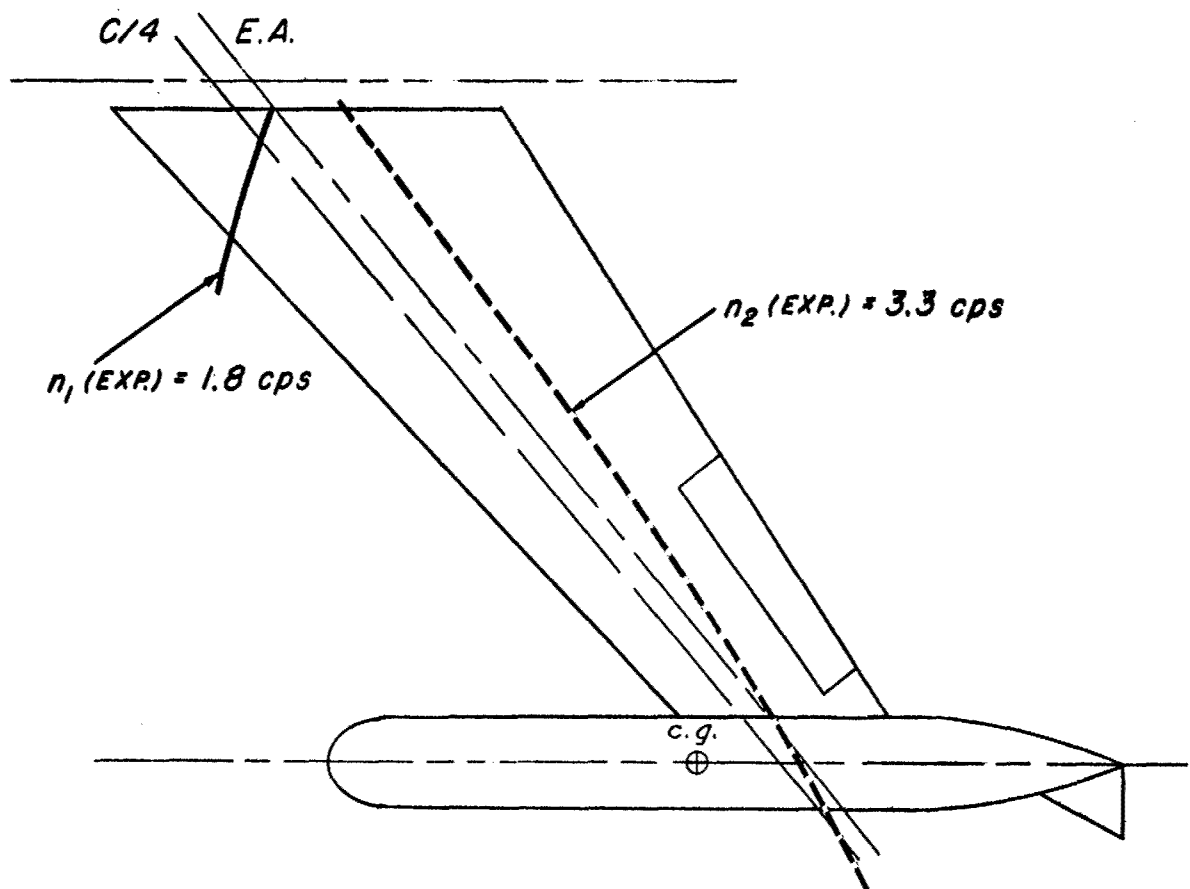
Fig. 13 COUPLED MODE NODAL LINES
CASE 10 CANTILEVER

W_T LB.	S_T LB.-IN.	I_T LB.-IN.^{2}	V_{cr} mph	n_{cr} cps	$V_N/b_r\omega$
38.9	-135	18,770	124	2.5	12
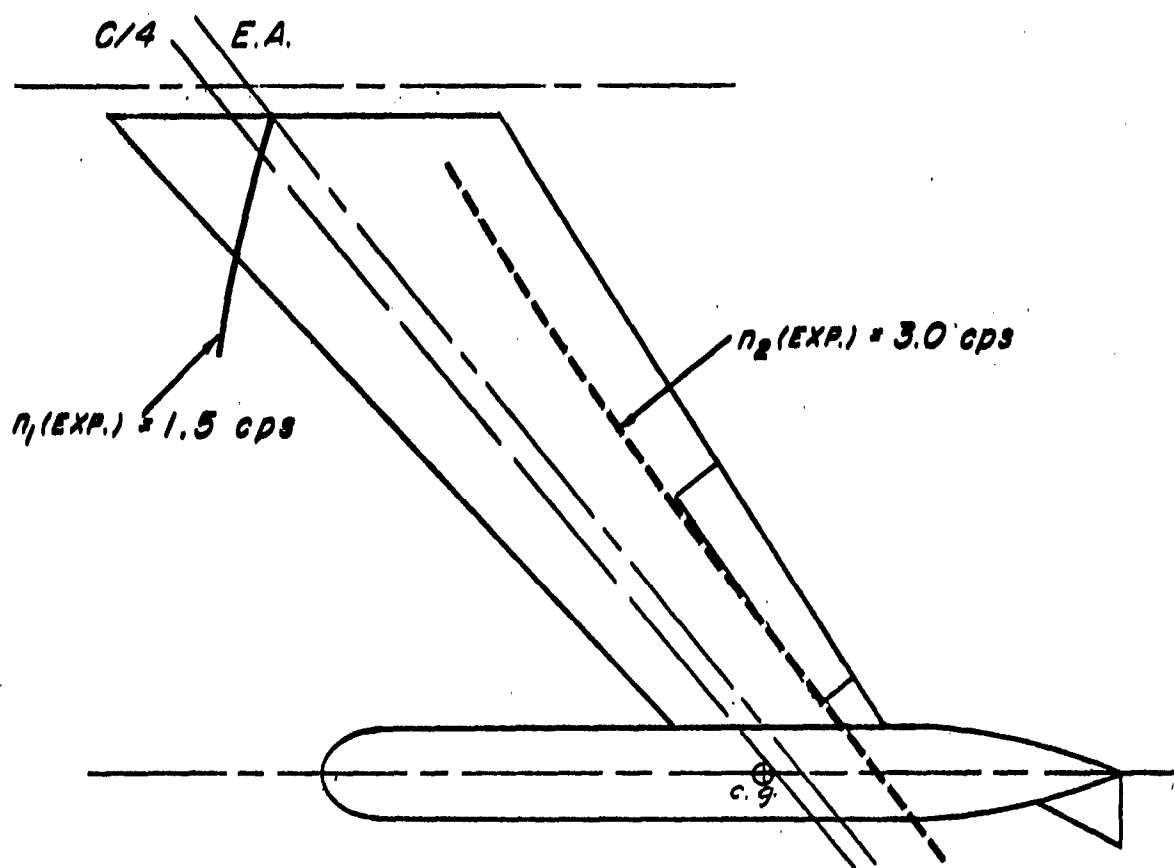
Fig. 14   COUPLED MODE NODAL LINES
CASE 13 CANTILEVER

W_T LB	S_T LB.-IN.	I_T LB.-IN.²	W_F LB.	S_F LB.-IN.	I_F LB.-IN.²	V_{cr} mph	n_{cr} cps	$V_N/b_r\omega$
42.7	-44.5	23,040	157.1	+22.0	88,760	150	2.4	16
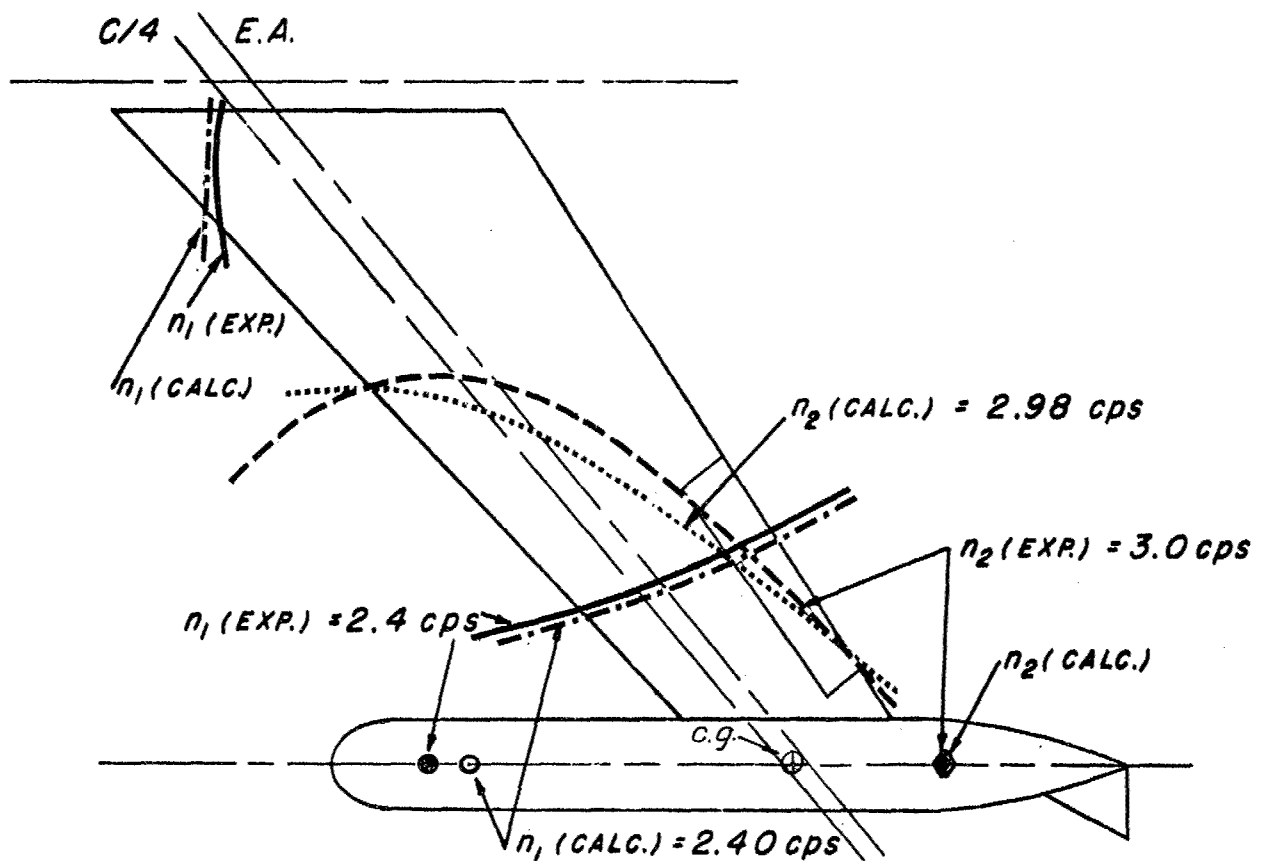
Fig. 15 COUPLED MODE NODAL LINES
CASE 3 SYMMETRIC

W_T LB	S_T LB.-IN.	I_T LB.-IN.^{2}	W_F LB.	S_F LB.-IN.	I_F LB.-IN.^{2}	V_{cr} mph	n_{cr} cps	$V_N/b_r\omega$
51.2	−423	39,520	157.1	+22.0	88,760	138	1.9	18

C/4   E.A.

$n_1(EXP.) = 2.2$ cps

$n_1(CALC.) = 2.21$ cps

$n_2(EXP.) = 2.4$ cps

$n_2(CALC.) = 2.42$ cps

c.g.
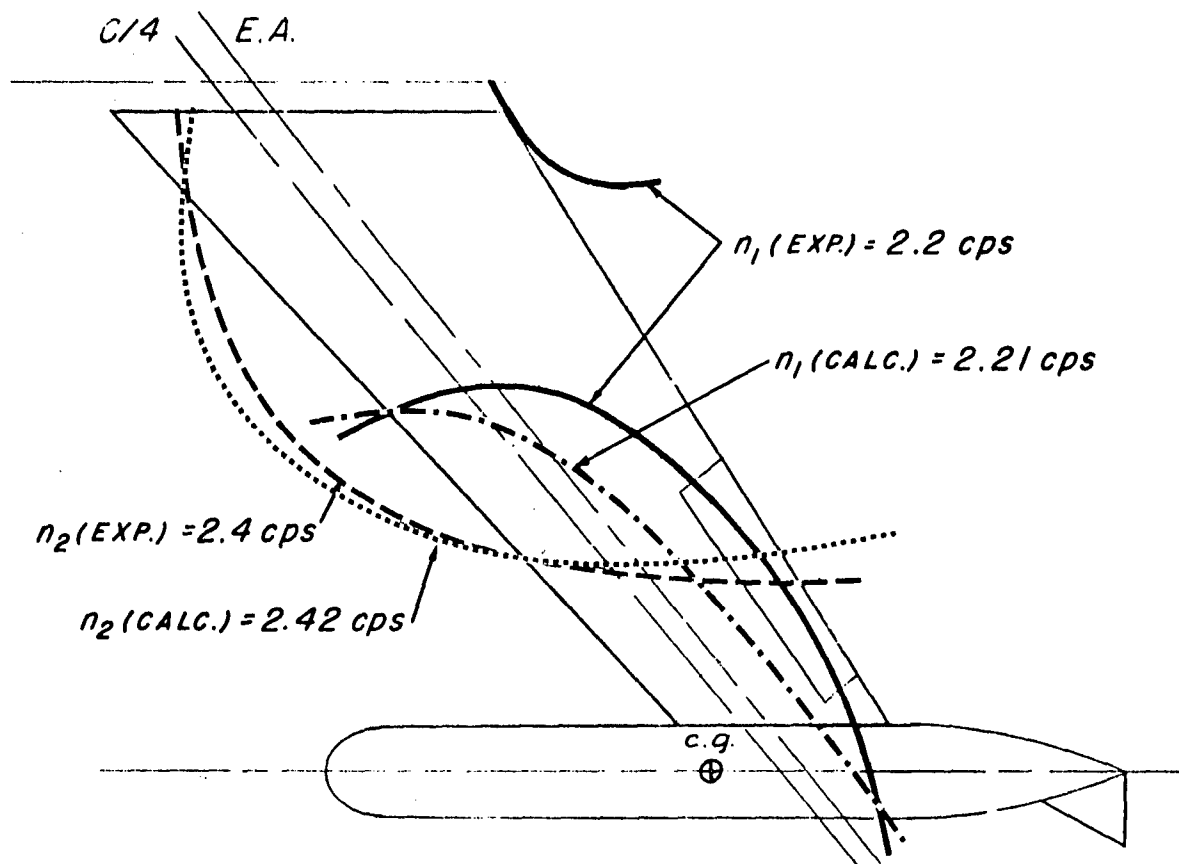
Fig. 16   COUPLED MODE NODAL LINES
CASE   4   SYMMETRIC

W_T LB	S_T LB.-IN.	I_T LB.-IN.^{2}	W_F LB.	S_F LB.-IN.	I_F LB.-IN.^{2}	V_{cr} mph	n_{cr} cps	$V_N/b_r\omega$
61.0	-412	46,160	157.1	+22.0	88,760	139	1.8	19
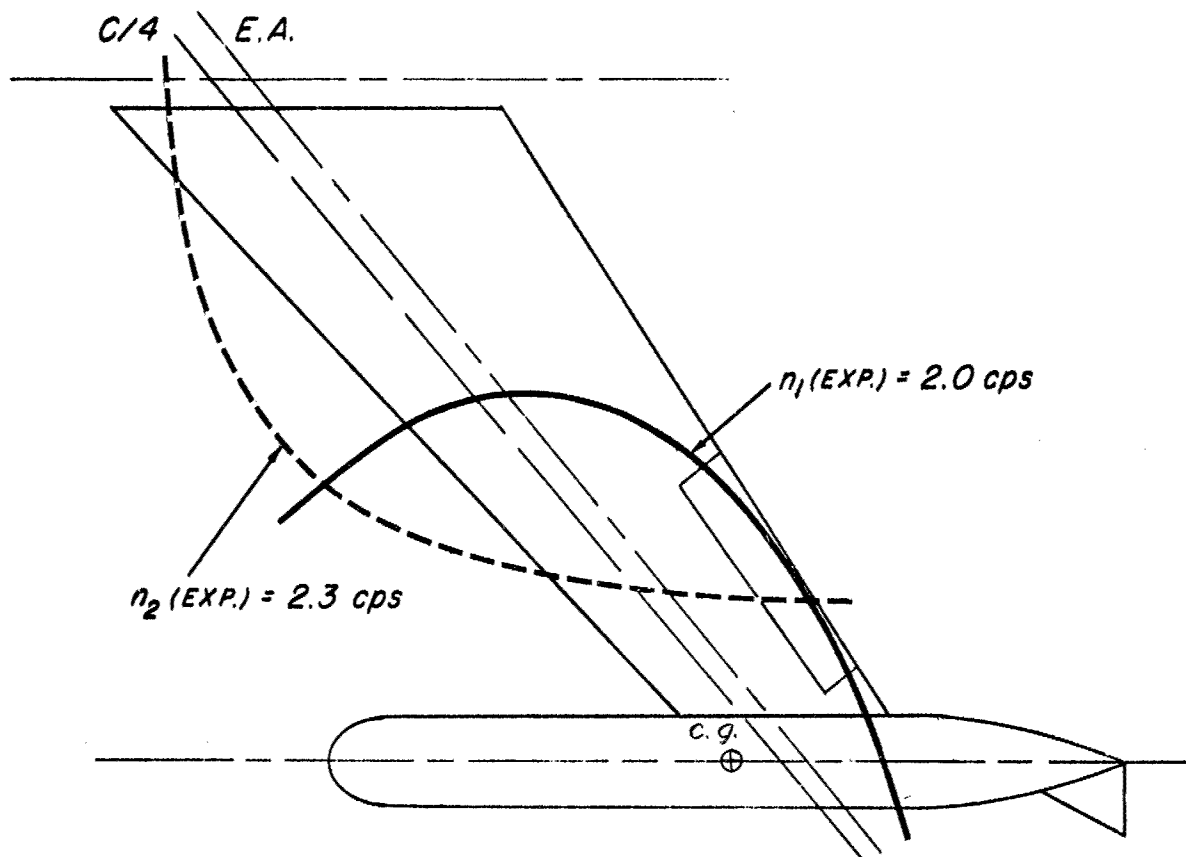
Fig. 17 COUPLED MODE NODAL LINES
CASE 4A SYMMETRIC

UNCLASSIFIED

W_T LB	S_T LB.-IN.	I_T LB.-IN.^{2}	W_F LB.	S_F LB.-IN.	I_F LB.-IN.^{2}	V_{cr} mph	n_{cr} cps	$V_N/b_r\omega$
34.9	−214	17,240	157.1	+22.0	88,760	120	2.8	11
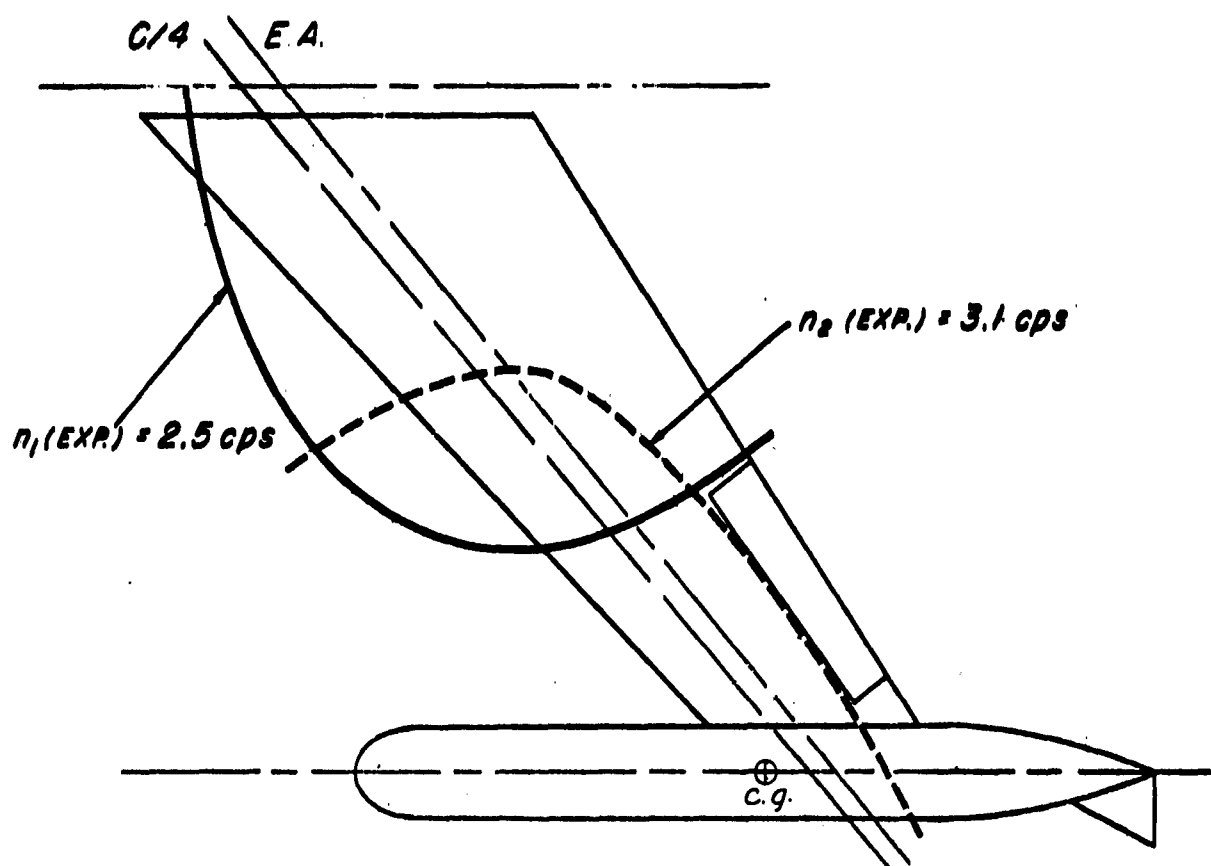
Fig.18   COUPLED MODE NODAL LINES
CASE 12 SYMMETRIC

W_T LB	S_T LB.-IN.	I_T LB.-IN.^{2}	W_F LB.	S_F LB.-IN.	I_F LB.-IN.^{2}	V_{cr} mph	n_{cr} cps	$V_N/b_r\omega$
36.3	−767	31,610	157.1	+22.0	88,760	160	2.2	18
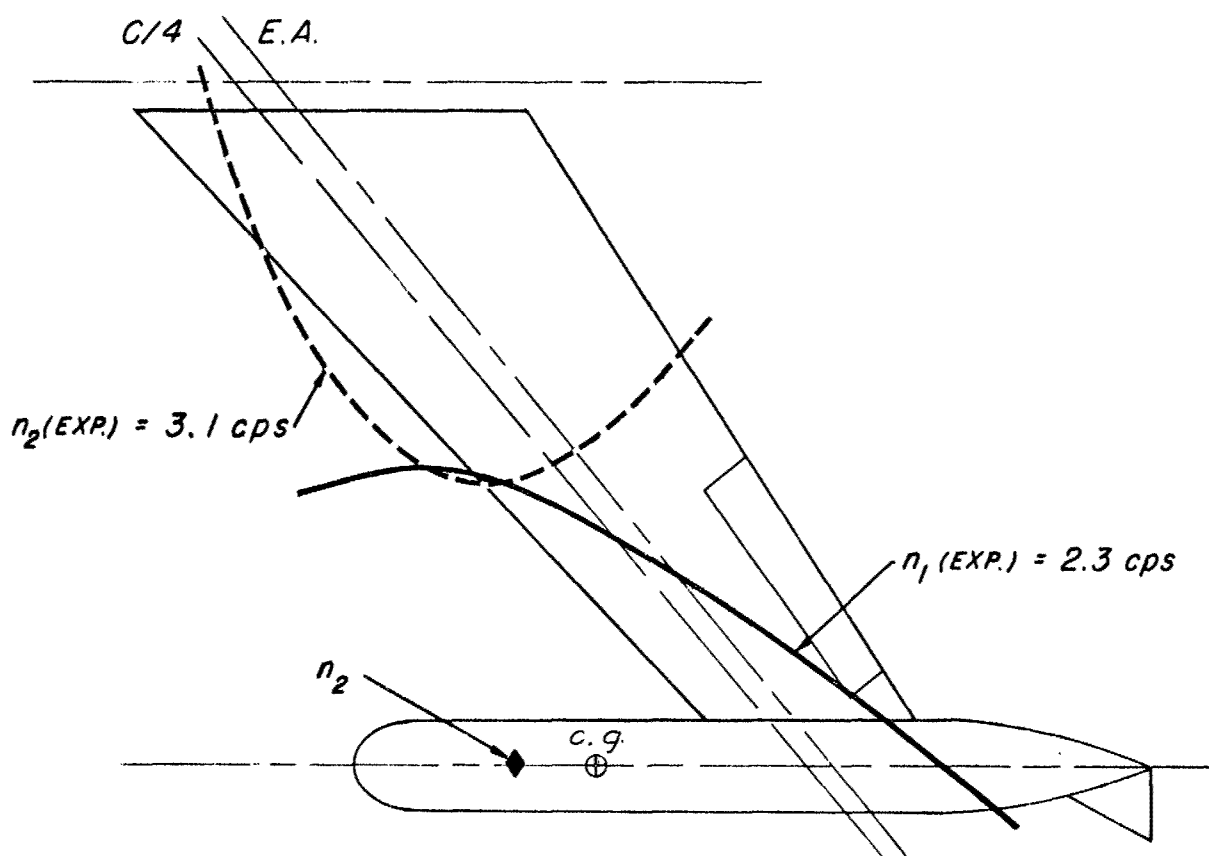
Fig. 19   COUPLED MODE NODAL LINES
CASE 22 SYMMETRIC

W_T LB	S_T LB.-IN.	I_T LB-IN.^{2}	W_F LB.	S_F LB.-IN.	I_F LB.-IN.^{2}	V_{cr} mph	n_{cr} cps	$V_N/b_r\omega$
50.3	-1257	48,690	157.1	+22.0	88,760	NO FLUTTER TO 257 mph		

C/4   E.A.

n_1 (EXP.) = 1.8 cps

n_2 (EXP.) = 3.0 cps

c.g.
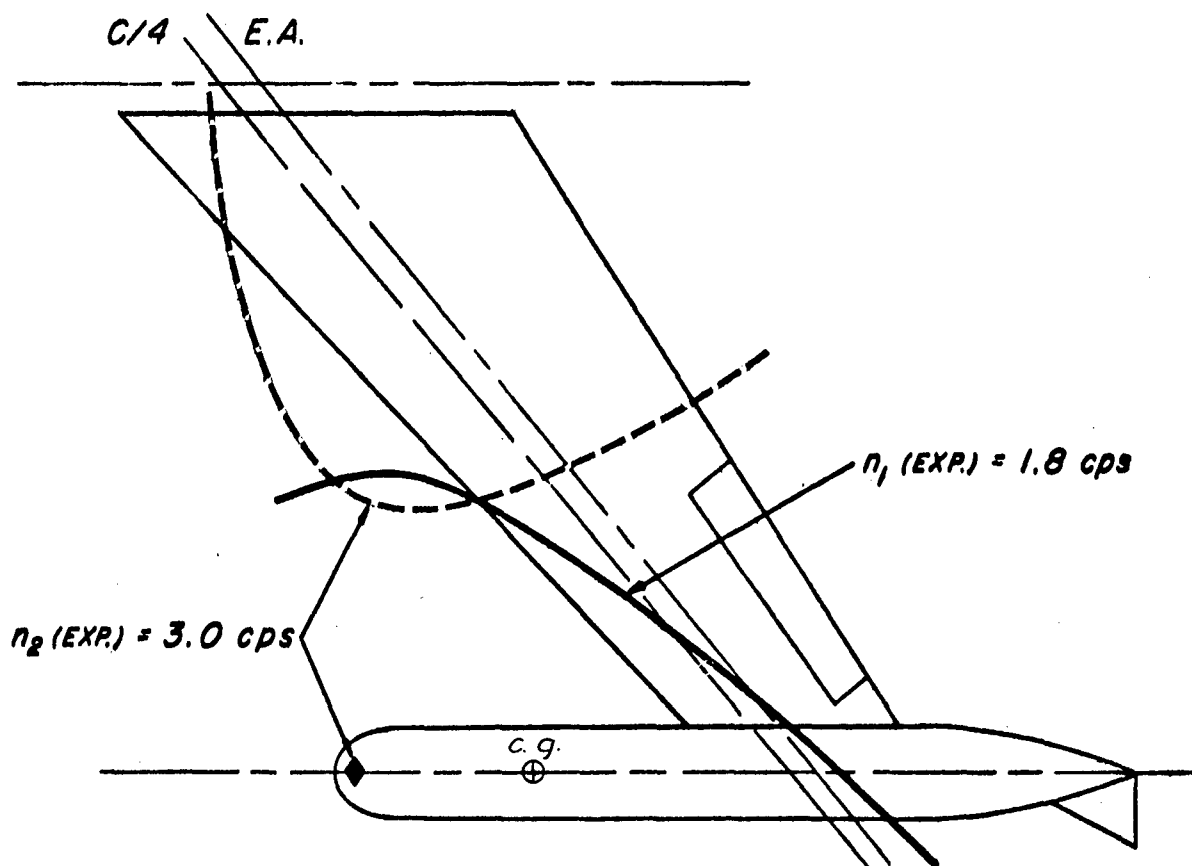
Fig. 20 COUPLED MODE NODAL LINES
CASE 22A SYMMETRIC

W_T LB	S_T LB.-IN.	I_T LB.-IN.^{2}	W_F LB.	S_F LB.-IN.	I_F LB.-IN.^{2}	V_{cr} mph	n_{cr} cps	$V_N/b_r\omega$
52.6	+416	19,820	157.1	+22.0	88,760	NO FLUTTER TO 155 mph		
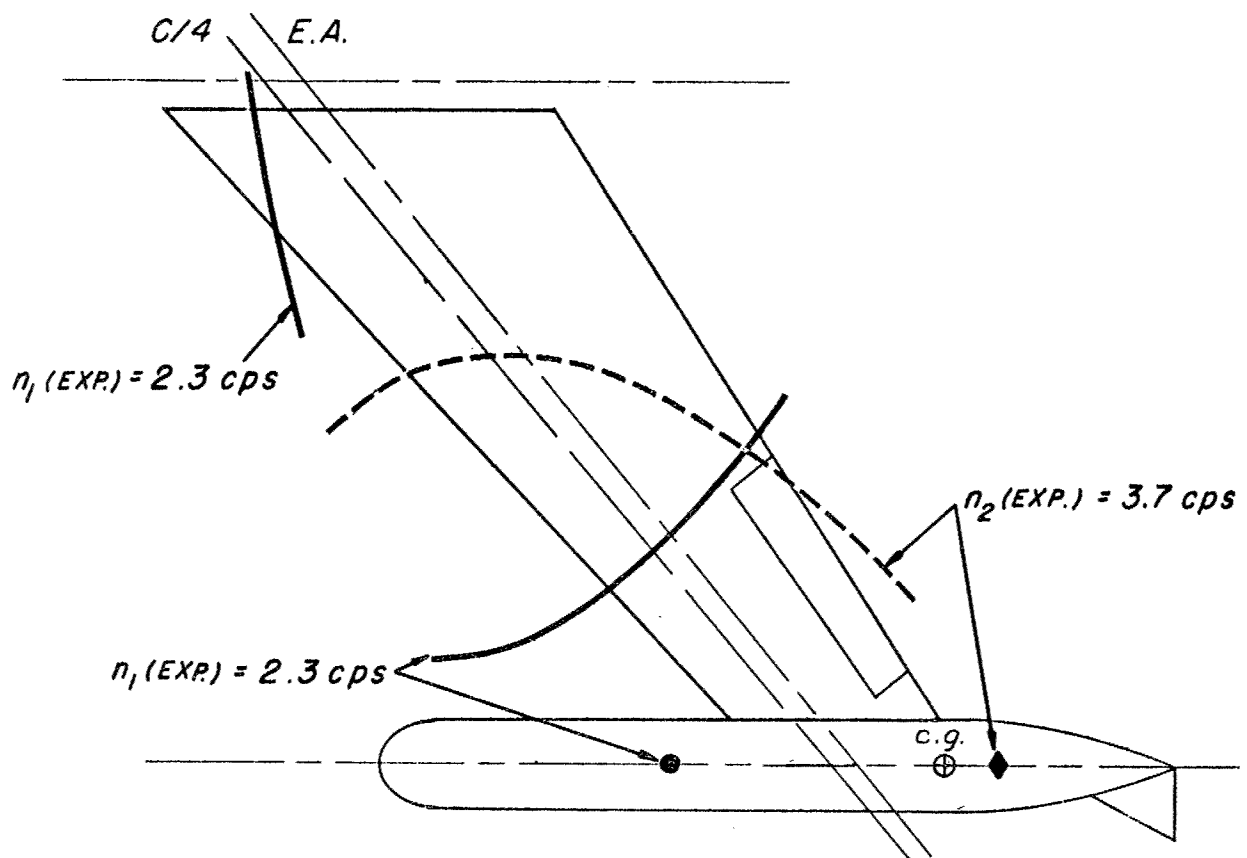
Fig. 21 COUPLED MODE NODAL LINES
CASE 33 SYMMETRIC

W_T LB	S_T LB.-IN.	I_T LB.-IN.^{2}	W_F LB.	S_F LB.-IN.	I_F LB.-IN.^{2}	V_{cr} mph	n_{cr} cps	$V_N/b_r\omega$
24.2	-267	10,500	157.1	+22.0	88,760	230	3.7	16

C/4   E.A.

n_1 (EXP.) = 2.8 cps

n_2 (EXP.) = 4.0 cps

c.g.
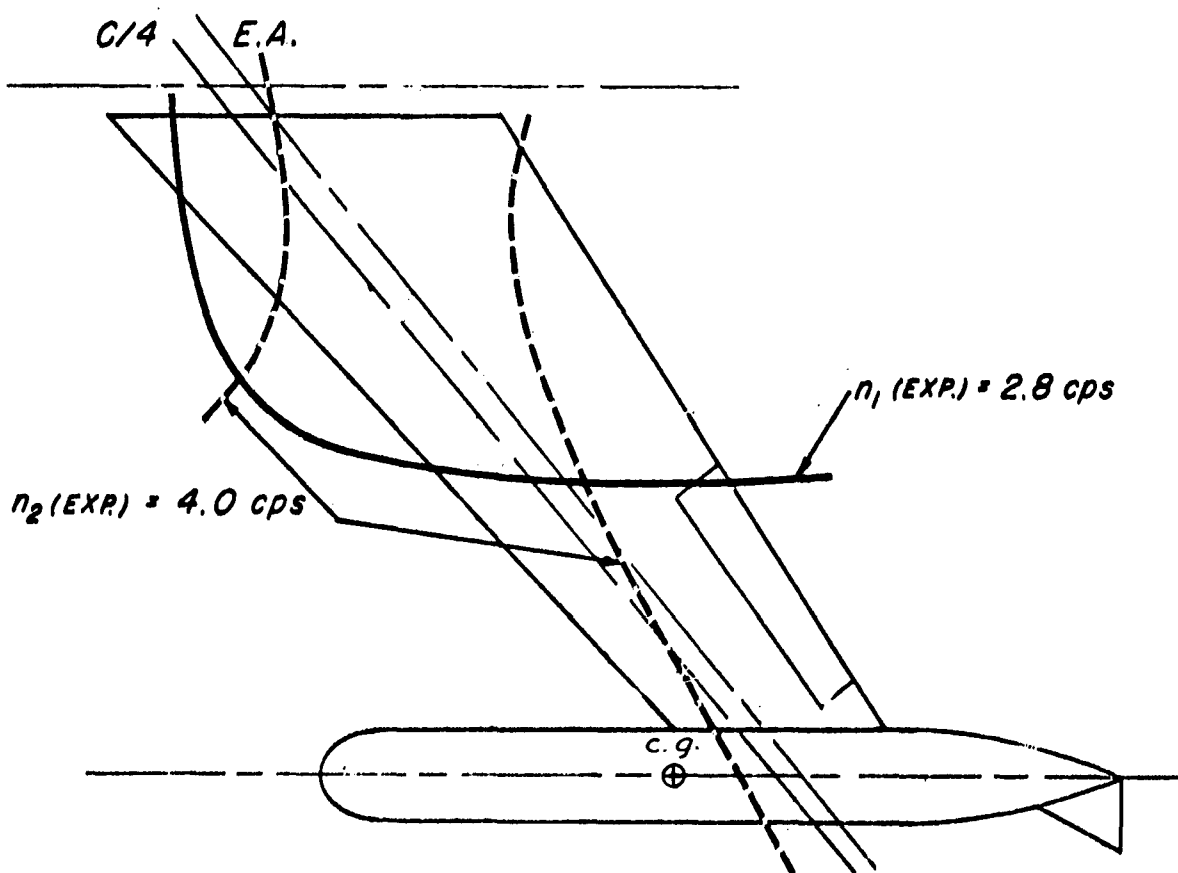
Fig. 22 COUPLED MODE NODAL LINES
CASE 100 SYMMETRIC

UNCLASSIFIED

W_T LB	S_T LB.-IN.	I_T LB.-IN.^{2}	W_F LB.	S_F LB.-IN.	I_F LB.-IN.^{2}	V_{cr} mph	n_{cr} cps	$V_N/b_r\omega$
52.6	+416	19,820	155.7	−1287	88,660	165	3.2	13

C/4   E.A.

n_2 (EXP.) = 3.6 cps

n_1 (EXP.) = 2.5 cps

c. g.
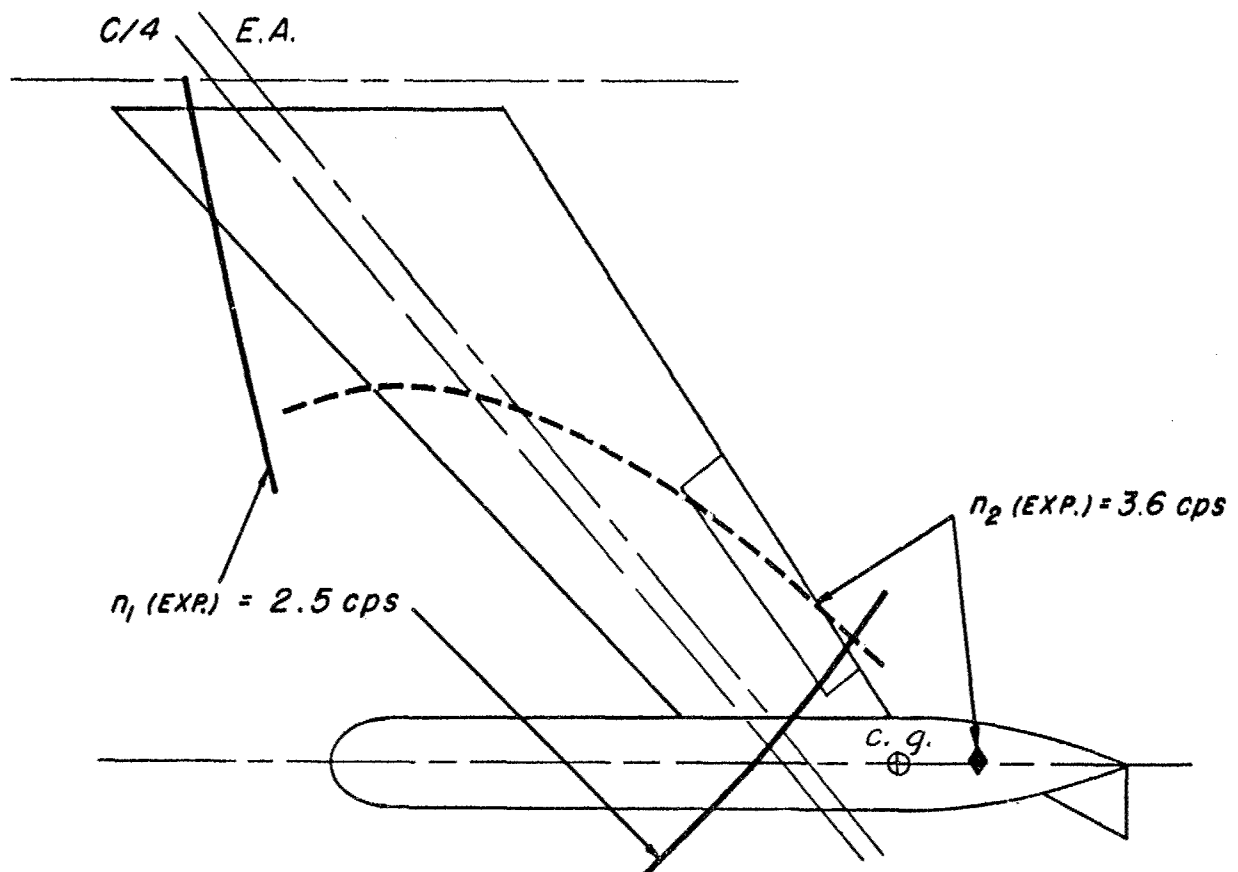
Fig. 23 COUPLED MODE NODAL LINES
CASE 33A SYMMETRIC

W_T LB	S_T LB.-IN.	I_T LB.-IN.^{2}	W_F LB.	S_F LB.-IN.	I_F LB.-IN.^{2}	V_{cr} mph	n_{cr} cps	$V_N/b_r\omega$
52.6	+416	19,820	155.7	-1287	88,660	175	2.6	17

C/4   E.A.

$n_2 (EXP.) = 3.6$ cps

$n_1 (EXP.) = 1.3$ cps

c.g.

Fig. 24 COUPLED MODE NODAL LINES
CASE 33B SYMMETRIC
(TRANSLATION FREE, PITCH LOCKED)

W_T LB	S_T LB.-IN.	I_T LB.-IN.²	W_F LB.	S_F LB.-IN.	I_F LB.-IN.²	V_{cr} mph	n_{cr} cps	$V_N/b_r\omega$
52.6	+416	19,820	155.7	-1287	88,660	151.5	2.0	19

C/4   E.A.

n_2 (EXP.) = 3.5 cps

n_1 (EXP.) = 2.3 cps

c. g.
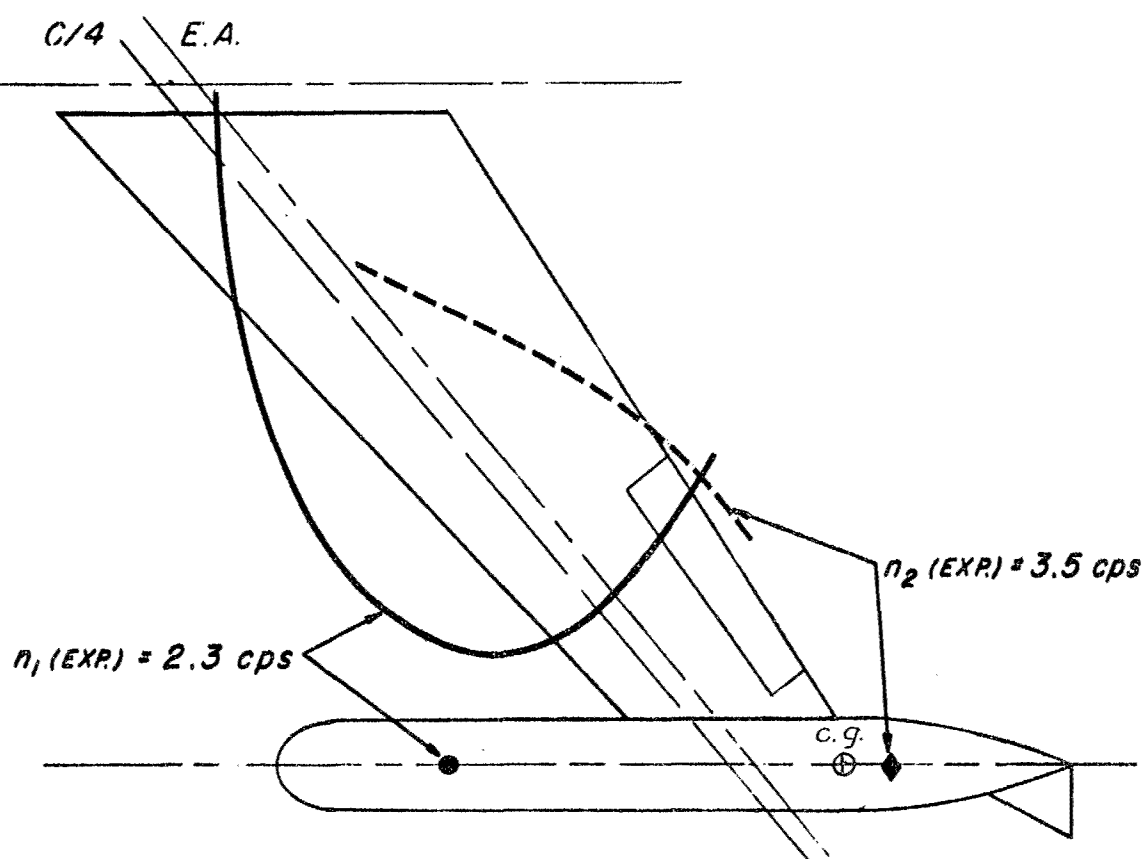
Fig. 25 COUPLED MODE NODAL LINES
CASE 33C SYMMETRIC
(TRANSLATION LOCKED, PITCH FREE)

UNCLASSIFIED

W_T LB.	S_T LB.-IN.	I_T LB.-IN.^{2}	I_ϕ LB.-IN.^{2}	V_{cr} mph	n_{cr} cps	$V_N/b_r\omega$
46.5	+166	21,890	17,130	107	1.7	16
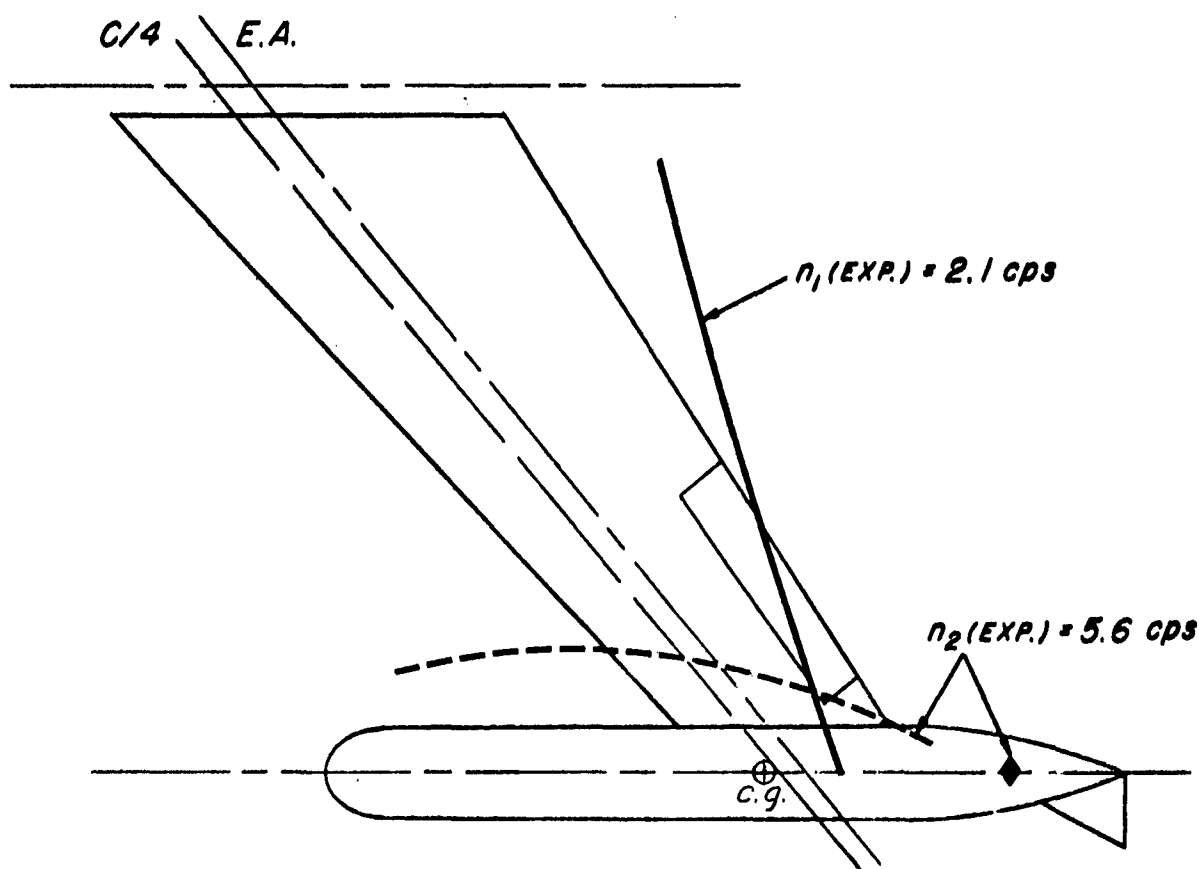
Fig. 26 COUPLED MODE NODAL LINES
CASE 15B ANTISYMMETRIC

W_T LB.	S_T LB.-IN.	I_T LB.-IN.²	I_ϕ LB.-IN.²	V_{cr} mph	n_{cr} cps	$V_N/b_r\omega$
41.2	-468	12040	17130	NO FLUTTER TO 221 mph		
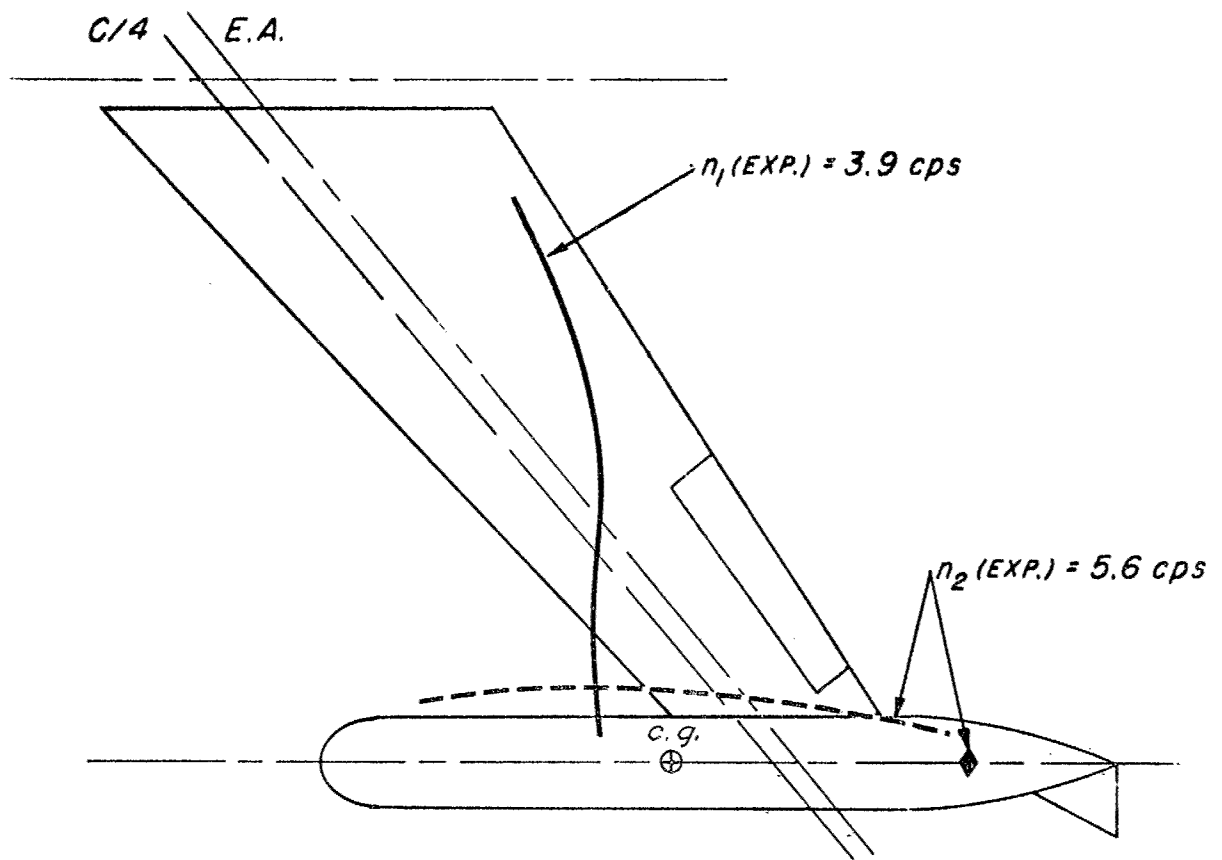
Fig. 27 COUPLED MODE NODAL LINES
CASE 18-1 ANTISYMMETRIC

UNCLASSIFIED

W_T LB.	S_T LB.-IN.	I_T LB.-IN.^{2}	I_ϕ LB.-IN.^{2}	V_{cr} mph	n_{cr} cps	$V_N/b_r\omega$
42.7	-44.5	23,040	33,130	124	1.8	17

C/4   E.A.

n_1 (CALC) = 2.1 cps

n_1 (EXP.) = 2.1 cps

n_2 (EXP.) = 4.5 cps

n_2 (CALC) = 4.3 cps

c.g.
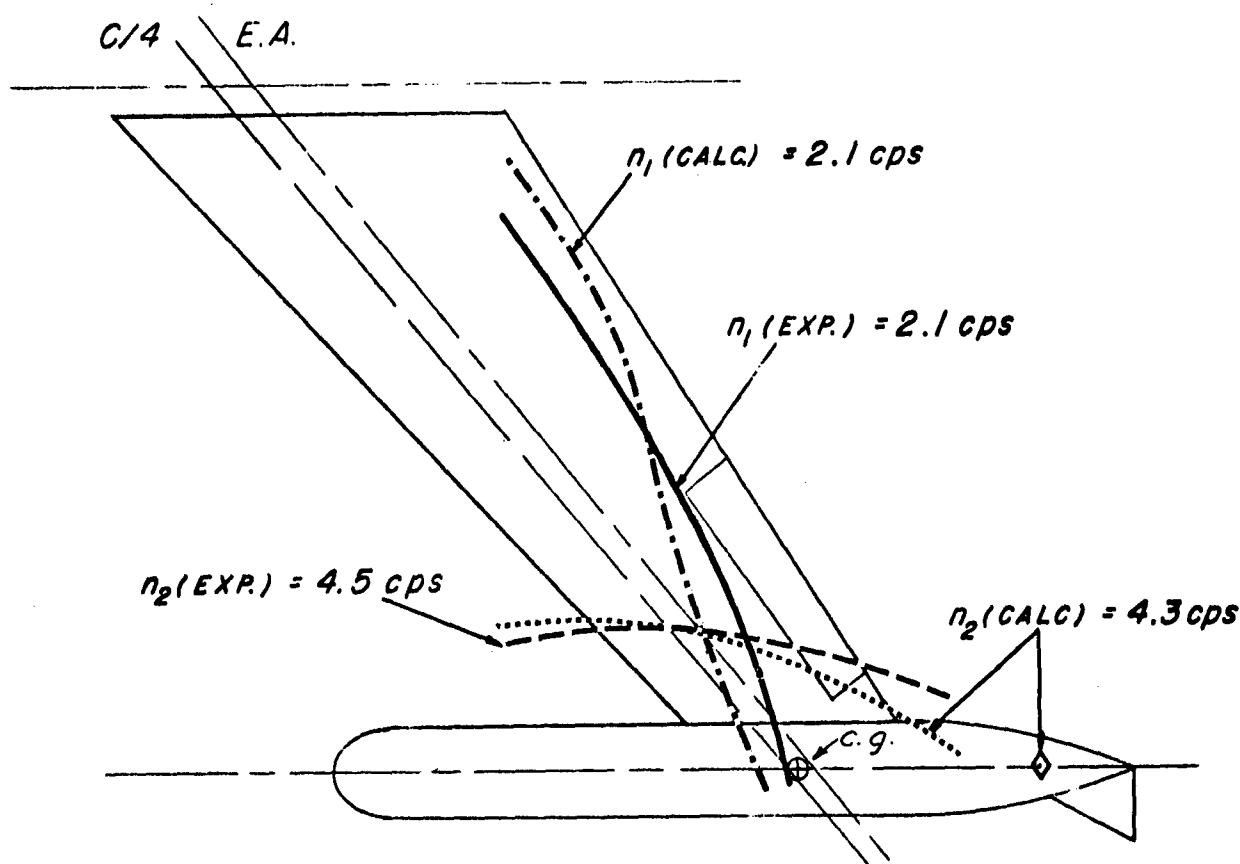
Fig. 28 COUPLED MODE NODAL LINES
CASE 3 ANTISYMMETRIC

UNCLASSIFIED

W_T LB.	S_T LB.-IN.	I_T LB.-IN.^{2}	I_ϕ LB.-IN.^{2}	V_{cr} mph	n_{cr} cps	$V_N / b_r \omega$
51.2	-423	39,520	33,130	174	1.7	26

C/4   E.A.

n_1 (CALC.) = 1.8 cps

n_1 (EXP.) = 1.7 cps

n_2 (EXP.) = 4.2 cps

n_2 (CALC.) = 4.3 cps

c.g.
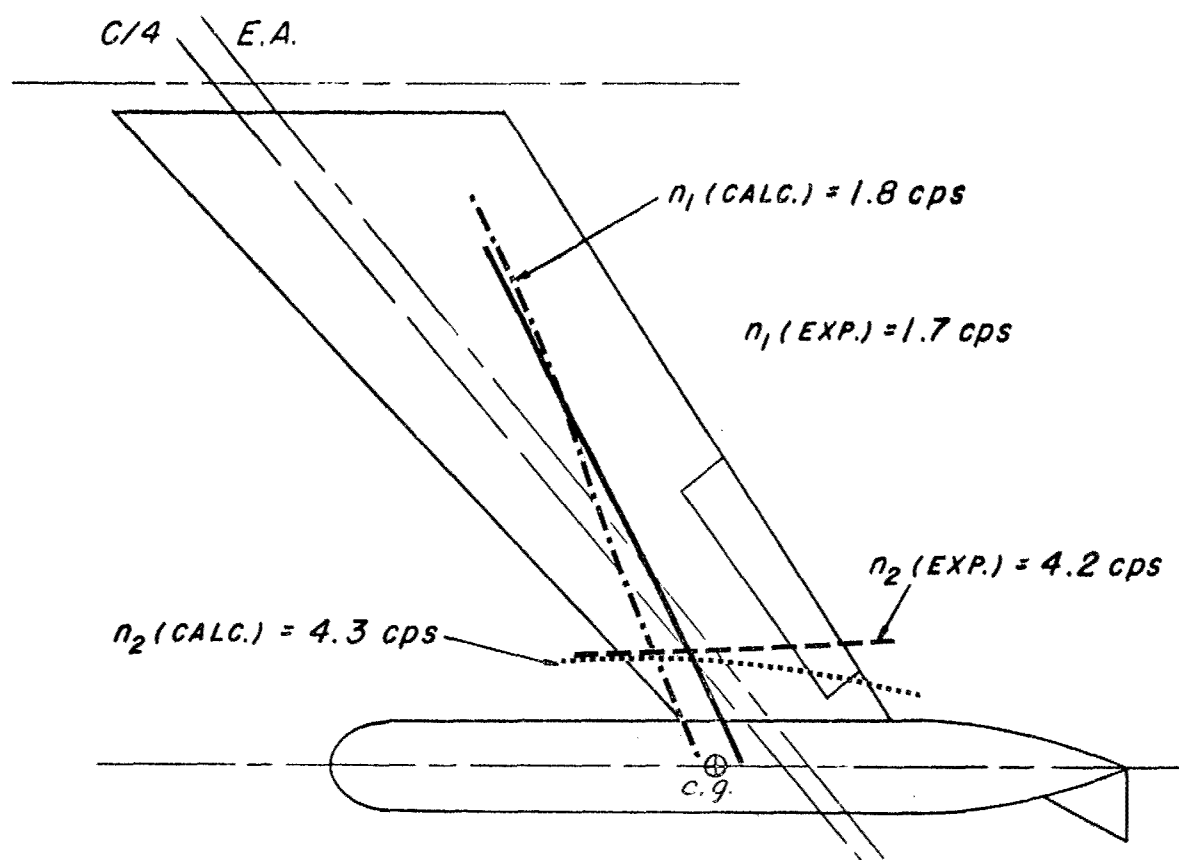
Fig. 29 COUPLED MODE NODAL LINES
CASE 4 ANTISYMMETRIC

W_T LB.	S_T LB.-IN.	I_T LB.-IN.^{2}	I_ϕ LB.-IN.^{2}	V_{cr} mph	n_{cr} cps	$V_N/b_f \omega$
33.2	-320	15050	33130	NO FLUTTER TO 238 mph		
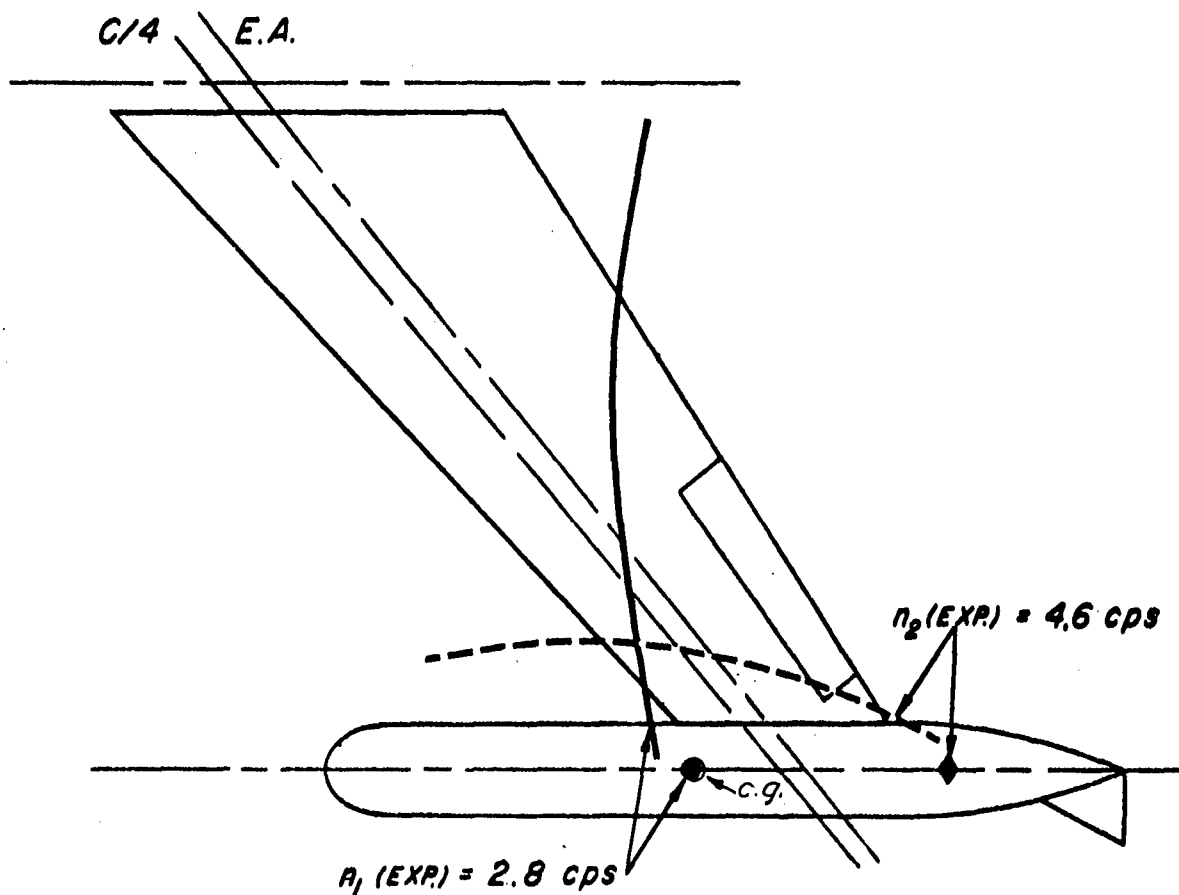
Fig. 30 COUPLED MODE NODAL LINES
CASE 10 ANTISYMMETRIC

W_T LB.	S_T LB.-IN.	I_T LB.-IN.^{2}	I_ϕ LB.-IN.^{2}	V_{cr} mph	n_{cr} cps	$V_N/b_r\omega$
38.9	-135	18,770	33,130	147	2.1	18

C/4   E.A.

$n_1 (EXP.) = 2.3$ cps

$n_2 (EXP.) = 4.5$ cps

c.g.
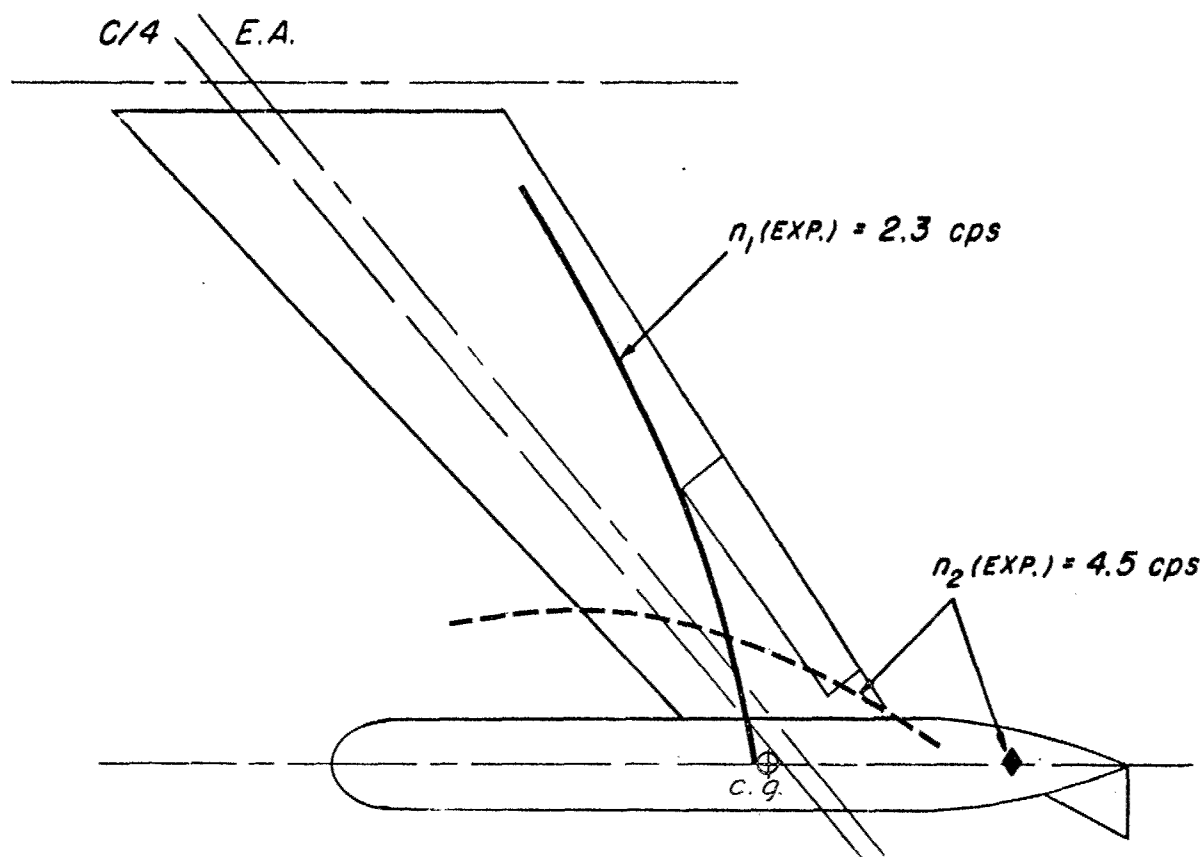
Fig. 31 COUPLED MODE NODAL LINES
CASE 13 ANTISYMMETRIC

W_T LB.	S_T LB.-IN.	I_T LB.-IN.^{2}	I_ϕ LB.-IN.^{2}	V_{cr} mph	n_{cr} cps	$V_N/b_r\omega$
41.2	-468	12040	33130	NO FLUTTER TO 271 mph		

C/4   E.A.

n_1 (EXP.) = 3.6 cps

c.g.

n_2 (EXP.) = 4.8 cps
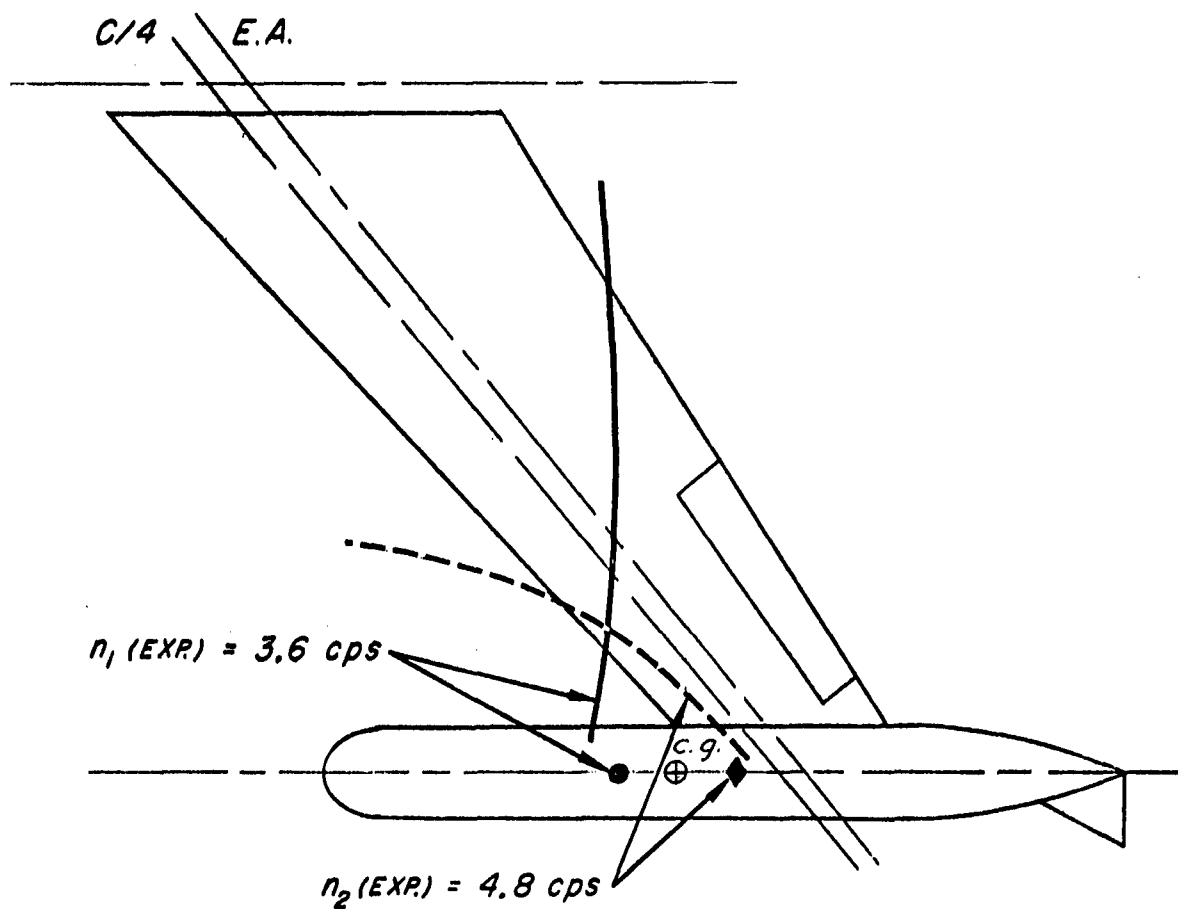
Fig.32 COUPLED MODE NODAL LINES
CASE 18 ANTISYMMETRIC

W_T LB.	S_T LB.-IN.	I_T LB.-IN.^{2}	I_ϕ LB.-IN.^{2}	V_{cr} mph	n_{cr} cps	$V_N/b_r\omega$
41.2	-282	8350	33130	NO FLUTTER TO 229 mph		

C/4   E.A.

$n_1 (EXP.) = 3.4$ cps

$n_2 (EXP.) = 5.1$ cps

c. g.
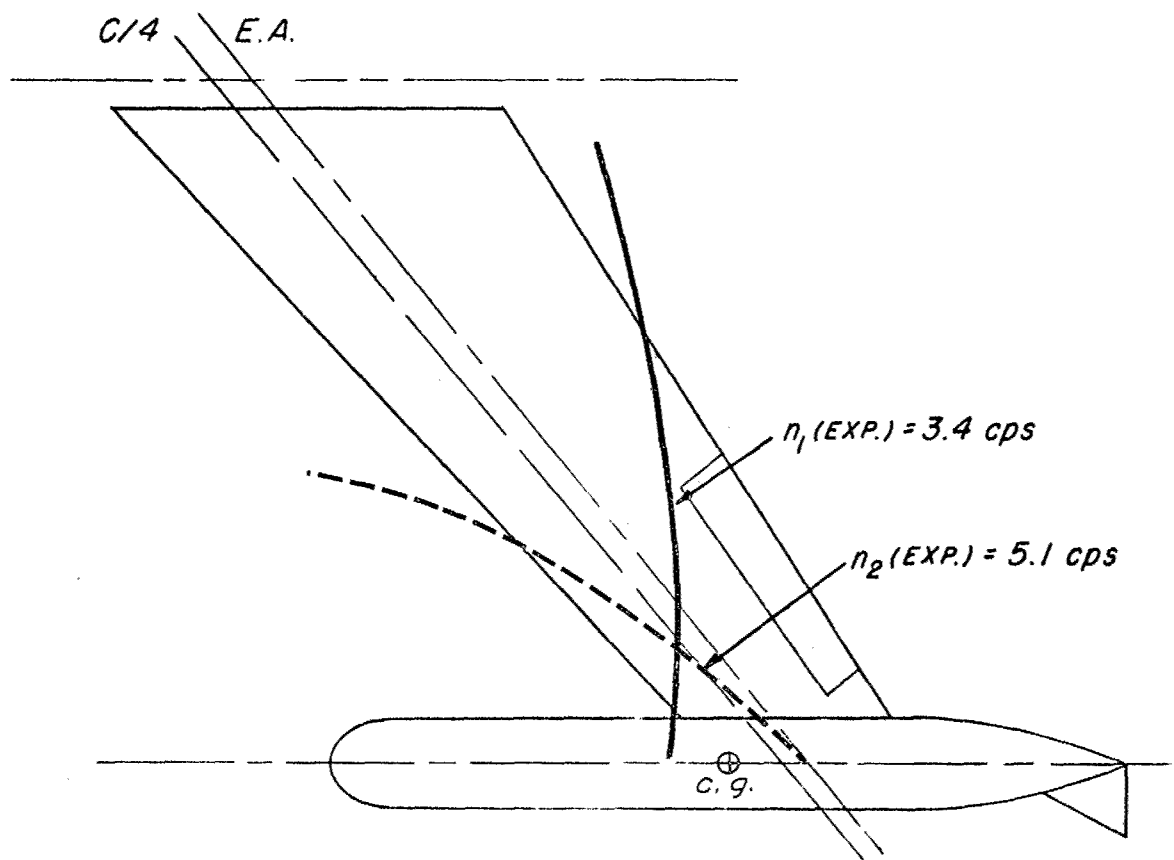
Fig 33 COUPLED MODE NODAL LINES
CASE 19 ANTISYMMETRIC

W_T LB.	S_T LB.-IN.	I_T LB.-IN.^{2}	I_ϕ LB.-IN.^{2}	V_{cr} mph	n_{cr} cps	$V_N/b_f\omega$
55.6	+ 52	15010	33130	132	1.8	18

C/4   E.A.

n_1 (EXP.) = 2.3 cps

n_2 (EXP.) = 4.7 cps

c.g.
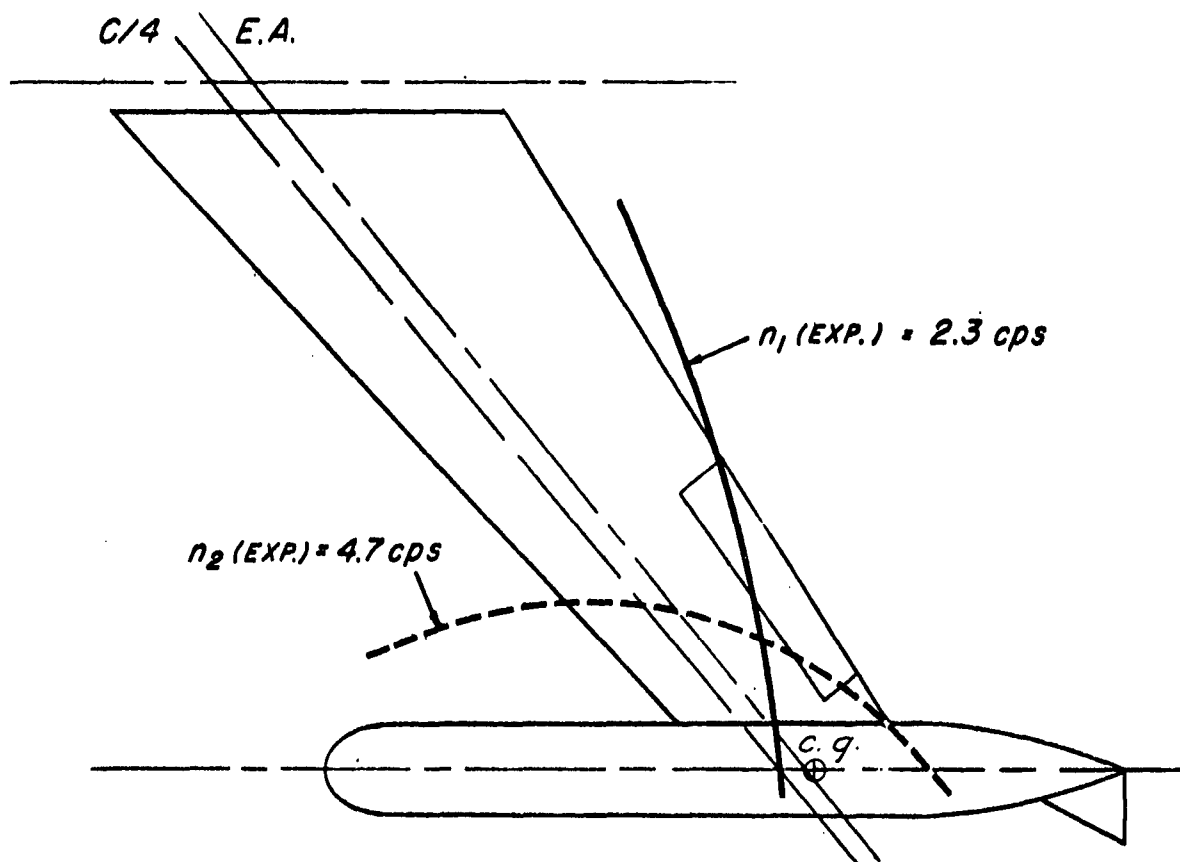
Fig. 34 COUPLED MODE NODAL LINES
CASE 19A ANTISYMMETRIC

W_T LB.	S_T LB.-IN.	I_T LB.-IN.^{2}	I_ϕ LB.-IN.^{2}	V_{cr} mph	n_{cr} cps	$V_N/b_f \omega$
36.3	−767	31610	33130	NO FLUTTER TO		262 mph

C/4   E.A.

$n_2 (EXP.) = 4.3$ cps

$n_1 (EXP.) = 2.6$ cps

c. g.
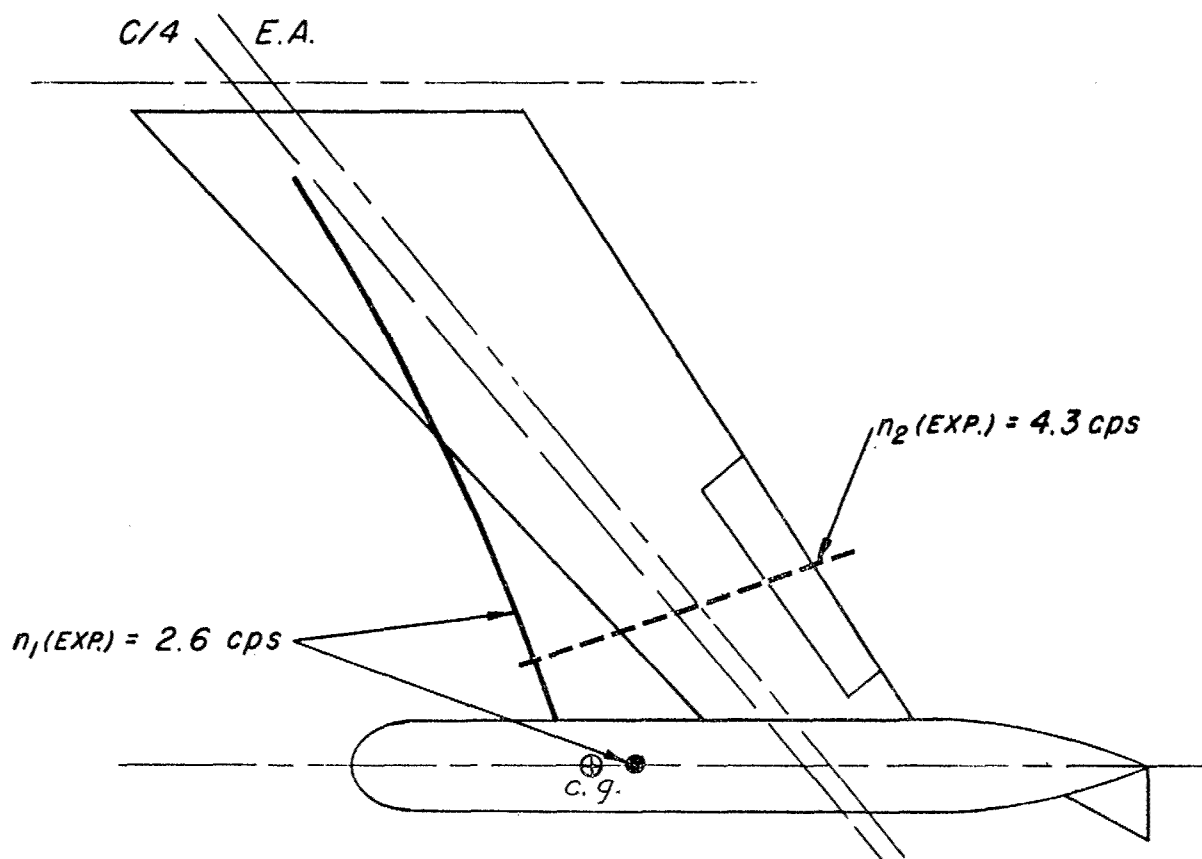
Fig. 35 COUPLED MODE NODAL LINES
CASE 22 ANTISYMMETRIC

W_T LB.	S_T LB.-IN.	I_T LB.-IN.^{2}	I_ϕ LB.-IN.^{2}	V_{cr} mph	n_{cr} cps	$V_N/b_r\omega$
55.6	–133	18,700	33,130	137	1.9	18
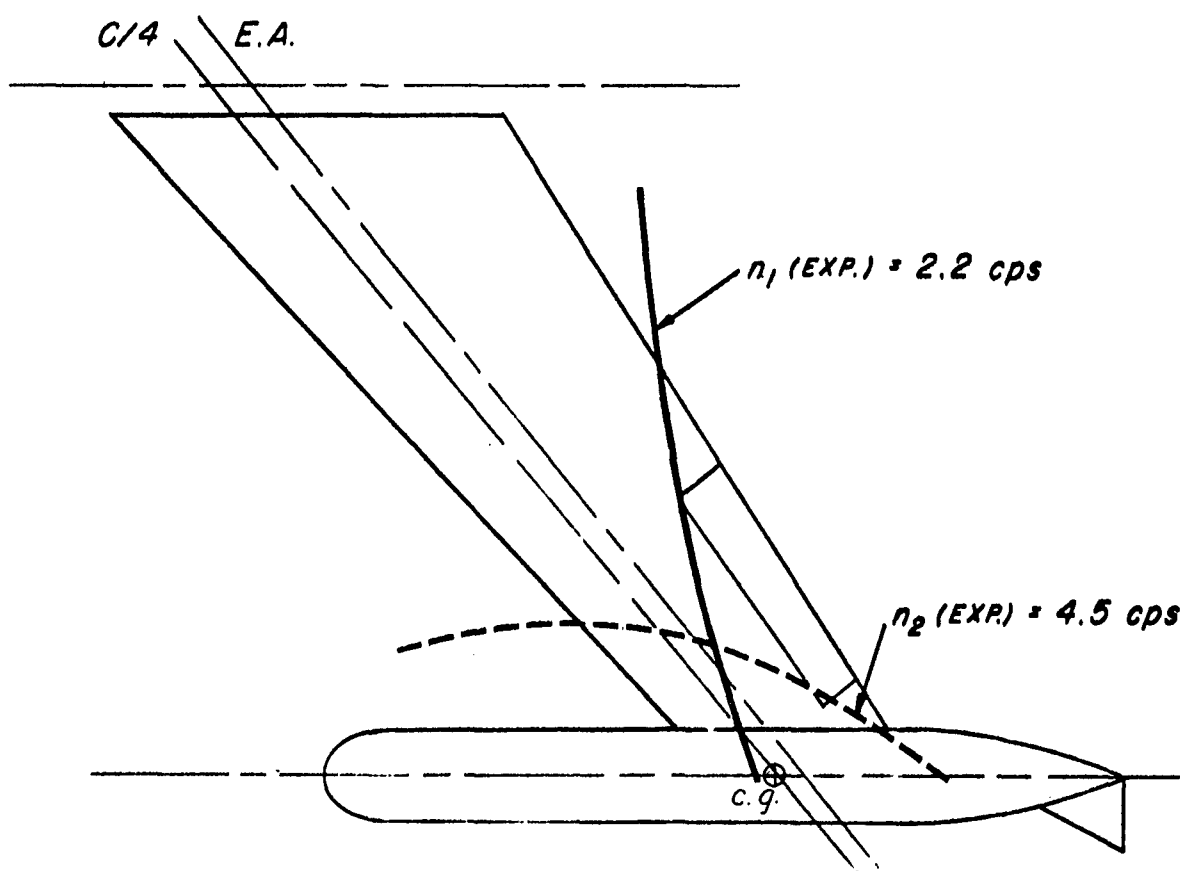
Fig. 36 COUPLED MODE NODAL LINES
CASE 28-1 ANTISYMMETRIC

W_T LB.	S_T LB.-IN.	I_T LB.-IN.^{2}	I_ϕ LB.-IN.^{2}	V_{cr} mph	n_{cr} cps	$V_N/b_r\omega$
21.8	-180	7530	33130	243	5.0	12

C/4   E.A.

n_2 (EXP.) = 5.2 cps

n_1 (EXP.) = 3.6 cps

c.g.
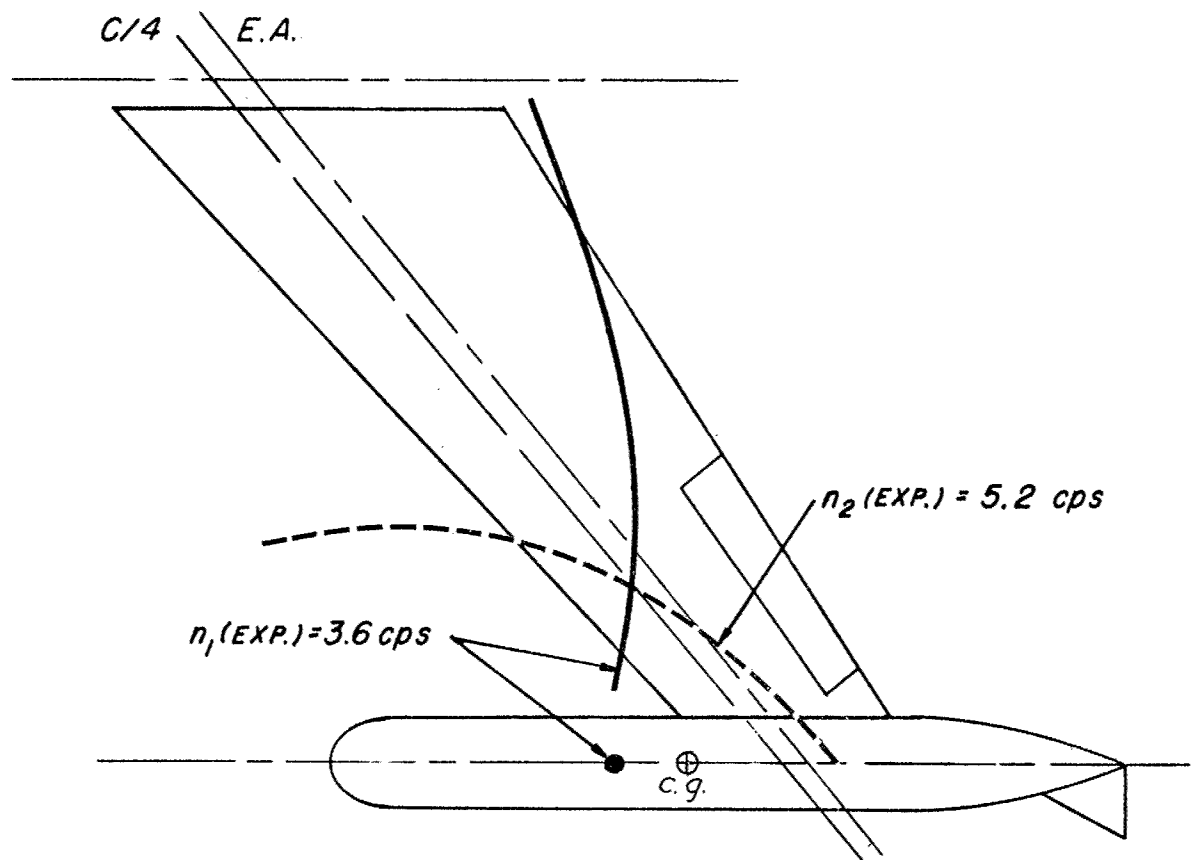
Fig. 37 COUPLED MODE NODAL LINES
CASE 31 ANTISYMMETRIC

W_T LB.	S_T LB.-IN.	I_T LB.-IN.^{2}	I_ϕ LB.-IN.^{2}	V_{cr} mph	n_{cr} cps	$V_N/b_r\omega$
41.2	-468	12040	41470	NO FLUTTER TO 242 mph		

C/4   E.A.

n_2 (EXP) = 4.6 cps

n_1 (EXP.) = 3.4 cps

c.g.
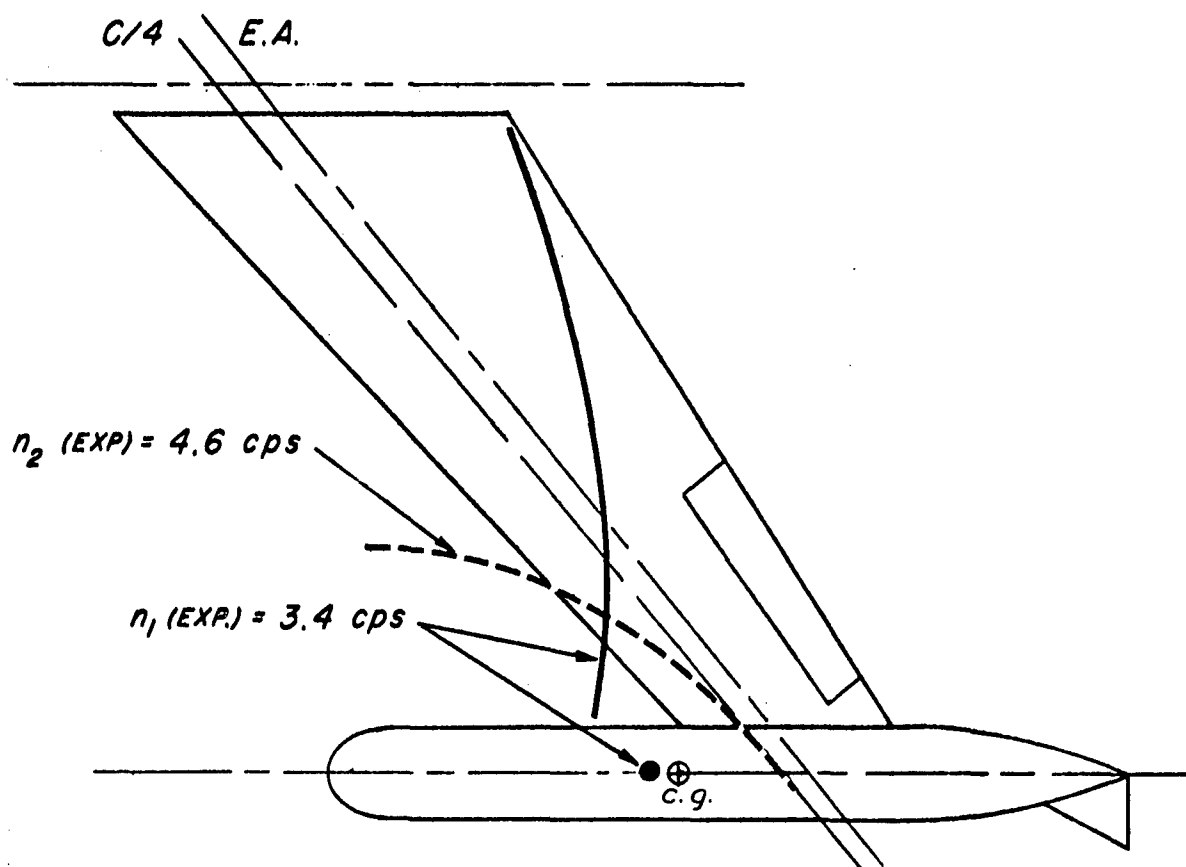
Fig. 38 COUPLED MODE NODAL LINES
CASE 18 - 2 ANTISYMMETRIC

W_T LB.	S_T LB.-IN.	I_T LB.-IN.^{2}	I_ϕ LB.-IN.^{2}	V_{cr} mph	n_{cr} cps	$V_N/b_r\omega$
55.6	-133	18700	41470	147	1.8	21

C/4   E.A.

$n_1 (EXP.) = 2.2\ cps$

$n_2 (EXP.) = 4.2\ cps$

c.g.
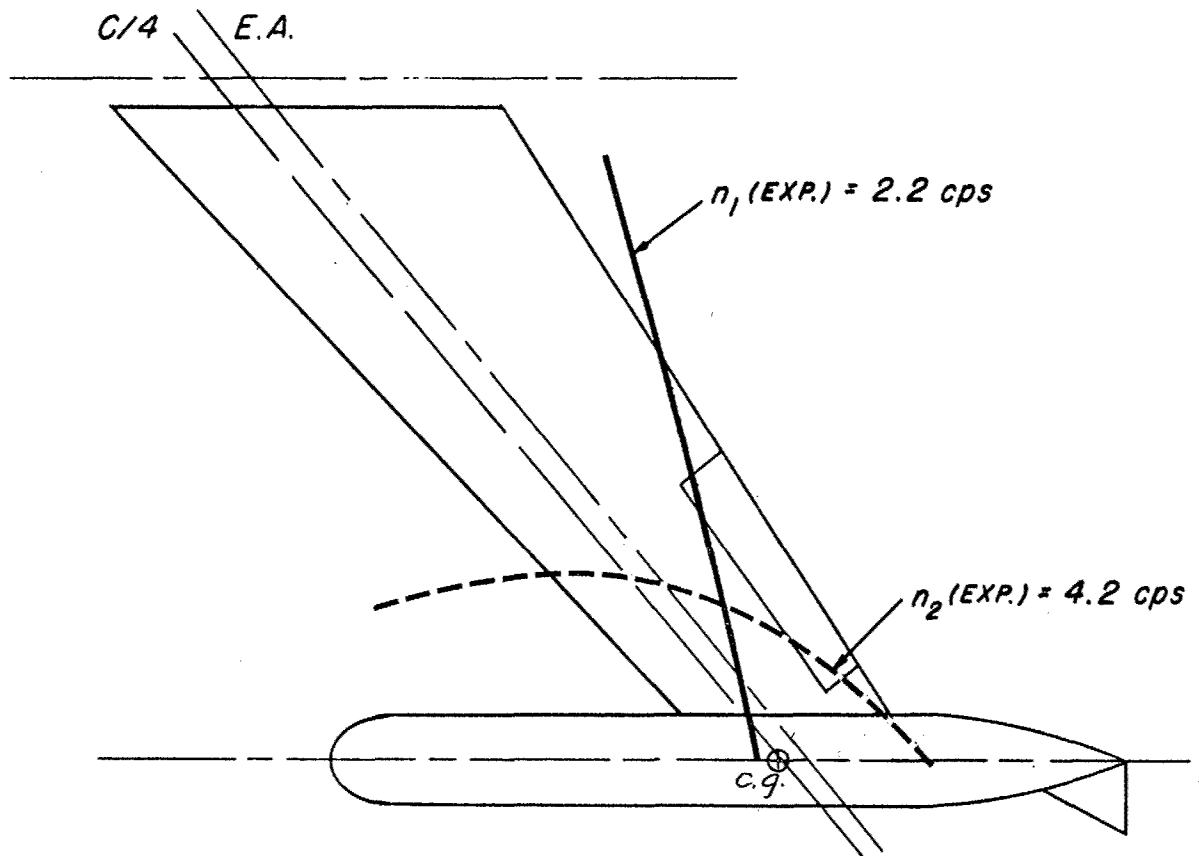
Fig. 39 COUPLED MODE NODAL LINES
CASE 28 ANTISYMMETRIC

W_T LB.	S_T LB.-IN.	I_T LB.-IN.^{2}	I_ϕ LB.-IN.^{2}	V_{cr} mph	n_{cr} cps	$V_N/b_r\omega$
46.5	+166	21,890	57,200	119	1.6	19

C/4   E.A.

$n_1 (EXP.) = 1.9$ cps

$n_2 (EXP.) = 4.1$ cps

c.g.
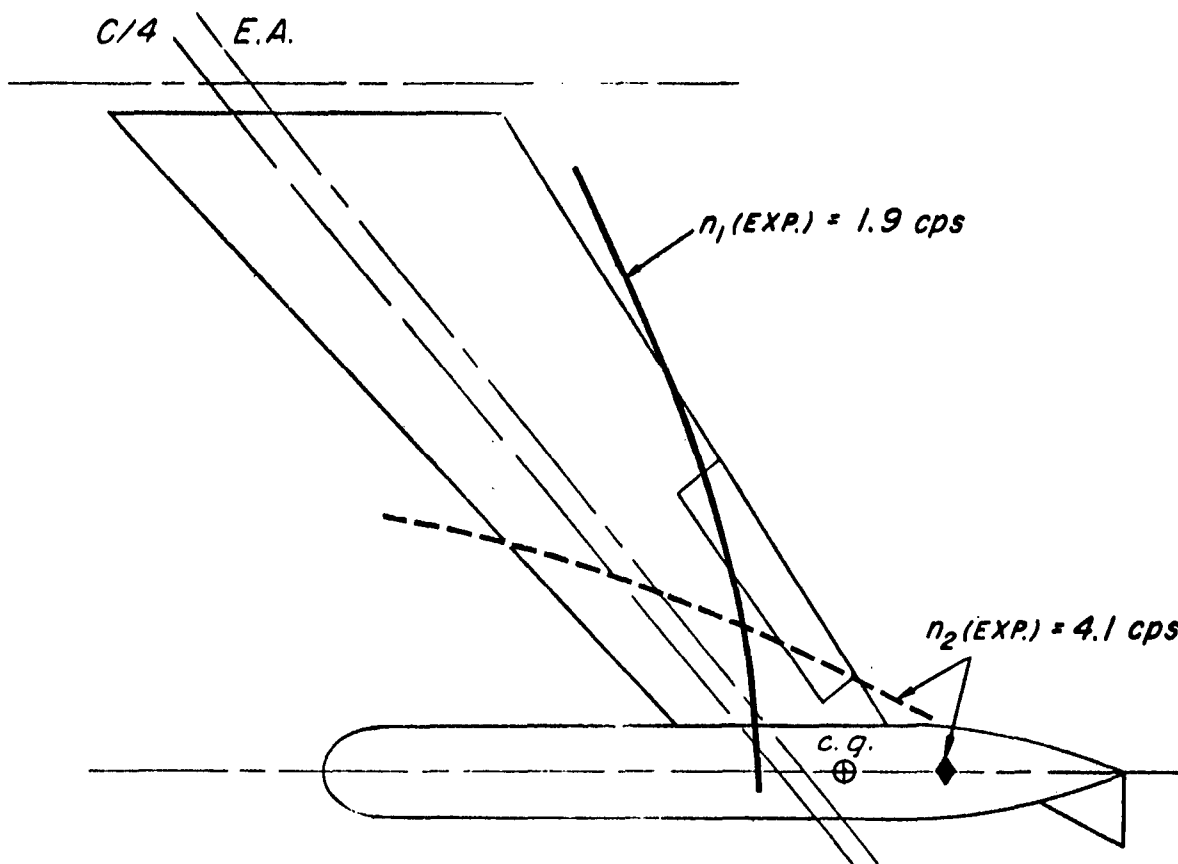
Fig. 40 COUPLED MODE NODAL LINES
CASE 15A ANTISYMMETRIC

W_T LB.	S_T LB.-IN.	I_T LB.-IN.^{2}	I_ϕ LB.-IN.^{2}	V_{cr} mph	n_{cr} cps	$V_N/b_r\omega$
51.0	−635	14,690	57,200	NO FLUTTER TO 265 mph		
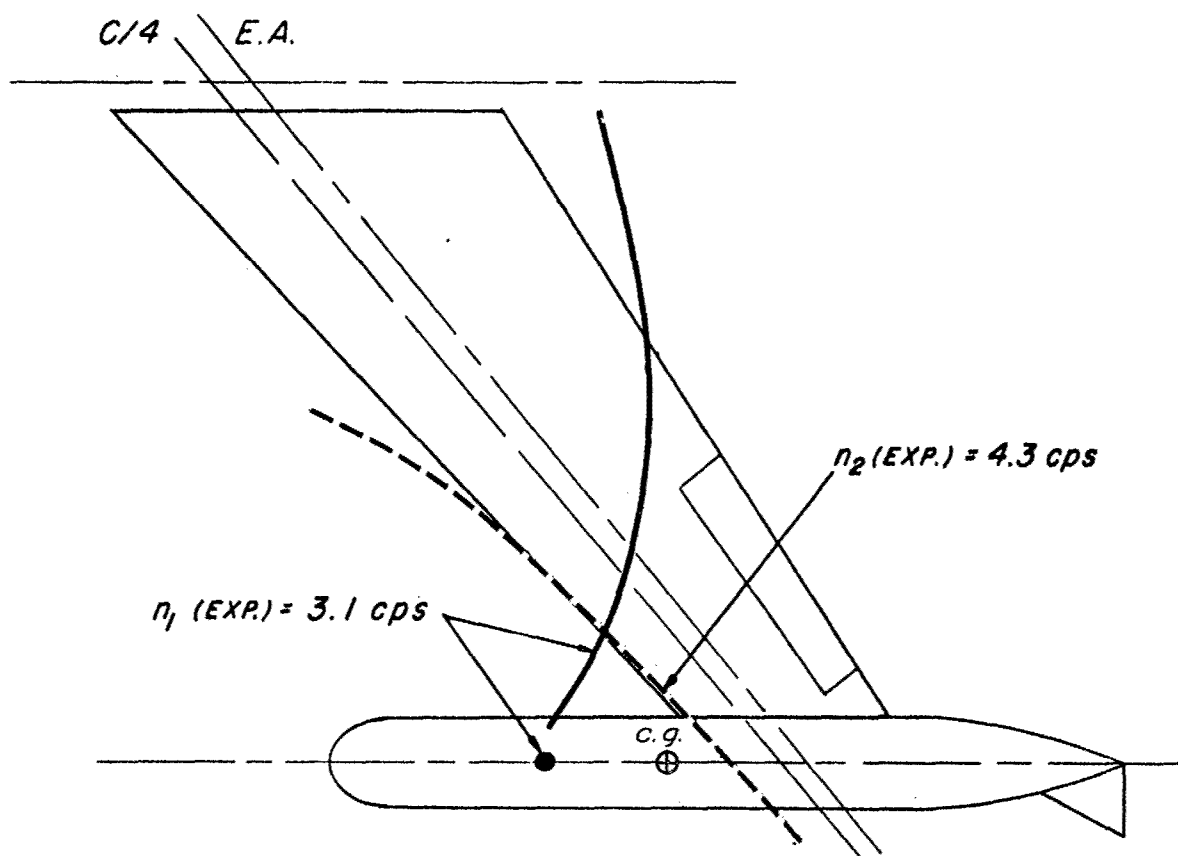
Fig. 41   COUPLED MODE NODAL LINES
CASE 30 ANTISYMMETRIC

Testing technique was similar to that used during the tests of Part 1 of this program. Excitation of the model in all configurations was achieved manually by means of a string attached to the front flutter brake pylon on the tip pod. Fig. 42 shows a typical flutter record.

Tables 6, 7, and 8 give a summary of flutter test data. The values of $V_N/b_r\omega$ listed here are based on a reference semi-chord normal to the elastic axis at the three-quarter span, and the component of the free stream velocity normal to the elastic axis.

IV. VIBRATION ANALYSES

During the vibration analyses of Part 1 of this program, it was found that for straight wings with heavy tip pods, the first uncoupled cantilever bending and torsion mode shapes varied only slightly with changing tip pod mass parameters. Furthermore, uncoupled modes higher than the first bending and torsion modes were found to have negligible effect in either the vibration or flutter analyses because of the high frequencies associated with such modes. Analyses for the swept wing configurations showed that a similar trend could be expected. In view of this, all vibration and flutter analyses of the swept wing model were made incorporating only the first uncoupled cantilever bending and torsion modes together with the appropriate rigid body degrees of freedom.

Cases 3 and 4, for which positive flutter points were obtained with cantilever, symmetric, and antisymmetric root conditions and which had considerable variation in tip pod mass properties, were chosen for vibration and flutter analyses. Case 3 was used as a basic configuration. Using the flexural and torsional rigidity distributions of Figs. 6 and 7, pp. 11 and 12, the uncoupled cantilever bending and the uncoupled cantilever torsion frequencies and mode shapes were computed by standard methods. The resulting normalized mode shapes are shown in Figs. 43 and 44.

The vibration analyses indicated that the wing mass effects were small compared to those of the tip pod. In consequence of this and the assumption of constant mode shapes, it was possible, with only small errors, to simplify the computation of first uncoupled cantilever bending and torsion frequencies for the various configurations by replacing the wing with a weightless spring and a constant equivalent effective mass at the tip which was combined with the various tip pod mass parameters.
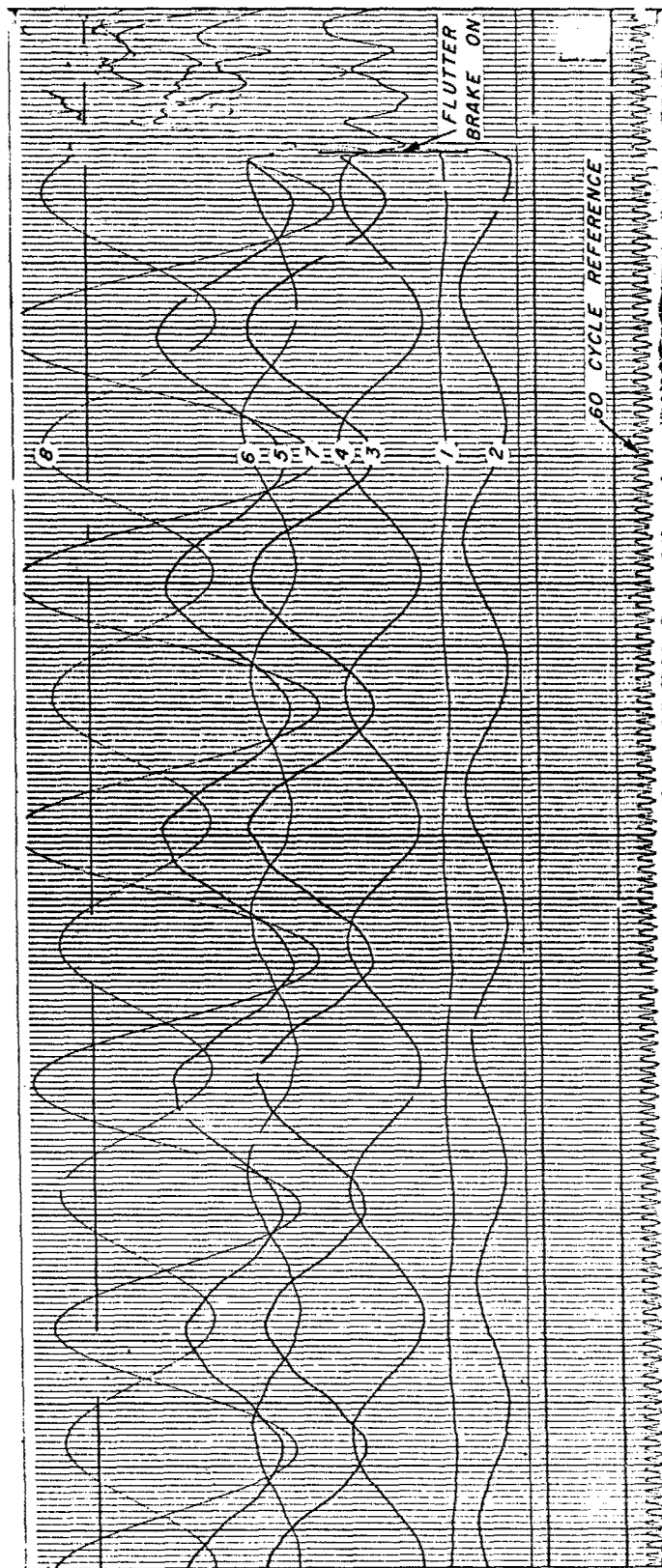
TRACES 1 TO 6 - WING STATIONS
TRACES 7 AND 8 - TIP POD STATIONS

Fig. 42 TYPICAL FLUTTER RECORD
CASE 13 CANTILEVER
$V_{CR} = 124$ mph $n_{CR} = 2.5$ cps

TABLE 6

SUMMARY OF FLUTTER TEST DATA - CANTILEVER CASES

CASE	V_{cr} mph	n_{cr} cps	$V_N/b_r\omega = V_{cr}\cos\Lambda/b_r\omega$
3	124	2.3	14
4	89	1.9	12
4A	90	1.7	13
10	130	3.0	11
13	124	2.5	12

TABLE 7

SUMMARY OF FLUTTER TEST DATA - SYMMETRIC CASES

CASE	V_{cr} mph	n_{cr} cps	$V_N/b_r\omega = V_{cr}\cos\Lambda/b_r\omega$
3	150	2.4	16
4	138	1.9	18
4A	139	1.8	19
12	120	2.8	11
22	160	2.2	18
22A	No flutter to 257 mph		
33	No flutter to 155 mph		
33A	165	3.2	13
33B	175	2.6	17
33C	151.5	2.0	19
100	230	3.7	16

TABLE 8

SUMMARY OF FLUTTER TEST DATA -- ANTISYMMETRIC CASES

CASE	V_{cr} mph	n_{cr} cps	$V_N/b_r\omega = V_{cr}\cos\wedge/b_r\omega$
3	124	1.8	17
4	174	1.7	26
10	No flutter to 238 mph		
13	147	2.1	18
15	108	1.7	16
15A	119	1.6	19
15B	107	1.7	16
18	No flutter to 271 mph		
18-1	No flutter to 221 mph		
18-2	No flutter to 242 mph		
19	No flutter to 229 mph		
19A	132	1.8	18
22	No flutter to 262 mph		
28	147	1.8	21
28-1	137	1.9	18
30	No flutter to 265 mph		
31	243	5.0	12
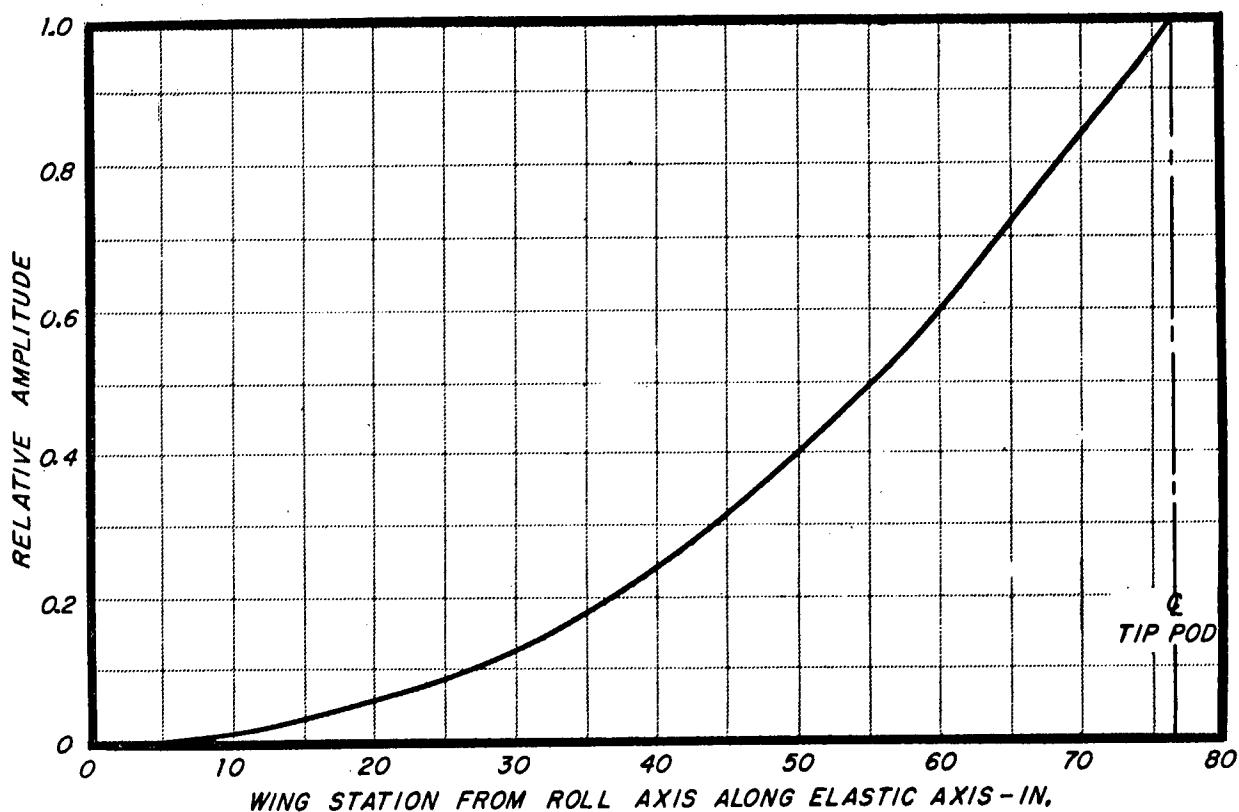
Fig. 43   FIRST UNCOUPLED CANTILEVER BENDING MODE SHAPE
CASE 3
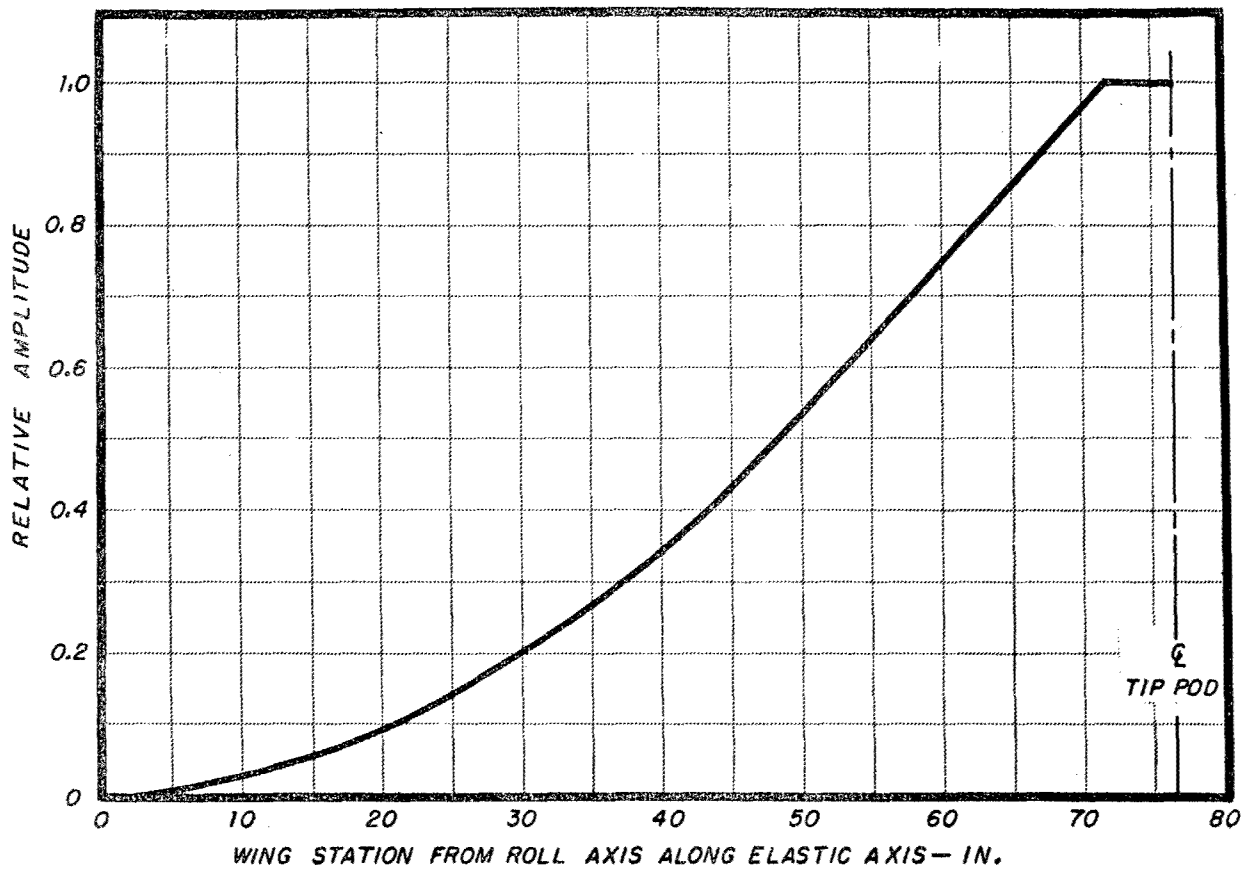
Fig. 44 FIRST UNCOUPLED CANTILEVER TORSION MODE SHAPE
CASE 3

The first uncoupled cantilever torsion and bending modes and the appropriate rigid body modes were used as generalized coordinates and coupled in the usual fashion to compute normal modes for cases 3 and 4 in the cantilever, symmetric, and antisymmetric configurations. The frequencies and nodal lines thus computed are shown on the appropriate figures in Section II, where they may be compared to experimental results.

V. FLUTTER ANALYSES

Analyses based on two dimensional aerodynamic coefficients, and analyses based on finite wing theory were made of cases 3 and 4 symmetric, antisymmetric, and cantilever. In all cases, the velocity component method of analysis of Ref. 4 was used. Figure 45 shows the wing plan form on which the analyses were based, as well as the coordinate system used.

In the finite wing analyses, a reflection plane was assumed at the wing root normal to the elastic axis, rather than in the free stream direction as was actually the case with the tunnel ceiling. This allowed the finite wing theory of Part 1 of this program to be used directly in velocity component analyses.

For the purposes of computing static circulation ratios for aspect ratio corrections, the wing tip was assumed to extend to the intersection of the wing elastic axis and the outer edge of the tip pod (see A, Fig. 45). However, in the finite wing analyses, in the computation of aerodynamic forces and moments, the wing was assumed to extend only to the center line of the tip pod (B, Fig. 45). Analyses were also made using the same static circulation ratios, but with the aerodynamic forces and moments based on a wing extending only to the inner edge of the tip pod (C, Fig. 45).

As customary, only spanwise flow corrections to the aerodynamic forces due to bending deflections were applied to the analysis, spanwise flow corrections due to torsional deflections being neglected.

Tip pod aerodynamics derived from slender body theory for the portion of the tip pod forward of the wing leading edge were included in all analyses. In the derivation, circulation and shed vorticity effects were neglected, as was the case in the tip pod aerodynamics used in the analyses of Part 1 of this program.

The analyses of the cantilever cases were based on the first uncoupled cantilever bending and torsion modes. The analyses of the symmetric cases
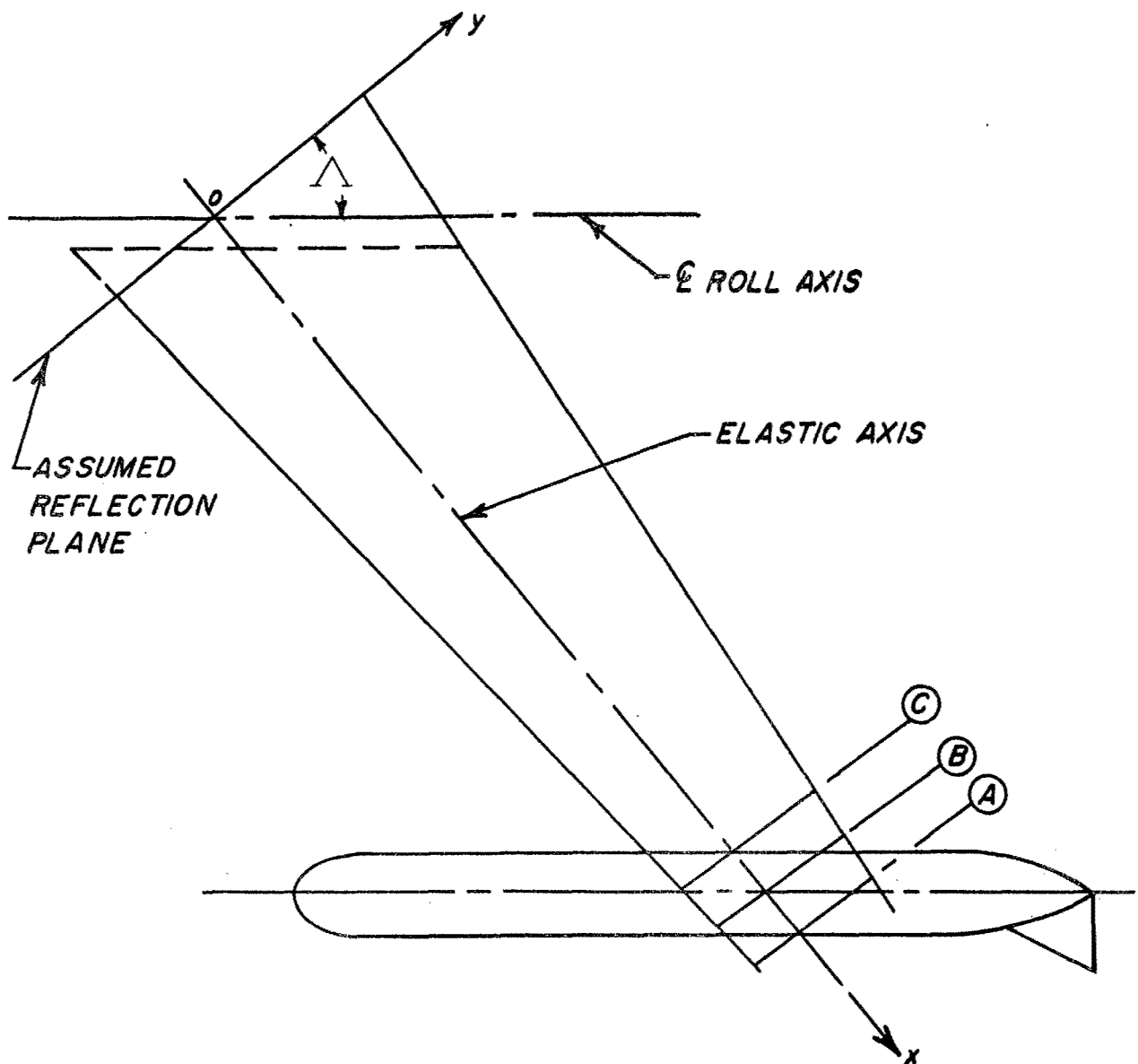
FIG. 45

WING PLAN FORMS CONSIDERED IN FLUTTER ANALYSES

(A) Wing tip assumed in computing static circulation ratios for aspect
     ratio corrections.
(B) Wing tip assumed for two dimensional and some finite wing analyses.
(C) Wing tip assumed for remaining finite wing analyses.

incorporated the above cantilever modes plus rigid body translation and rigid body pitch modes. The antisymmetric analyses included the rigid body roll mode in addition to the uncoupled cantilever modes.

The structural damping coefficients used in the analyses were as follows: 0.01 in the first bending mode, 0.01 in the first torsion mode (except for case 3 symmetric, in which 0.015 was used), 0.1 in the pitch mode, 0.25 in the translation mode, and 0.05 in the roll mode. These coefficients correspond closely to experimental values.

The results of these analyses are shown in Figs. 46 to 51 and in Table 9. Formulae for the aerodynamic and mechanical terms used in the analyses are given in Appendix I.

It should be noted that, in addition to inherent differences between flutter analyses of straight and swept wings, the analyses of Parts 1 and 2 of this report differ in several other respects. In Part 2, to avoid the complexities arising from the geometric coupling due to sweep, the uncoupled elastic modes used in all analyses were uncoupled cantilever modes. In Part 1, the uncoupled elastic modes used in the analysis of each configuration included its appropriate root freedoms. In addition, the following differences are noted:

Flutter Analyses - Two Dimensional Aerodynamic Coefficients

Part 1	Part 2
Wing tip assumed at outer edge of tip pod	Wing tip assumed at intersection of tip pod ₵ and e.a.
Tip pod aerodynamics not included	Tip pod aerodynamics included

Flutter Analyses - Finite Wing Aerodynamic Coefficients

Part 1	Part 2
Wing tip assumed at inner edge of tip pod	Wing tip assumed at intersection of tip pod ₵ and e.a. In some analyses, where so noted, wing tip assumed at intersection of inner edge of tip pod and e.a.
Tip pod aerodynamics included	Tip pod aerodynamics included

TYPE OF ANALYSIS	$(\omega_h/\omega_a)_{CANT}$ (THEOR.)	$V_N/b_r(\omega_a)_{CANT}$ AT FLUTTER		$V_N/b_r\omega$ AT FLUTTER		FLUTTER SPEED-mph		FLUTTER FREQ-cps.	
		CALC.	EXP.	CALC.	EXP.	CALC.	EXP.	CALC.	EXP.
2 DIM.	0.52	10.7	11.5	14.3	14	115	124	2.03	2.3
AR CORR	0.52	11.8	11.5	16.6	14	127	124	1.93	2.3
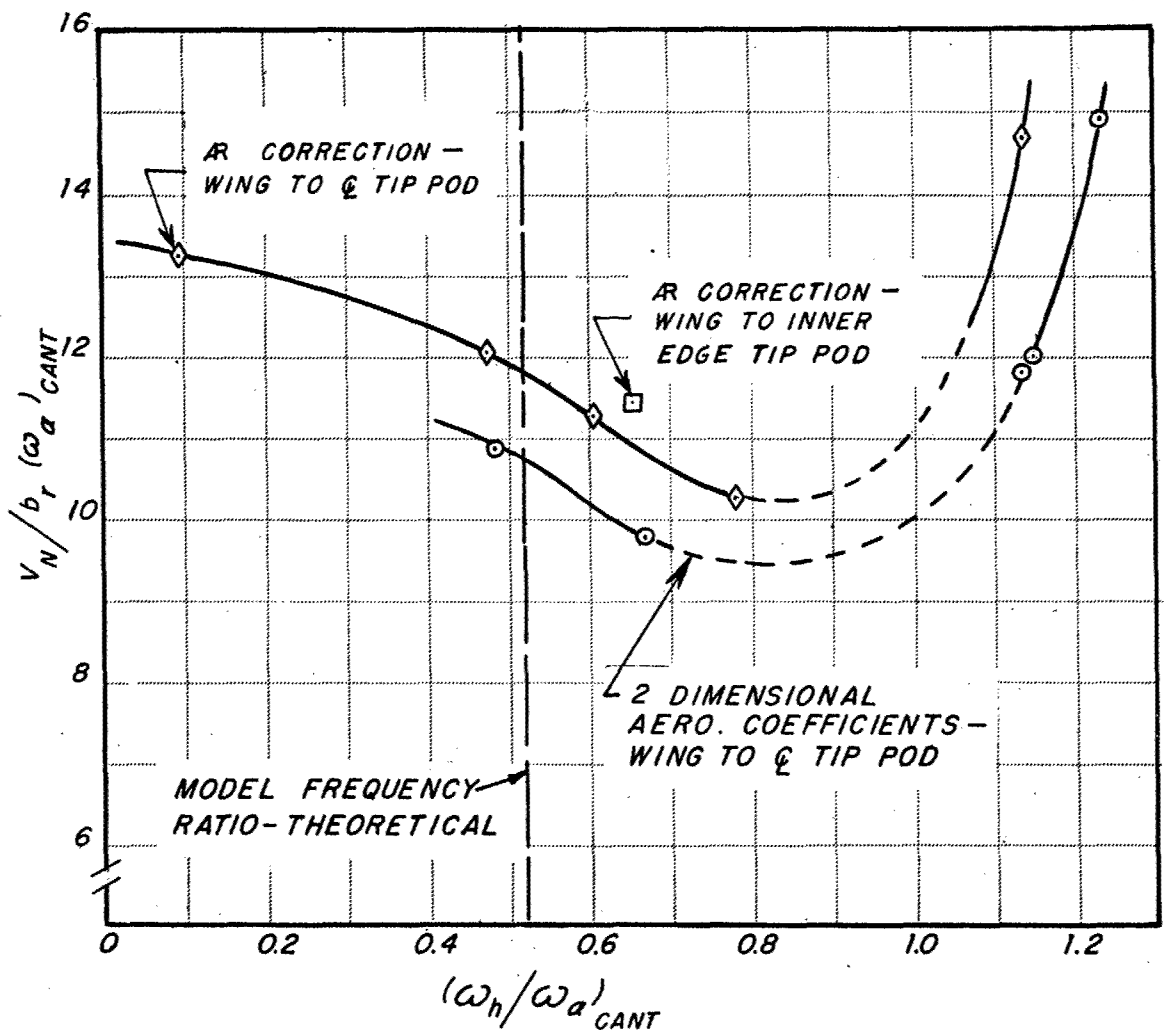
Fig.46 $V_N/b_r(\omega_a)_{CANT}$ vs $(\omega_h/\omega_a)_{CANT}$

CASE 3 CANTILEVER

TYPE OF ANALYSIS	$(\omega_h/\omega_a)_{CANT}$ (THEOR.)	$V_N/b_r(\omega_a)_{CANT}$ AT FLUTTER		$V_N/b_r\omega$ AT FLUTTER		FLUTTER SPEED-mph		FLUTTER FREQ-cps.	
		CALC.	EXP.	CALC.	EXP.	CALC.	EXP.	CALC.	EXP.
2 DIM.	0.67	11.3	10.8	13.0	12	93	89	1.81	1.9
AR CORR.	0.67	12.8	10.8	14.6	12	106	89	1.82	1.9
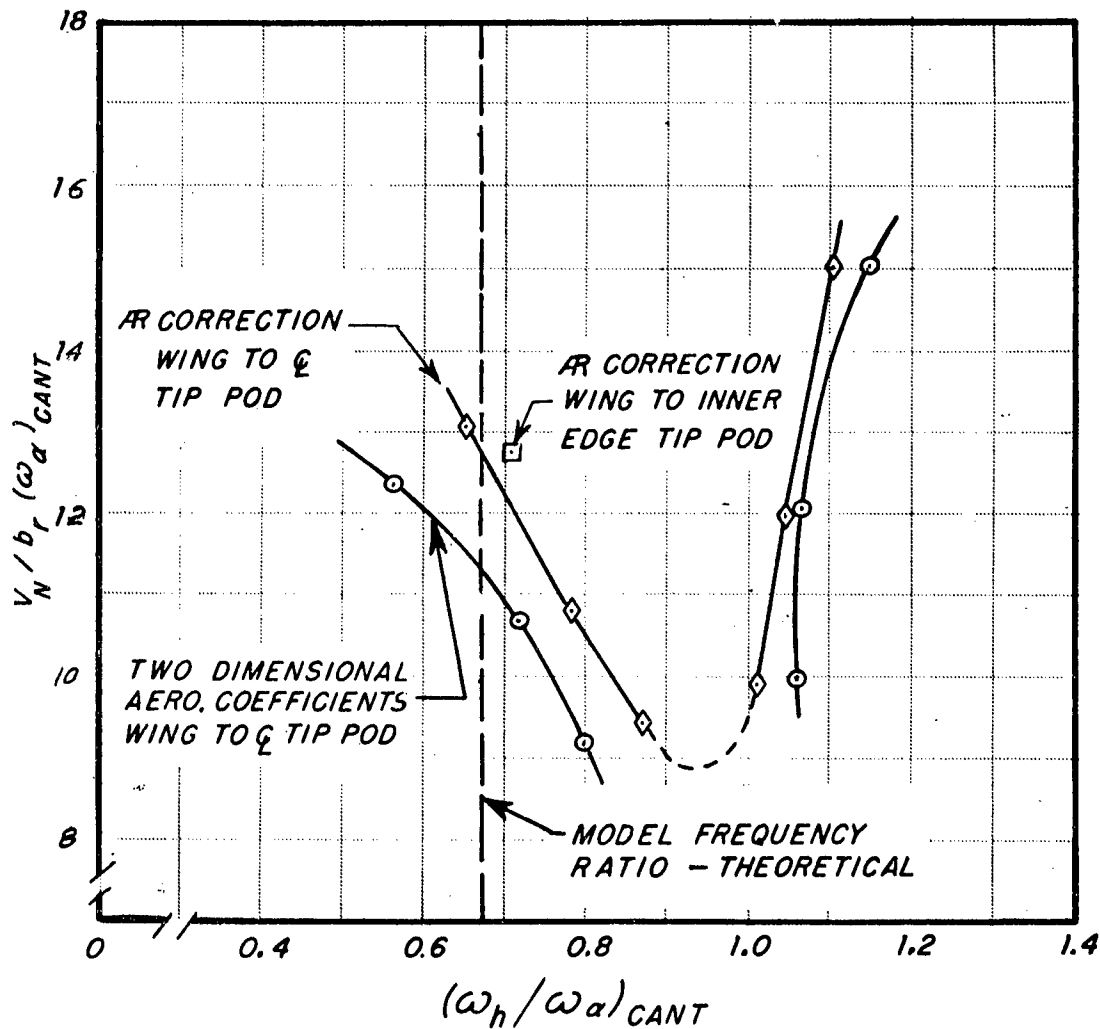
Fig. 47 $V_N/b_r(\omega_{a_{CANT}})$ vs $(\omega_h/\omega_a)_{CANT}$

CASE 4 CANTILEVER

TYPE OF ANALYSIS	$(\omega_h/\omega_a)_{CANT}$ (THEOR.)	$V_N/b_r(\omega_a)_{CANT}$ AT FLUTTER		$V_N/b_r\omega$ AT FLUTTER		FLUTTER SPEED -mph		FLUTTER FREQ - cps.	
		CALC.	EXP.	CALC.	EXP.	CALC.	EXP.	CALC.	EXP.
2 DIM.	.52	13.7	13.9	15.6	16	148	150	2.38	2.4
AR CORR.	.52	16.1	13.9	19.8	16	174	150	2.20	2.4

ANALYSIS FOR TRANSLATION - PITCH - FIRST UNCOUPLED
CANTILEVER BENDING - FIRST UNCOUPLED CANTILEVER TORSION

Fig. 48 $V_N/b_r (\omega_a)_{CANT}$ vs $(\omega_h/\omega_a)_{CANT}$

CASE 3 SYMMETRIC

TYPE OF ANALYSIS	$(\omega_h/\omega_a)_{CANT}$ (THEOR.)	$V_N/b_r(\omega_a)_{CANT}$ AT FLUTTER		$V_N/b_r\omega$ AT FLUTTER		FLUTTER SPEED-mph		FLUTTER FREQ-cps.	
		CALC.	EXP.	CALC.	EXP.	CALC.	EXP.	CALC.	EXP.
2 DIM.	0.67	17.4	16.7	20.8	18	144	138	1.74	1.9
AR - WING TO ¢	0.67	19.7	16.7	22.2	18	162	138	1.84	1.9
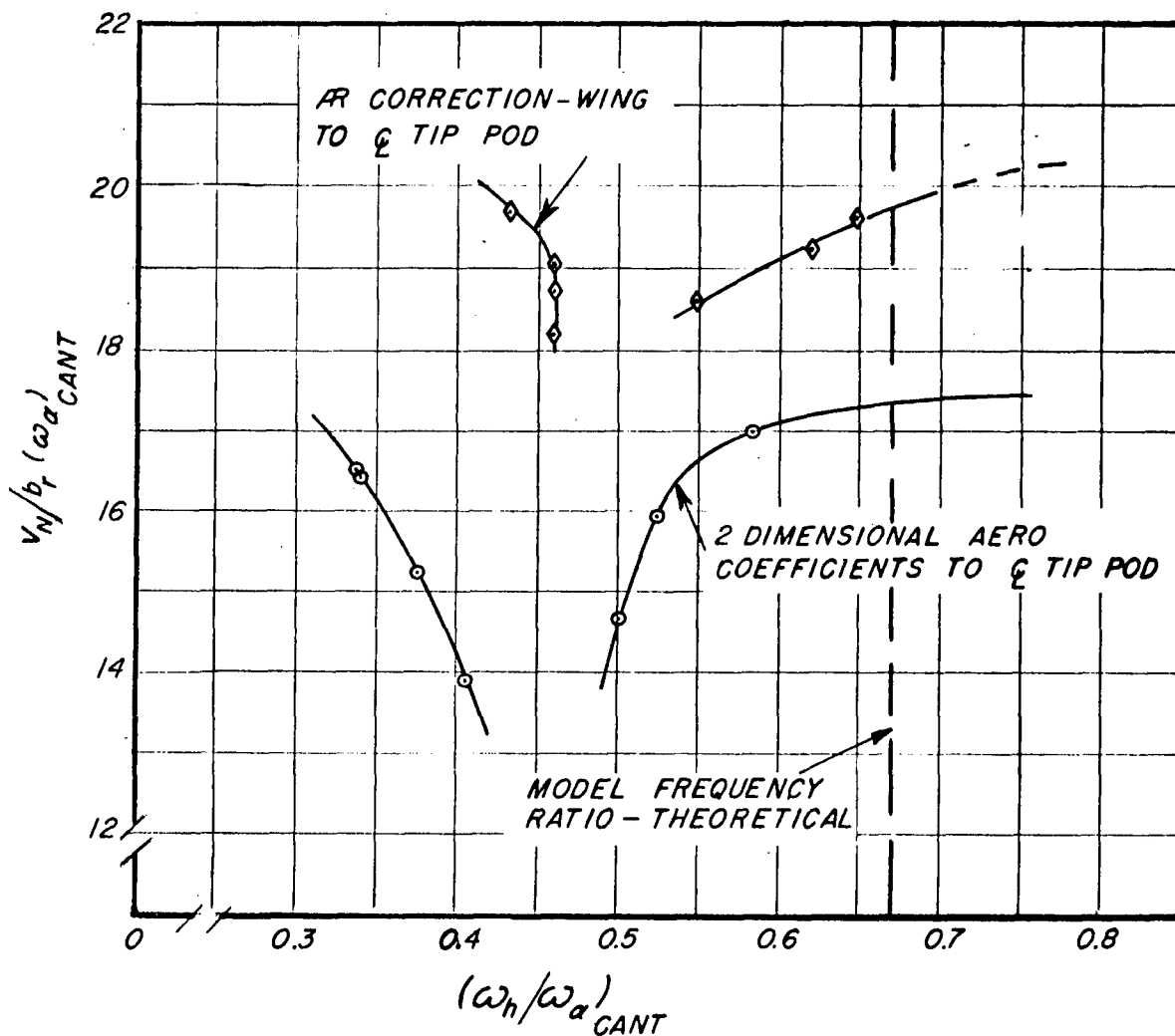
ANALYSIS FOR TRANSLATION - PITCH - FIRST UNCOUPLED
CANTILEVER BENDING - FIRST UNCOUPLED CANTILEVER TORSION

Fig. 49 $V_N/b_r(\omega_a)_{CANT}$ vs $(\omega_h/\omega_a)_{CANT}$

CASE 4 SYMMETRIC

TYPE OF ANALYSIS	$(\omega_h/\omega_a)_{CANT}$ (THEOR.)	$V_N/b_r(\omega_a)_{CANT}$ AT FLUTTER		$V_N/b_r\omega$ AT FLUTTER		FLUTTER SPEED-mph		FLUTTER FREQ-cps.	
		CALC.	EXP.	CALC.	EXP.	CALC.	EXP.	CALC.	EXP.
2 DIM	0.52	12.2	11.5	18.7	17	132	124	1.77	1.8
AR CORR. WING TO ₵	0.52	13.9	11.5	24.5	17	150	124	1.54	1.8
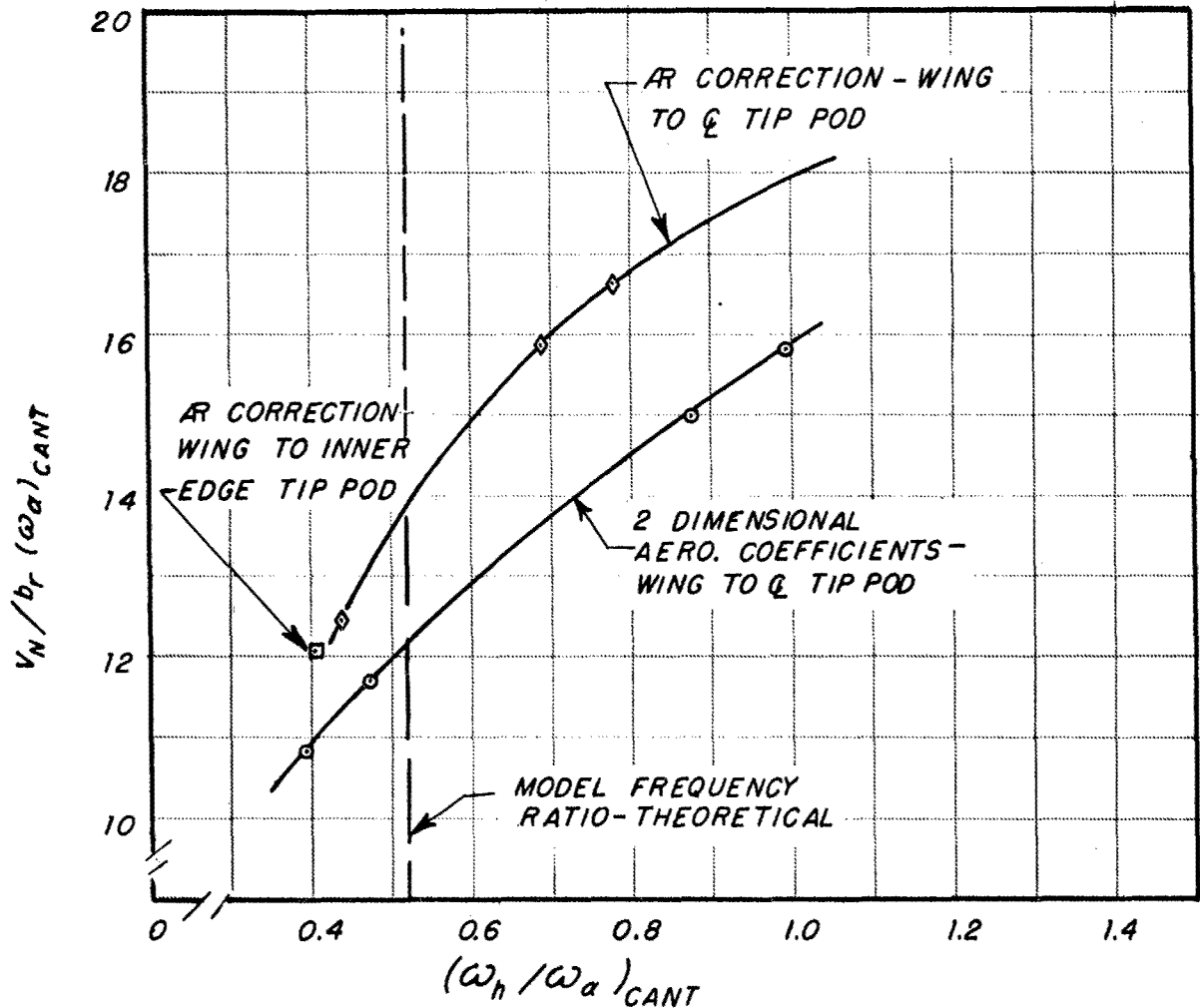
ANALYSIS FOR ROLL-FIRST UNCOUPLED CANTILEVER
BENDING-FIRST UNCOUPLED CANTILEVER TORSION

Fig. 50 $V_N/b_r(\omega_a)_{CANT}$ vs $(\omega_h/\omega_a)_{CANT}$

CASE 3 ANTISYMMETRIC

UNCLASSIFIED

CONFIDENTIAL

TYPE OF ANALYSIS	$(\omega_h/\omega_a)_{CANT}$ (THEOR.)	$V_N/b_r(\omega_a)_{CANT}$ AT FLUTTER		$V_N/b_r\omega$ AT FLUTTER		FLUTTER SPEED-mph		FLUTTER FREQ-cps.	
		CALC.	EXP.	CALC.	EXP.	CALC.	EXP.	CALC.	EXP.
2 DIM.	0.67	28.8	21	36.8	26	238	174	1.63	1.7
Æ WING TO INNER EDGE	0.67	24.3	21	36.2	26	201	174	1.40	1.7
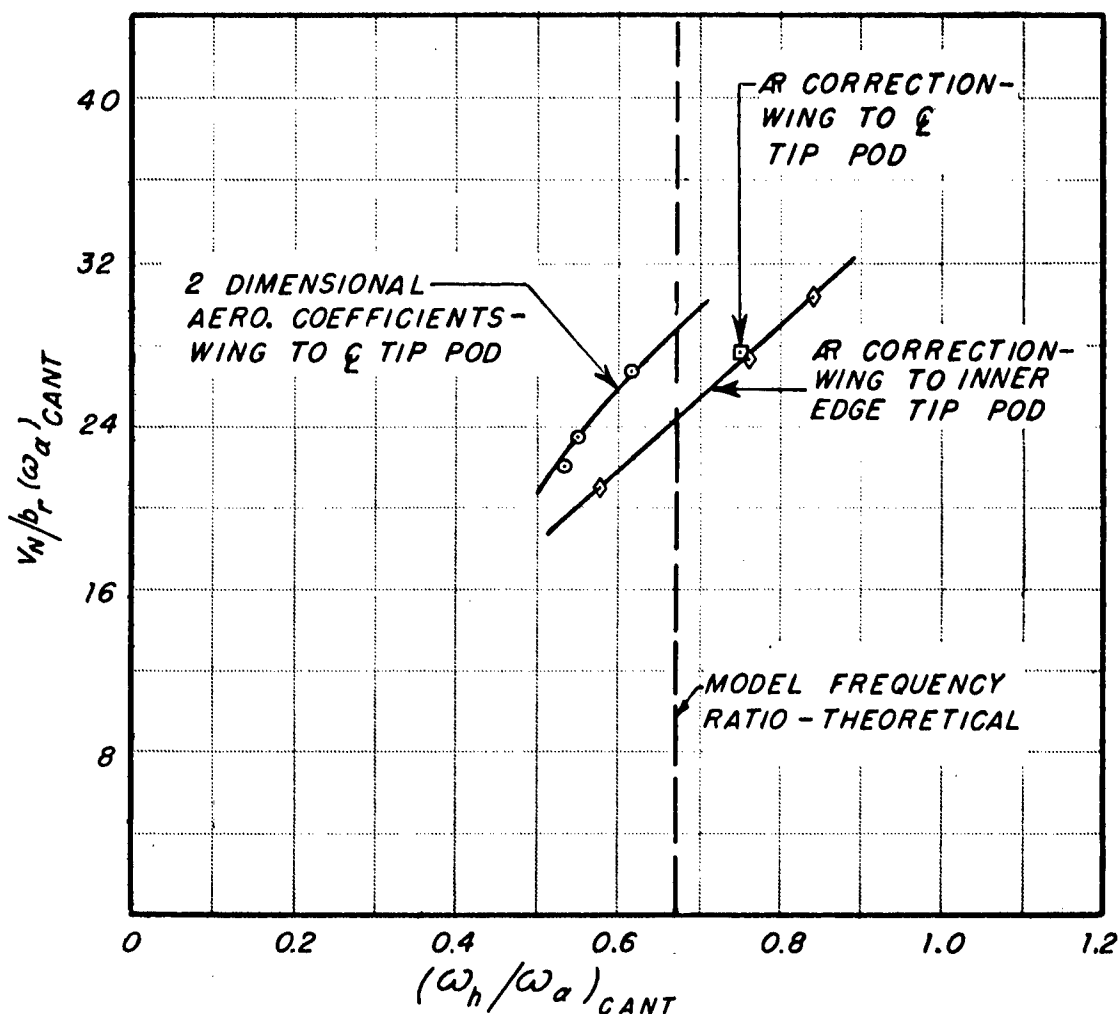
ANALYSIS FOR ROLL — FIRST UNCOUPLED CANTILEVER BENDING — FIRST UNCOUPLED CANTILEVER TORSION

Fig. 51 $V_N/b_r(\omega_a)_{CANT}$ VS $(\omega_h/\omega_a)_{CANT}$

CASE 4 ANTISYMMETRIC

CONFIDENTIAL

TABLE 9

SUMMARY OF FLUTTER PARAMETERS – CALCULATED AND EXPERIMENTAL

| Configu-ration	Type of Analysis	Flutter Speed mph		Flutter Frequency cps		$V_N/b_r\omega$		$V_N/b_r(\omega_\alpha)$cant		(ω_h/ω_α)cant
		Calc.	Exp.	Calc.	Exp.	Calc.	Exp.	Calc.	Exp.	Calc.
3 cant.	2 Dim.	115	124	2.03	2.3	14.3	14	10.7	11.5	0.517
	$\mathcal{R}$ – $\mathbb{E}$	127	124	1.93	2.3	16.6	14	11.8	11.5	0.517
4 cant.	2 Dim.	93	89	1.81	1.9	13.0	12	11.3	10.8	0.671
	$\mathcal{R}$ – $\mathbb{E}$	106	89	1.82	1.9	14.6	12	12.8	10.8	0.671
3 sym.	2 Dim.	148	150	2.38	2.4	15.6	16	13.7	13.9	0.517
	$\mathcal{R}$ – $\mathbb{E}$	174	150	2.20	2.4	19.8	16	16.1	13.9	0.517
4 sym.	2 Dim.	144	138	1.74	1.9	20.8	18	17.4	16.7	0.671
	$\mathcal{R}$ – $\mathbb{E}$	162	138	1.84	1.9	22.2	18	19.7	16.7	0.671
3 anti.	2 Dim.	132	124	1.77	1.8	18.7	17	12.2	11.5	0.517
	$\mathcal{R}$ – $\mathbb{E}$	150	124	1.54	1.8	24.5	17	13.9	11.5	0.517
4 anti.	2 Dim.	238	174	1.63	1.7	36.8	26	28.8	21.1	0.671
	$\mathcal{R}$ – Inner	201	174	1.40	1.7	36.2	26	24.3	21.1	0.671

NOTE: In the above table, under "Type of Analysis", "$\mathcal{R}$ – $\mathbb{E}$" refers to the assumption that the wing extends to the intersection of the elastic axis with the tip pod centerline. "$\mathcal{R}$ – Inner" refers to the assumption that the wing extends to the intersection of the elastic axis with the inner edge of tip pod (See Fig. 45, p. 55).

CONFIDENTIAL   UNCLASSIFIED

Thus in Part 2 the two dimensional and finite span analyses were made to differ only in the values of F + jG used in the aerodynamic coefficients in order that comparison of the relative validity of the two methods of analysis might be made on an equitable basis.

VI. DISCUSSION AND RESULTS

A. Model, Suspension System, and Instrumentation

The wind tunnel model, suspension system, and flutter brake were all completely satisfactory. Accurate flutter data was obtained relatively quickly, and with no damage to the model. As all the above components were similar to items used in Part 1 of this program, this was to be expected.

Instrumentation performance was satisfactory as reflected in a comparison of coupled mode nodal lines obtained visually with those reduced from accelerometer data. It is felt that this is primarily due to the use of the Consolidated accelerometers. Although somewhat heavier than the Martin type which were used for the straight wing tests, the Consolidated accelerometers appear to supply more accurate displacement data at the very low frequencies involved in these tests.

B. Vibration Tests

The coupled mode nodal lines for the cantilever configurations were similar to those encountered with the straight wing. With the addition of rigid body modes, however, this similarity vanished. Whereas the nodal lines for the antisymmetric configurations resemble somewhat those for the straight wing, the associated frequencies are in reverse order. It is of interest to note that even with the wide variation of tip pod and fuselage mass properties encountered in the antisymmetric test cases, none resulted in coupled mode frequencies ordered with the nodal lines as in the straight wing. With the exception of Case 100, the symmetric cases exhibited bending outboard with pitch inboard in one coupled mode, and torsion outboard with translation inboard in the other mode. Case 100 with the smallest tip pod weight and pitch moment of inertia of any of the symmetric cases, resulted in coupled mode nodal lines more nearly like those found in the symmetric cases for the straight wing.

The differences in the dynamic behavior between the straight and swept wings with tip pods are obviously attributable to the more involved interaction, as a result of sweep, between the rigid body modes themselves and between the rigid body modes and the elastic modes. This, and the presence of large rotary inertia mass couplings, makes it considerably more difficult to foresee the effects of varying tip pod mass properties for the case of swept wings.

C. Flutter Tests

Flutter test results are summarized in Tables 6 to 8, pp. 50 and 51. The various tip pod configurations were chosen primarily to afford a wide variation of the parameters η_E and η_T. In addition, some tests were made in which fuselage inertial parameters were varied.

Except for Cases 12, 33A, and 100, the symmetric configurations fluttered violently with considerable coupling between the first torsion and rigid body modes, and with flutter frequencies at or below the first coupled mode frequencies. Cases 12 and 100, which had the lowest tip pod weights and pitch moments of inertia, exhibited primarily bending-torsion coupling during flutter. From visual observation during the tests of Case 33A, all four degrees of freedom were present, and of importance in the flutter mode.

The antisymmetric configurations generally showed a gradual build up of amplitude as the flutter speed was reached, only two cases exhibiting violent, highly divergent flutter. These were Cases 4 antisymmetric and 31 antisymmetric, both of which fluttered at relatively high speeds. All antisymmetric configurations except 31 appeared to flutter with primarily torsion-roll coupling, with flutter frequencies at or below the first coupled mode frequency. Case 31, with the lowest tip pod weight and pitch moment of inertia, fluttered in a primarily bending-torsion mode with the flutter frequency between the two coupled mode frequencies, and in these respects was the only case comparable to the straight wing antisymmetric configurations.

It was observed during the flutter tests of cases involving rigid body degrees of freedom that the effect of the rigid body modes on the elastic modes changed significantly with airspeed, as evidenced by the shift in nodal line locations during model excitations.

Two of the five cantilever configurations exhibited violent flutter. In particular, for case 13 cantilever, the transition from stable motion to violent highly divergent flutter occurred within a 2 mph increase in tunnel speed.

For those configurations tested with both symmetric and cantilever root conditions, the symmetric cases fluttered at higher $V_N/b_r (\omega_\alpha)_{cant}$. Furthermore, it is to be noted that for these configurations, the percentage increase in $V_N/b_r (\omega_\alpha)_{cant}$ in going from cantilever to symmetric root conditions became larger with increasing tip pod weight and pitch moment of inertia. Cases 33B symmetric and 33C symmetric, identical to 33A symmetric except with, respectively, rigid body pitch and rigid body translation locked out, show that the individual rigid body degrees of freedom produce wide variations in the flutter mode and in $V_N/b_r\omega$ at flutter, although the maximum change in flutter speed of these two cases from Case 33A symmetric was only of the order of 10%.

Figures 52 and 53, showing plots of $V_N/b_r (\omega_\alpha)_{cant}$ vs. the "effective c.g. location", η_E, appear to indicate stability boundaries for the test cases. These boundaries represent the lower limits of $V_N/b_r (\omega_\alpha)_{cant}$ at which flutter
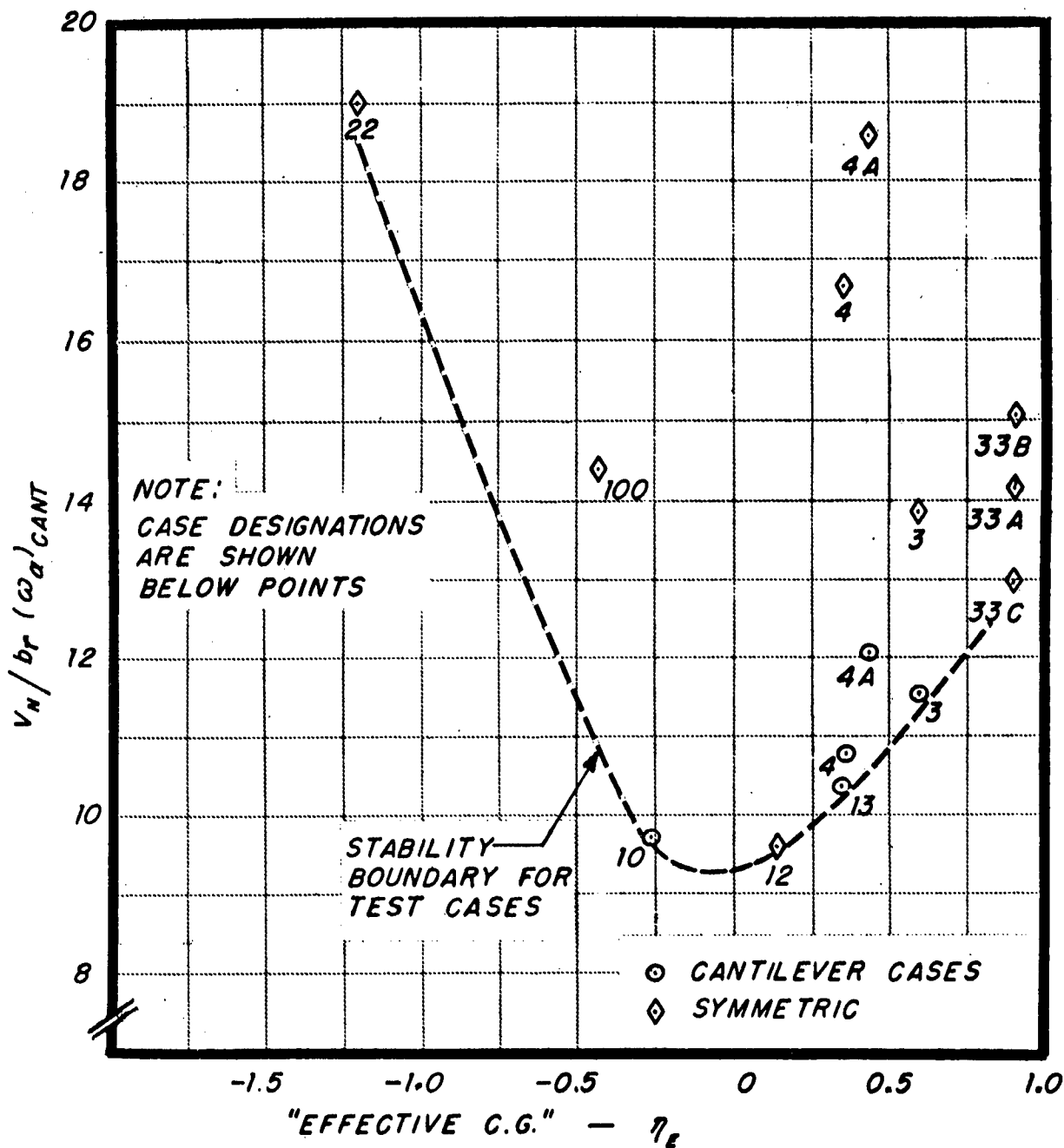
NOTE:
CASE DESIGNATIONS
ARE SHOWN
BELOW POINTS

STABILITY
BOUNDARY FOR
TEST CASES

⊙ CANTILEVER CASES
◇ SYMMETRIC

"EFFECTIVE C.G." — η_E

Fig.52 $V_N/b_r \, (\omega_a)_{CANT}$ VS η_E — SYMMETRIC

AND CANTILEVER CASES

NOTE:
CASE DESIGNATIONS
ARE SHOWN NEAR
EACH TEST POINT

STABILITY BOUNDARY
FOR TEST CASES

NOTE: THE SYMBOL $\top$ DENOTES
NO FLUTTER TO THIS
POINT

"EFFECTIVE C.G." - η_E
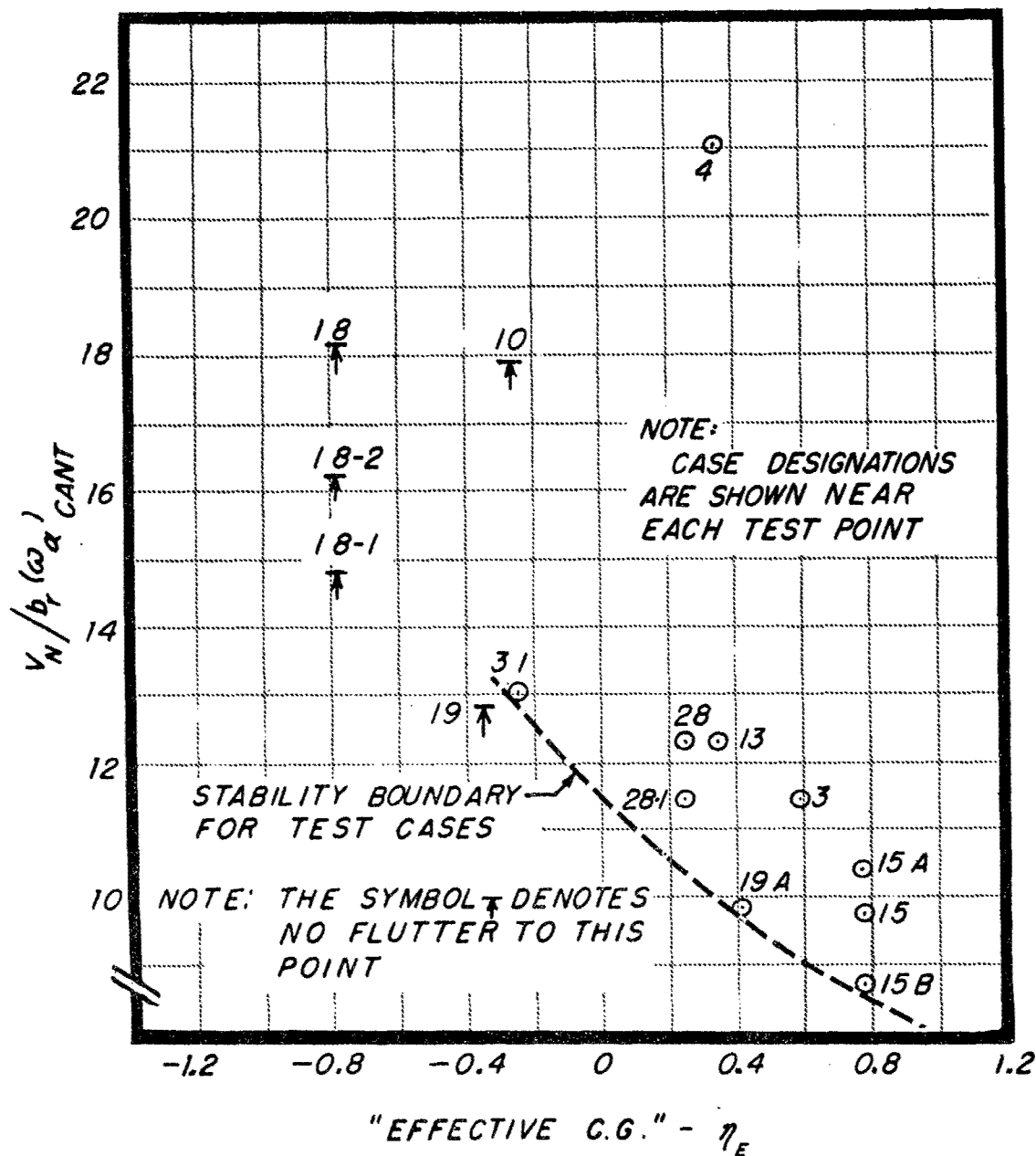
Fig. 53 $V_N/b_r(\omega_\alpha)_{CANT}$ vs η_E

ANTISYMMETRIC CASES

was obtained over the range of η_E tested. For the symmetric and cantilever cases a critical flutter region exists at values of η_E close to zero, in that the stability boundary of Fig. 52 is at a minimum. As the most stable antisymmetric configurations were those with forward effective c.g. locations, it appears that configurations with appreciably negative η_E will be more stable in both symmetric and antisymmetric modes. Such negative effective c.g. configurations can only be obtained with tip pods sufficiently nose heavy to decisively override the rotary inertia coupling. It should be observed that there is a maximum distance along the tip pod forward of the elastic axis at which the actual tip pod c.g. can be placed to achieve this purpose. Forward of this point, the increase in the rotary inertia coupling will more than offset the additional mass static unbalance coupling. However, for normal configurations, this distance is sufficiently large so that the achievement of effectively nose heavy configurations presents no difficulty. For the symmetric and cantilever cases, the data appear to follow the conclusions of Biot and Arnold in Ref. 6 relative to the association of minimum flutter speeds with the proximity of a normal mode nodal line to the 75% chord position.

In general, flutter was not obtained for antisymmetric cases with forward effective c.g. locations. Large variations in fuselage roll inertia did not appear to affect this result, as demonstrated by Cases 18-1 and 18-2, which were identical to Case 18 except for decreased and increased fuselage roll inertia respectively. For Cases 15, 15A, and 15B, and Cases 28 and 28-1, all with aft effective c.g. locations, increasing fuselage roll inertia resulted in increased flutter speeds.

For configurations of the type tested, the stability boundaries of Figs. 52 and 53 indicate that for those configurations with negative or slightly positive η_E the lowest critical flutter speed will be in the symmetric mode, and for those configurations with appreciably positive η_E, the lowest critical flutter speed will be in the antisymmetric mode.

In contrast to the straight wing, it was found that for the antisymmetric cases tested, flutter was not obtained when the first and second coupled mode nodal lines intersected forward of the quarter chord. In those cases where the point of intersection fell on or aft of the quarter chord, flutter was obtained. Furthermore, the flutter speed was lower the further aft the point of intersection, as is shown in Fig. 54. This suggests that for antisymmetric root conditions, the actual tip pod c.g. location is a more important flutter parameter than the effective c.g. location, as it can be shown (see Appendix II) that, for wings with heavy tip pods, the location of the coupled mode nodal line intersection point is simply related to the actual tip pod c.g. location. Thus the similarity in trends shown by the curves of Fig. 54 is to be expected. This dependence of stability on the location of the actual tip pod c.g. and the importance of the quarter chord as a reference point, is analogous to results obtained from analyses of straight wing configurations based on rigid body translation vs. rigid body pitch vs. one fundamental symmetric elastic mode. Thus it is of interest to note that the flutter loops derived from the analyses of the antisymmetric configurations (Figs. 50 and 51, pp. 61 and 62) resemble those obtained from analyses for such symmetric configurations of straight wings.
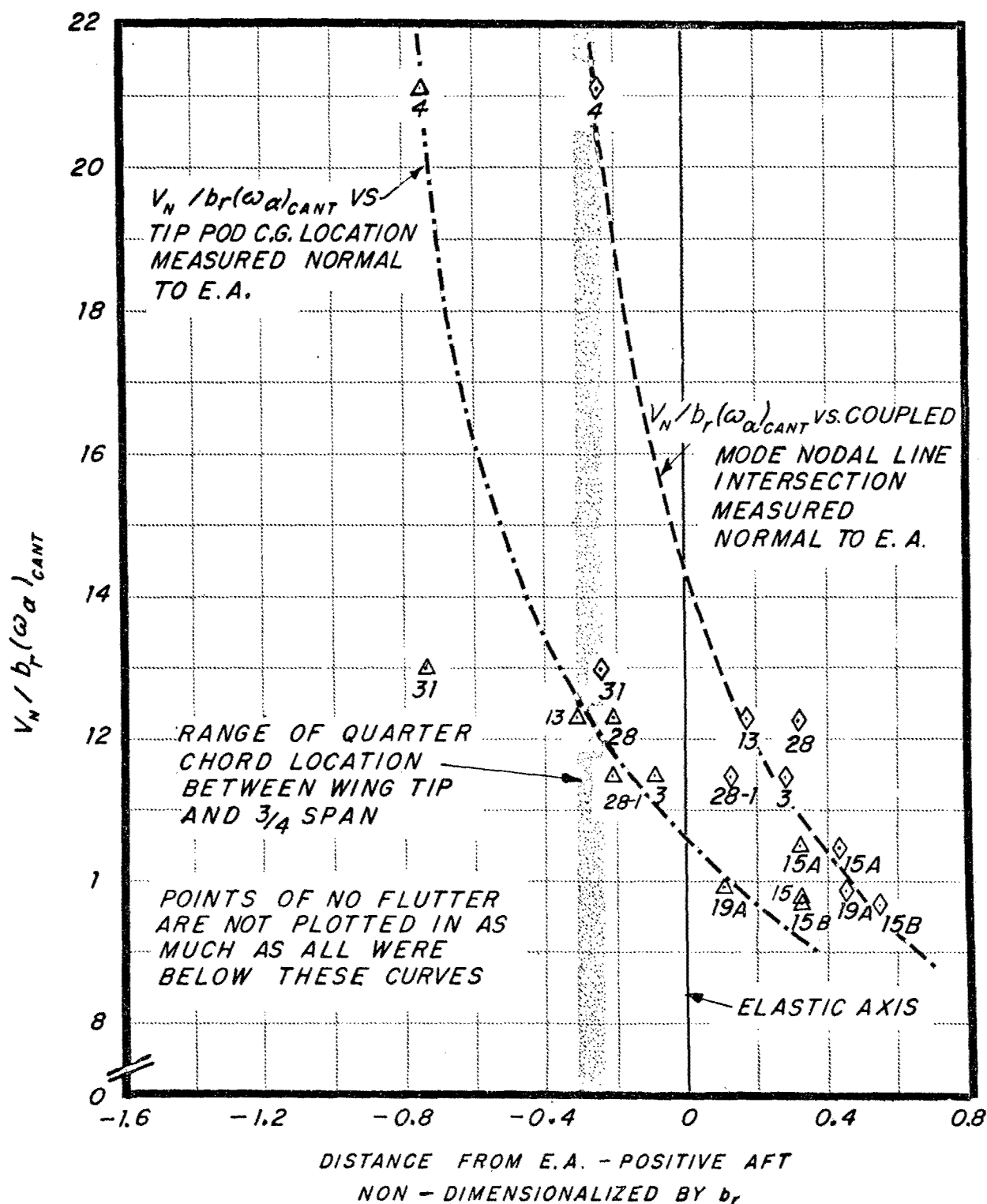
Fig. 54 $V_N/b_r(\omega_\alpha)_{CANT.}$ VS TIP POD C.G. LOCATION
AND VS COUPLED MODE NODAL LINE INTERSECTION
ANTISYMMETRIC CASES

D. **Flutter Analyses**

For the most part, the flutter analyses confirmed the trends of the experimental results. Referring to Table 9, p. 63, it can be seen that, with the exception of Case 4 antisymmetric, the analyses based on two dimensional aerodynamics resulted in good correlation with the experimental data; the analyses based on finite wing aerodynamics, except for Case 3 cantilever, yielded appreciably unconservative flutter speeds.

Sources of errors in the analyses, other than those inherent in the non-stationary aerodynamics of swept wings and the assumptions on which the tip pod aerodynamics were based, are: inaccuracies in the mass and stiffness data, the assumption of Case 3 cantilever mode shapes for Case 4 analyses, and the manner in which the reflection plane at the wing root was assumed for the finite wing analyses. In view of the steepness of the curves of Fig. 54, it appears that small errors in the tip pod mass data and the wing stiffness data as reflected in nodal line location, can have considerable effect on the results of the anti-symmetric mode flutter analyses. It is felt that the use of the Case 3 cantilever mode shapes in Case 4 analyses resulted in relatively small errors in the computed results. The orientation assumed for the reflection plane at the wing root may have introduced significant errors in the analyses based on finite wing aerodynamics. It would be of interest to compare the data with the results of flutter analyses incorporating finite wing aerodynamics based on a reflection plane parallel to the free stream direction. Because of the high $V_N/b_r\omega$ at flutter, particularly for Case 4 antisymmetric, pseudo-static aerodynamic coefficients would probably approximate the actual oscillatory aerodynamics in a more satisfactory manner. These pseudo-static coefficients could be computed by standard methods incorporating the proper orientation of the reflection plane. The better representation of the aerodynamics at high $V_N/b_r\omega$'s given by such coefficients should result in more accurate flutter analyses.

An interesting feature of the analyses of the symmetric cases is that at frequency ratios larger than approximately 0.6, $V_N/b_r(\omega_\alpha)_{cant}$ is essentially constant and independent of cantilever frequency ratio. The analyses for these cases show that, at the values of $V_N/b_r\omega$ for which this condition occurs, the effect of the rigid body modes on the elastic modes is to weaken the effective coupling between the elastic modes to such an extent that for $(\omega_h/\omega_\alpha)_{cant}$ greater than approximately 0.6, the solutions are unaffected by the first cantilever bending mode. The analyses indicate, therefore, that for these frequency ratios, the flutter mode would essentially consist of the first uncoupled cantilever torsion vs. rigid body translation vs. rigid body pitch modes. The value of $(\omega_h/\omega_\alpha)_{cant}$ for Case 4 was 0.67, and visual observations during the flutter tests confirmed that the flutter mode was predominantly of this nature. However, it is not clear from these two analyses whether this condition would be obtained for other swept-wing-with-tip-pod configurations. It should be noted that in the analyses, the approach of $V_N/b_r(\omega_\alpha)_{cant}$ to a constant value coincides with an approach to an apparent damped resonance in the rigid body pitch degree of freedom assumed for the analysis. For wings with normal sweep angles, this apparent resonance will always occur at some value of $V_N/b_r\omega$.

Even though the translation and pitch springs, incorporated in the model suspension system to center the model in the tunnel, were purposely kept soft, the symmetric cases analyzed showed some sensitivity to rigid body pitch frequency, although damping in the pitch mode of the order of magnitude encountered in the tests had relatively small effect. The rigid body translation frequency and damping had negligible effects, as the frequency was only 0.4 that of the rigid body pitch frequency.

In the process of performing the flutter analyses, an arithmetic error was made and subsequently corrected in the tip pod aerodynamic coefficients affecting several terms in the flutter determinant. The maximum change in any aerodynamic term in the flutter determinant was of the order of 10% (in A_{12}), yet significant changes in the shapes of the flutter loops of the symmetric cases resulted, particularly for the Case 3 symmetric finite wing analysis, in which a loop similar to those resulting from the cantilever analyses all but disappeared in the corrected results. Investigation of the reason for these results indicates that the predominant effect is the small decrease in the bending-torsion coupling term which markedly aggravates the decoupling effect of the rigid body modes. This suggests that the flutter characteristics of the symmetric configurations are sensitive to relatively small changes in the bending-torsion coupling term and indicates the importance of incorporating accurate tip pod aerodynamics and accurate values of tip bending slope in the analyses. It should be noted that this is particularly true for those nose-heavy tip pod configurations with rotary inertia and mass unbalance couplings of comparable orders of magnitude, i.e., m_{12} near zero.

The $V_N/b_r(\omega_\alpha)_{cant}$ vs. $(\omega_h/\omega_\alpha)_{cant}$ curves for the antisymmetric cases, shown in Figs. 50 and 51, pp. 61 and 62, bear no resemblance to the usual type of flutter loop. However, as previously noted, there is some similarity to low frequency dynamic instability curves. Although the computed flutter speeds for these cases are unconservative, they are consistent with the vibration analyses in that, even though good agreement of computed with experimental coupled mode nodal lines was obtained, the computed nodal line intersection points for both Cases 3 and 4 antisymmetric were slightly forward of the experimental points of intersection (see Figs. 28 and 29, p. 34 and 35). On the basis of Fig. 54, p. 69, it is therefore to be expected that the analyses would predict greater stability than these configurations exhibited during the flutter tests. It is difficult to say, without additional analysis, whether the poor correlation with test data obtained from the analysis of Case 4 antisymmetric using two dimensional aerodynamic coefficients is primarily due to the above effect, or to inaccurate aerodynamic data as noted previously.

The effect of the roll spring was destabilizing in the analyses of the antisymmetric cases, in that increased roll frequency reduced the flutter speed although damping in roll of the order of magnitude present during the tests had negligible effect.

VII. CONCLUSIONS AND RECOMMENDATIONS

It may be generally concluded that the objectives of this program were achieved. Considerable flutter data covering a wide range of tip pod mass properties was obtained, and theoretical comparisons with the experimental data were made. From these data and the theoretical analyses, it may be further concluded that:

1. As in the case of straight wings with large tip pods, fuselage and tip pod mass parameters dominate wing mass parameters.

2. For the symmetric and cantilever configurations tested, those with η_E near zero resulted in the lowest values of $V_N/b_r(\omega_\alpha)_{cant}$. The antisymmetric cases, in general, showed decreasing stability with increasingly positive values of η_E.

3. Configurations with appreciably negative values of η_E, obtainable by the use of tip pods sufficiently nose-heavy to decisively override the rotary inertia coupling, were more stable for both symmetric and antisymmetric root conditions than configurations with correspondingly positive values.

4. The actual tip pod c.g. location, as reflected in the intersection point of the first two coupled mode nodal lines, is a fundamental parameter in the antisymmetric flutter mode of swept wings with heavy tip pods. Test configurations were stable for intersection points forward of the wing quarter chord, and were increasingly unstable for intersection points aft of the quarter chord.

5. The sensitivity of the vibration and flutter analyses of nose-heavy configurations to tip bending slope suggests that it might be possible to reduce the large rotary inertia effects in the bending-torsion mass coupling by small adjustments of the flexural rigidity distribution.

6. Computed results from analyses based on strip theory aerodynamics, with one exception, gave good agreement with experimental results, whereas analyses based on finite wing aerodynamics in general yielded appreciably unconservative flutter speeds.

7. Tip pod aerodynamics are important in the flutter analyses of configurations of the type tested. Errors of the order of magnitude of the tip pod aerodynamics may produce large differences in computed flutter characteristics.

8. The important dynamic differences between the swept wing results and the straight wing results of Part 1 of this report are: the influence of the tip pod rotary inertia coupling effects on the vibration and flutter characteristics of the swept wing; the dissimilarities between the straight and swept wing symmetric and antisymmetric coupled modes; the occurrence of flutter in the cantilever and in the symmetric modes for swept wing configurations with negative as well as positive η_E; and, in general, the non-occurrence of antisymmetric mode flutter for swept wing configurations with negative η_E.

It is recommended that:

1. Further investigations be made of the oscillatory aerodynamics of swept-wing-tip-pod configurations, for use in flutter analyses.

2. Data be obtained for the flutter of swept wings with large tip pods in the compressible flow region.

3. Flutter tests, similar to the present program, be made on swept wings with heavy tip pods to further investigate the stability in the symmetric mode with respect to the effective c.g. location. It is believed that the maximum information would result if such tests were made on groups of configurations, each with constant cantilever frequency ratio and fixed tip pod pitch moment of inertia.

4. Further analytical flutter investigations be made using the experimental data of this report and incorporating finite wing pseudo-static aerodynamic coefficients.

VIII. REFERENCES

1. Nelson, H. C., and Tomassoni, J. E. Experimental Investigation of the Effects of Sweepback on the Flutter of a Uniform Cantilever Wing with a Variably Located Concentrated Mass NACA RM L9F24 August 31, 1949.

2. Tomassoni, J. E., and Nelson, H. C. Experimental Investigation of the Effects of Root Restraint on the Flutter of a Sweptback, Uniform, Cantilever Wing with a Variably Located Concentrated Mass NACA RM L9J21a, March 31, 1950.

3. Sewall, J. L. Experimental and Analytical Investigation of Flutter of a Nonuniform Sweptback Cantilever Wing with Two Concentrated Weights NACA RM L51H09a December 4, 1951.

4. Spielberg, I., Fettis, H. E., and Toney, H. S. Methods for Calculating the Flutter and Vibration Characteristics of Swept Wings Engineering Division Memorandum Report MCREXA5-4595-8-4 August 3, 1948.

5. Smilg, B., and Wasserman, L. S. Application of Three Dimensional Flutter Theory to Aircraft Structures Air Corps Technical Report No. 4798 July 9, 1942.

6. Biot, M. A. and Arnold, Lee Low-Speed Flutter and Its Physical Interpretation Journal of the Aeronautical Sciences Vol. 15, pp. 232-236 April, 1948.

7. Broadbent, E. G. Flutter Problems of High Speed Aircraft R.A.E. Report No. Structures 37 April, 1949.

APPENDIX I

DETAILS OF ANALYSES

A. Flutter Analysis For Symmetric Cases

The dynamic equations of motion for first cantilever wing bending vs first cantilever wing torsion vs airplane rigid body translation vs airplane rigid body pitch flutter are

$$\begin{bmatrix} E_{11} & E_{12} & E_{13} & E_{14} \\ E_{21} & E_{22} & E_{23} & E_{24} \\ E_{31} & E_{32} & E_{33} & E_{34} \\ E_{41} & E_{42} & E_{43} & E_{44} \end{bmatrix} \begin{bmatrix} H_T^{(1)}/b_r \\ H_T^{(\alpha)} \\ H_T^{(0)}/b_r \\ H_T^{(p)}/b_r \end{bmatrix} = 0$$

where

$$E_{11} = m_{11}\left[1 - \left(\frac{\omega_h}{\omega}\right)^2\left(1 + jg_h\right)\right] + A_{11}$$

$$E_{12} = m_{12} + A_{12}$$

$$E_{13} = m_{13} + A_{13}$$

$$E_{14} = m_{14} + A_{14}$$

$$E_{21} = m_{21} + A_{21}$$

$$E_{22} = m_{22}\left[1 - \left(\frac{\omega_\alpha}{\omega}\right)^2\left(1 + jg_\alpha\right)\right] + A_{22}$$

$$E_{23} = m_{23} + A_{23}$$

$$E_{24} = m_{24} + A_{24}$$

$$E_{31} = m_{31} + A_{31}$$

$$E_{32} = m_{32} + A_{32}$$

$$E_{33} = m_{33}\left[1 - \left(\frac{\omega_{h_0}}{\omega}\right)^2\left(1 + jg_{h_0}\right)\right] + A_{33}$$

$$E_{34} = m_{34} + A_{34}$$

$$E_{41} = m_{41} + A_{41}$$

$$E_{42} = m_{42} + A_{42}$$

$$E_{43} = m_{43} + A_{43}$$

$$E_{44} = m_{44}\left[1 - \left(\frac{\omega_p}{\omega}\right)^2\left(1 + jg_{h_p}\right)\right] + A_{44}$$

$$A_{ij} = (A_{ij})_N + (A_{ij})_S + (A_{ij})_T \quad , \quad i,j = 1, 2, 3, 4.$$

$(A_{ij})_N$, $(A_{ij})_S$, and $(A_{ij})_T$ are the non-dimensionalized aerodynamic terms due to the velocity component normal to the elastic axis, the velocity component parallel to the elastic axis, and the tip pod respectively. These are defined on pp. 80 to 83.

m_{ij} are the non-dimensionalized effective mass terms of the wing, fuselage, tip pod combination and are defined on pp. 78 and 79.

The generalized coordinates $H_r^{(1)}/b_r$, $H_r^{(\alpha)}$, $H_r^{(a)}/b_r$, and $H_r^{(p)}/b_r$ represent the non-dimensional tip amplitudes in first cantilever bending, first cantilever torsion, rigid body translation, and rigid body pitch to which the mode shapes have been normalized.

B. Flutter Analysis For Cantilever Cases

The dynamic equations of motion for first cantilever wing bending vs first cantilever wing torsion flutter are

$$\begin{bmatrix} E_{11} & E_{12} \\ E_{21} & E_{22} \end{bmatrix} \begin{bmatrix} H_T^{(1)}/b_r \\ H_T^{(\alpha)} \end{bmatrix} = 0$$

where E_{ij}, $i,j = 1, 2$, are defined as on p. 75.

C. Flutter Analysis For Anti-Symmetric Cases

The dynamic equations of motion for first cantilever wing bending vs first cantilever wing torsion vs airplane rigid body roll flutter are

$$\begin{bmatrix} E_{55} & E_{56} & E_{57} \\ E_{65} & E_{66} & E_{67} \\ E_{75} & E_{76} & E_{77} \end{bmatrix} \begin{bmatrix} H_T^{(1)}/b_r \\ H_T^{(\alpha)} \\ H_T^{(r)}/b_r \end{bmatrix} = 0$$

where

$$E_{55} = m_{55}\left[1 - \left(\frac{\omega_h}{\omega}\right)^2 (1 + jg_h) \right] + A_{55}$$

$$E_{56} = m_{56} + A_{56}$$

$$E_{57} = m_{57} + A_{57}$$

$$E_{65} = m_{65} + A_{65}$$

$$E_{66} = m_{66}\left[1 - \left(\frac{\omega_\alpha}{\omega}\right)^2 (1 + jg_\alpha) \right] + A_{66}$$

$$E_{67} = m_{67} + A_{67}$$

$$E_{75} = m_{75} + A_{75}$$

$$E_{76} = m_{76} + A_{76}$$

$$E_{77} = m_{77}\left[1 - \left(\frac{\omega_r}{\omega}\right)^2 (1 + j q_r)\right] + A_{77}$$

and

$$A_{ij} = (A_{ij})_N + (A_{ij})_S + (A_{ij})_T , \quad i,j = 5,6,7$$

$(A_{ij})_N$, $(A_{ij})_S$, and $(A_{ij})_T$ are defined on pp. 84 and 85.

m_{ij} are defined on p. 79.

$H_r^{(r)}/b_r$ is the non-dimensional tip amplitude in rigid body roll.

D. <u>Definitions of Mechanical Terms</u>

For coordinate system used, see Fig. 45, p. 55.

$$m_{11} = \frac{1}{\pi \rho b_r^2 \ell}\left\{W_T - 2S_T\left[\frac{\varphi_T^{(1)}}{H_T^{(1)}}\right]\sin\Lambda + I_T\left[\frac{\varphi_T^{(1)}}{H_T^{(1)}}\right]^2 \sin^2\Lambda + \int_0^\ell W\left[h^{(1)}\right]^2 dx\right\}$$

$$m_{21} = m_{12} = \frac{1}{\pi \rho b_r^3 \ell}\left\{S_T \cos\Lambda - I_T\left[\frac{\varphi_T^{(1)}}{H_T^{(1)}}\right]\sin\Lambda \cos\Lambda + \int_0^\ell S_\alpha\left[h^{(1)}\alpha^{(1)}\right]dx\right\}$$

$$m_{31} = m_{13} = \frac{1}{\pi \rho b_r^2 \ell}\left\{W_T - S_T\left[\frac{\varphi_T^{(1)}}{H_T^{(1)}}\right]\sin\Lambda + \int_0^\ell W\left[h^{(1)}\right]dx\right\}$$

$$m_{41} = m_{14} = \frac{1}{\pi \rho b_r^2 \ell}\left\{W_T + \frac{S_T}{\ell \sin\Lambda} - S_T\left[\frac{\varphi_T^{(1)}}{H_T^{(1)}}\right]\sin\Lambda - \frac{I_T}{\ell}\left[\frac{\varphi_T^{(1)}}{H_T^{(1)}}\right] + \int_0^\ell\left[W\left(\frac{x}{\ell}\right) + \frac{\cot\Lambda}{\ell}S_\alpha\right]\left[h^{(1)}\right]dx\right\}$$

$$m_{22} = \frac{1}{\pi \rho b_r^4 \ell}\left\{I_T \cos^2\Lambda + \int_0^\ell I_\alpha\left[\alpha^{(1)}\right]^2 dx\right\}$$

$$m_{32} = m_{23} = \frac{1}{\pi \rho b_r^3 \ell}\left\{S_T \cos\Lambda + \int_0^\ell S_\alpha\left[\alpha^{(1)}\right]dx\right\}$$

$$m_{42} = m_{24} = \frac{1}{\pi \rho b_r^3 \ell} \left\{ S_T \cos \Lambda + \frac{I_T}{\ell} \cot \Lambda + \int_0^\ell \left[S_\alpha \left(\frac{x}{\ell} \right) + \frac{\cot \Lambda}{\ell} I_\alpha \right] \left[\alpha^{(1)} \right] dx \right\}$$

$$m_{33} = \frac{1}{\pi \rho b_r^2 \ell} \left\{ W_T + W_F + \int_0^\ell W \, dx \right\}$$

$$m_{43} = m_{34} = \frac{1}{\pi \rho b_r^2 \ell} \left\{ W_T + \frac{S_T + S_F}{\ell \sin \Lambda} + \int_0^\ell \left[W \left(\frac{x}{\ell} \right) + \frac{\cot \Lambda}{\ell} S_\alpha \right] dx \right\}$$

$$m_{44} = \frac{1}{\pi \rho b_r^2 \ell} \left\{ W_T + \frac{2 S_T}{\ell \sin \Lambda} + \frac{I_T + I_F}{(\ell \sin \Lambda)^2} + \int_0^\ell \left[W \left(\frac{x}{\ell} \right)^2 + \frac{2 \cot \Lambda}{\ell} S_\alpha \left(\frac{x}{\ell} \right) + \frac{\cot^2 \Lambda}{\ell^2} I_\alpha \right] dx \right\}$$

$$m_{55} = m_{11}$$

$$m_{56} = m_{65} = m_{12}$$

$$m_{57} = m_{75} = \frac{1}{\pi \rho b_r^2 \ell} \left\{ W_T - S_T \left[\frac{\varphi_T^{(1)}}{H_T^{(1)}} \right] \sin \Lambda + \int_0^\ell \left[W \left(\frac{x}{\ell} \right) - \frac{\tan \Lambda}{\ell} S_\alpha \right] \left[h^{(1)} \right] dx \right\}$$

$$m_{66} = m_{22}$$

$$m_{67} = m_{76} = \frac{1}{\pi \rho b_r^3 \ell} \left\{ S_T \cos \Lambda + \int_0^\ell \left[S_\alpha \left(\frac{x}{\ell} \right) - \frac{\tan \Lambda}{\ell} I_\alpha \right] \left[\alpha^{(1)} \right] dx \right\}$$

$$m_{77} = \frac{1}{\pi \rho b_r^2 \ell} \left\{ W_T + \frac{I_\phi}{(\ell \cos \Lambda)^2} + \int_0^\ell \left[W \left(\frac{x}{\ell} \right)^2 - \frac{2 \tan \Lambda}{\ell} S_\alpha \left(\frac{x}{\ell} \right) + \frac{\tan^2 \Lambda}{\ell^2} I_\alpha \right] dx \right\}$$

E. Definitions of Aerodynamic Terms

For coordinate system used, see Fig. 45, p. 55.

$$(A_{11})_N = \frac{1}{\ell} \int_0^{\ell} \left[\frac{b}{b_r}\right]^2 \left[h^{(1)}\right]^2 \left[L_h\right] dx$$

$$(A_{12})_N = \frac{1}{\ell} \int_0^{\ell} \left[\frac{b}{b_r}\right]^3 \left[h^{(1)} \alpha^{(1)}\right] \left[L_\alpha - \left(\frac{1}{2}+a\right)L_h\right] dx$$

$$(A_{13})_N = \frac{1}{\ell} \int_0^{\ell} \left[\frac{b}{b_r}\right]^2 \left[h^{(1)}\right] \left[L_h\right] dx$$

$$(A_{14})_N = \frac{1}{\ell} \int_0^{\ell} \left[\frac{b}{b_r}\right]^2 \left[\left(\frac{x}{\ell}\right) h^{(1)}\right] \left[L_h\right] dx +$$
$$+ \cot \Lambda \left(\frac{b_r}{\ell^2}\right) \int_0^{\ell} \left[\frac{b}{b_r}\right]^3 \left[h^{(1)}\right] \left[L_\alpha - \left(\frac{1}{2}+a\right)L_h\right] dx$$

$$(A_{21})_N = \frac{1}{\ell} \int_0^{\ell} \left[\frac{b}{b_r}\right]^3 \left[h^{(1)} \alpha^{(1)}\right] \left[\frac{1}{2} - \left(\frac{1}{2}+a\right)L_h\right] dx$$

$$(A_{22})_N = \frac{1}{\ell} \int_0^{\ell} \left[\frac{b}{b_r}\right]^4 \left[\alpha^{(1)}\right]^2 \left[-\frac{1}{2}\left(\frac{1}{2}+a\right) + M_\alpha - \left(\frac{1}{2}+a\right)L_\alpha + \left(\frac{1}{2}+a\right)^2 L_h\right] dx$$

$$(A_{23})_N = \frac{1}{\ell} \int_0^{\ell} \left[\frac{b}{b_r}\right]^3 \left[\alpha^{(1)}\right] \left[\frac{1}{2} - \left(\frac{1}{2}+a\right)L_h\right] dx$$

$$(A_{24})_N = \frac{1}{\ell} \int_0^{\ell} \left[\frac{b}{b_r}\right]^3 \left[\left(\frac{x}{\ell}\right) \alpha^{(1)}\right] \left[\frac{1}{2} - \left(\frac{1}{2}+a\right)L_h\right] dx$$
$$+ \cot \Lambda \left(\frac{b_r}{\ell^2}\right) \int_0^{\ell} \left[\frac{b}{b_r}\right]^4 \left[\alpha^{(1)}\right] \left[-\frac{1}{2}\left(\frac{1}{2}+a\right) + M_\alpha - \left(\frac{1}{2}+a\right)L_\alpha + \left(\frac{1}{2}+a\right)^2 L_h\right] dx$$

$$(A_{31})_N = \frac{1}{\ell} \int_0^{\ell} \left[\frac{b}{b_r}\right]^2 \left[h^{(1)}\right] \left[L_h\right] dx$$

$$(A_{32})_N = \frac{1}{\ell} \int_0^{\ell} \left[\frac{b}{b_r}\right]^3 \left[\alpha^{(1)}\right] \left[L_\alpha - \left(\frac{1}{2}+a\right)L_h\right] dx$$

$$(A_{33})_N = \frac{1}{\ell} \int_0^{\ell} \left[\frac{b}{b_r}\right]^2 \left[L_h\right] dx$$

$$(A_{34})_N = \frac{1}{2}\int_0^l \left[\frac{b}{b_r}\right]^2\left[\frac{x}{l}\right]\left[L_h\right]dx + \cot\Lambda\left(\frac{b_r}{l^2}\right)\int_0^l\left[\frac{b}{b_r}\right]^3\left[L_\alpha-\left(\frac{1}{2}+a\right)L_h\right]dx$$

$$(A_{41})_N = \frac{1}{2}\int_0^l\left[\frac{b}{b_r}\right]^2\left[\left(\frac{x}{l}\right)h^{(\prime)}\right]\left[L_h\right]dx+\cot\Lambda\left(\frac{b_r}{l^2}\right)\int_0^l\left[\frac{b}{b_r}\right]^3\left[h^{(\prime)}\right]\left[\frac{1}{2}-\left(\frac{1}{2}+a\right)L_h\right]dx$$

$$(A_{42})_N = \frac{1}{2}\int_0^l\left[\frac{b}{b_r}\right]^3\left[\left(\frac{x}{l}\right)\alpha^{(\prime)}\right]\left[L_\alpha-\left(\frac{1}{2}+a\right)L_h\right]dx$$

$$+\cot\Lambda\left(\frac{b_r}{l^2}\right)\int_0^l\left[\frac{b}{b_r}\right]^4\left[\alpha^{(\prime)}\right]\left[-\frac{1}{2}\left(\frac{1}{2}+a\right)+M_\alpha-\left(\frac{1}{2}+a\right)L_\alpha+\left(\frac{1}{2}+a\right)^2 L_h\right]dx$$

$$(A_{43})_N = \frac{1}{2}\int_0^l\left[\frac{b}{b_r}\right]^2\left[\frac{x}{l}\right]\left[L_h\right]dx+\cot\Lambda\left(\frac{b_r}{l^2}\right)\int_0^l\left[\frac{b}{b_r}\right]^3\left[\frac{1}{2}-\left(\frac{1}{2}+a\right)L_h\right]dx$$

$$(A_{44})_N = \frac{1}{2}\int_0^l\left[\frac{b}{b_r}\right]^2\left[\frac{x}{l}\right]^2\left[L_h\right]dx + \cot\Lambda\left(\frac{b_r}{l^2}\right)\int_0^l\left[\frac{b}{b_r}\right]^3\left[\frac{x}{l}\right]\left[L_\alpha-\left(\frac{1}{2}+a\right)L_h\right]dx$$

$$+\cot\Lambda\left(\frac{b_r}{l^2}\right)\int_0^l\left[\frac{b}{b_r}\right]^3\left[\frac{x}{l}\right]\left[\frac{1}{2}-\left(\frac{1}{2}+a\right)L_h\right]dx$$

$$+\cot^2\Lambda\left(\frac{b_r^2}{l^3}\right)\int_0^l\left[\frac{b}{b_r}\right]^4\left[-\frac{1}{2}\left(\frac{1}{2}+a\right)+M_\alpha-\left(\frac{1}{2}+a\right)L_\alpha+\left(\frac{1}{2}+a\right)^2 L_h\right]dx$$

$$(A_{11})_S = j\tan\Lambda\left(\frac{b_r}{l}\right)\left(\frac{V_N}{b_r\omega}\right)\int_0^l\left[\frac{b}{b_r}\right]^2\left[\left(\frac{\varphi^{(\prime)}}{H_T^{(\prime)}}\right)h^{(\prime)}\right]\left[L_h\right]dx$$

$$(A_{12})_S = 0$$

$$(A_{13})_S = 0$$

$$(A_{14})_S = -j\tan\Lambda\left(\frac{b_r}{l^2}\right)\left(\frac{V_N}{b_r\omega}\right)\int_0^l\left[\frac{b}{b_r}\right]^2\left[h^{(\prime)}\right]\left[L_h\right]dx$$

$$(A_{21})_S = j\tan\Lambda\left(\frac{b_r}{l}\right)\left(\frac{V_N}{b_r\omega}\right)\int_0^l\left[\frac{b}{b_r}\right]^3\left[\left(\frac{\varphi^{(\prime)}}{H_T^{(\prime)}}\right)\alpha^{(\prime)}\right]\left[\frac{1}{2}-\left(\frac{1}{2}+a\right)L_h\right]dx$$

$$(A_{22})_S = 0$$

$$(A_{23})_S = 0$$

$$(A_{24})_s = -j \tan \Lambda \left(\frac{b_r}{\ell^2}\right)\left(\frac{V_N}{b_r \omega}\right)\int_0^\ell \left[\frac{b}{b_r}\right]^3 \left[\alpha^{(l)}\right]\left[\tfrac{1}{2} - \left(\tfrac{1}{2} + a\right) L_h\right] dx$$

$$(A_{31})_s = j \tan \Lambda \left(\frac{b_r}{\ell}\right)\left(\frac{V_N}{b_r \omega}\right)\int_0^\ell \left[\frac{b}{b_r}\right]^2 \left[\frac{\varphi^{(l)}}{H_T^{(l)}}\right]\left[L_h\right] dx$$

$$(A_{32})_s = 0$$

$$(A_{33})_s = 0$$

$$(A_{34})_s = -j \tan \Lambda \left(\frac{b_r}{\ell^2}\right)\left(\frac{V_N}{b_r \omega}\right)\int_0^\ell \left[\frac{b}{b_r}\right]^2 \left[L_h\right] dx$$

$$(A_{41})_s = j \tan \Lambda \left(\frac{b_r}{\ell}\right)\left(\frac{V_N}{b_r \omega}\right)\int_0^\ell \left[\frac{b}{b_r}\right]^2 \left[\left(\tfrac{x}{\ell}\right)\left(\frac{\varphi^{(l)}}{H_T^{(l)}}\right)\right]\left[L_h\right] dx$$
$$+ j \left(\frac{b_r}{\ell}\right)^2 \left(\frac{V_N}{b_r \omega}\right)\int_0^\ell \left[\frac{b}{b_r}\right]^3 \left[\frac{\varphi^{(l)}}{H_T^{(l)}}\right]\left[\tfrac{1}{2} - \left(\tfrac{1}{2} + a\right) L_h\right] dx$$

$$(A_{42})_s = 0$$

$$(A_{43})_s = 0$$

$$(A_{44})_s = -j \tan \Lambda \left(\frac{b_r}{\ell^2}\right)\left(\frac{V_N}{b_r \omega}\right)\int_0^\ell \left[\frac{b}{b_r}\right]^2 \left[\frac{x}{\ell}\right]\left[L_h\right] dx$$
$$- j \left(\frac{b_r^2}{\ell^3}\right)\left(\frac{V_N}{b_r \omega}\right)\int_0^\ell \left[\frac{b}{b_r}\right]^3 \left[\tfrac{1}{2} - \left(\tfrac{1}{2} + a\right) L_h\right] dx$$

Refer to p. 86 for L_{α_T} and M_{α_T}

$$(A_{11})_T = - b_r \left(\frac{\varphi_T^{(1)}}{H_T^{(1)}}\right) \sin \Lambda \left[L_{\alpha_T} - M_{\alpha_T} \, b_r \left(\frac{\varphi_T^{(1)}}{H_T^{(1)}}\right) \sin \Lambda \right]$$

$$(A_{12})_T = \cos \Lambda \left[L_{\alpha_T} - M_{\alpha_T} \, b_r \left(\frac{\varphi_T^{(1)}}{H_T^{(1)}}\right) \sin \Lambda \right]$$

$$(A_{13})_T = 0$$

$$(A_{14})_T = \frac{b_r}{\ell \sin \Lambda} \left[L_{\alpha_T} - M_{\alpha_T} \, b_r \left(\frac{\varphi_T^{(1)}}{H_T^{(1)}}\right) \sin \Lambda \right]$$

$$(A_{21})_T = - M_{\alpha_T} \, b_r \left(\frac{\varphi_T^{(1)}}{H_T^{(1)}}\right) \sin \Lambda \, \cos \Lambda$$

$$(A_{22})_T = M_{\alpha_T} \cos^2 \Lambda$$

$$(A_{23})_T = 0$$

$$(A_{24})_T = M_{\alpha_T} \left(\frac{b_r}{\ell}\right) \cot \Lambda$$

$$(A_{31})_T = 0$$

$$(A_{32})_T = 0$$

$$(A_{33})_T = 0$$

$$(A_{34})_T = 0$$

$$(A_{41})_T = - b_r \left(\frac{\varphi_T^{(1)}}{H_T^{(1)}}\right) \left[L_{\alpha_T} \sin \Lambda + M_{\alpha_T} \left(\frac{b_r}{\ell}\right) \right]$$

$$(A_{42})_T = L_{\alpha_T} \cos \Lambda + M_{\alpha_T} \left(\frac{b_r}{\ell}\right) \cot \Lambda$$

$$(A_{43})_T = 0$$

$$(A_{44})_T = \frac{b_r}{\ell \sin \Lambda} \left[L_{\alpha_T} + M_{\alpha_T} \left(\frac{b_r}{\ell \sin \Lambda}\right) \right]$$

$$(A_{55})_N = (A_{11})_N$$

$$(A_{56})_N = (A_{12})_N$$

$$(A_{57})_N = \frac{1}{\ell} \int_0^\ell \left[\frac{b}{b_r}\right]^2 \left[\left(\frac{x}{\ell}\right) h^{(1)}\right] \left[L_h\right] dx$$

$$- \tan \Lambda \left(\frac{b_r}{\ell^2}\right) \int_0^\ell \left[\frac{b}{b_r}\right]^3 \left[h^{(1)}\right] \left[L_\alpha - \left(\frac{1}{2} + a\right) L_h\right] dx$$

$$(A_{65})_N = (A_{21})_N$$

$$(A_{66})_N = (A_{22})_N$$

$$(A_{67})_N = \frac{1}{\ell} \int_0^\ell \left[\frac{b}{b_r}\right]^3 \left[\left(\frac{x}{\ell}\right) \alpha^{(1)}\right] \left[\frac{1}{2} - \left(\frac{1}{2} + a\right) L_h\right] dx$$

$$- \tan \Lambda \left(\frac{b_r}{\ell^2}\right) \int_0^\ell \left[\frac{b}{b_r}\right]^4 \left[\alpha^{(1)}\right] \left[-\frac{1}{2}\left(\frac{1}{2}+a\right) + M_\alpha - \left(\frac{1}{2}+a\right) L_\alpha + \left(\frac{1}{2}+a\right)^2 L_h\right] dx$$

$$(A_{75})_N = \frac{1}{\ell} \int_0^\ell \left[\frac{b}{b_r}\right]^2 \left[\left(\frac{x}{\ell}\right) h^{(1)}\right] \left[L_h\right] dx$$

$$- \tan \Lambda \left(\frac{b_r}{\ell^2}\right) \int_0^\ell \left[\frac{b}{b_r}\right]^3 \left[h^{(1)}\right] \left[\frac{1}{2} - \left(\frac{1}{2} + a\right) L_h\right] dx$$

$$(A_{76})_N = \frac{1}{\ell} \int_0^\ell \left[\frac{b}{b_r}\right]^3 \left[\left(\frac{x}{\ell}\right) \alpha^{(1)}\right] \left[L_\alpha - \left(\frac{1}{2} + a\right) L_h\right] dx$$

$$- \tan \Lambda \left(\frac{b_r}{\ell^2}\right) \int_0^\ell \left[\frac{b}{b_r}\right]^4 \left[\alpha^{(1)}\right] \left[-\frac{1}{2}\left(\frac{1}{2}+a\right) + M_\alpha - \left(\frac{1}{2}+a\right) L_\alpha + \left(\frac{1}{2}+a\right)^2 L_h\right] dx$$

$$(A_{77})_N = \frac{1}{\ell} \int_0^\ell \left[\frac{b}{b_r}\right]^2 \left[\frac{x}{\ell}\right]^2 \left[L_h\right] dx - \tan \Lambda \left(\frac{b_r}{\ell^2}\right) \int_0^\ell \left[\frac{b}{b_r}\right]^3 \left[\frac{x}{\ell}\right] \left[L_\alpha - \left(\frac{1}{2}+a\right) L_h\right] dx$$

$$- \tan \Lambda \left(\frac{b_r}{\ell^2}\right) \int_0^\ell \left[\frac{b}{b_r}\right]^3 \left[\frac{x}{\ell}\right] \left[\frac{1}{2} - \left(\frac{1}{2} + a\right) L_h\right] dx$$

$$+ \tan^2 \Lambda \left(\frac{b_r^2}{\ell^3}\right) \int_0^\ell \left[\frac{b}{b_r}\right]^4 \left[-\frac{1}{2}\left(\frac{1}{2}+a\right) + M_\alpha - \left(\frac{1}{2}+a\right) L_\alpha + \left(\frac{1}{2}+a\right)^2 L_h\right] dx$$

$$(A_{55})_S = (A_{11})_S$$

$$(A_{56})_S = (A_{12})_S = 0$$

$$(A_{57})_S = (A_{14})_S$$

$$(A_{65})_S = (A_{21})_S$$

$$(A_{66})_S = (A_{22})_S = 0$$

$$(A_{67})_S = (A_{24})_S = 0$$

$$(A_{75})_S = \int \tan \Lambda \left(\frac{b_r}{\ell}\right)\left(\frac{V_N}{b_r \omega}\right)\int_o^\ell \left[\frac{b}{b_r}\right]^2 \left[\left(\frac{x}{\ell}\right)\left(\frac{\varphi^{(1)}}{H_T^{(1)}}\right)\right]\left[L_h\right] dx$$

$$- \int \tan^2 \Lambda \left(\frac{b_r}{\ell}\right)^2 \left(\frac{V_N}{b_r \omega}\right)\int_o^\ell \left[\frac{b}{b_r}\right]^3 \left[\frac{\varphi^{(1)}}{H_T^{(1)}}\right]\left[\frac{1}{2}-\left(\frac{1}{2}+o\right)L_h\right] dx$$

$$(A_{76})_S = 0$$

$$(A_{77})_S = -j\tan \Lambda \left(\frac{b_r}{\ell^2}\right)\left(\frac{V_N}{b_r \omega}\right)\int_o^\ell \left[\frac{b}{b_r}\right]^2\left[\frac{x}{\ell}\right]\left[L_h\right] dx$$

$$+ \int \tan^2 \Lambda \left(\frac{b_r^2}{\ell^3}\right)\left(\frac{V_N}{b_r \omega}\right)\int_o^\ell \left[\frac{b}{b_r}\right]^3\left[\frac{1}{2}-\left(\frac{1}{2}+o\right)L_h\right] dx$$

Refer to p. 86 for L_{α_T}

$$(A_{55})_T = (A_{11})_T$$

$$(A_{56})_T = (A_{12})_T$$

$$(A_{57})_T = 0$$

$$(A_{65})_T = (A_{21})_T$$

$$(A_{66})_T = (A_{22})_T$$

$$(A_{67})_T = 0$$

$$(A_{75})_T = -L_{\alpha_T} b_r \left(\frac{\varphi_T^{(1)}}{H_T^{(1)}}\right) \sin \Lambda$$

$$(A_{76})_T = L_{\alpha_T} \cos \Lambda$$

$$(A_{77})_T = 0$$

F. Tip Pod Aerodynamic Effects

$$L\alpha_T = \frac{L}{\pi \rho \, b_r^3 \omega^2 \ell \alpha_P}$$

$$M\alpha_T = \frac{M_{e.a.}}{\pi \rho \, b_r^4 \omega^2 \ell \alpha_P}$$

where

$$\alpha_P = \frac{H_T^{(p)}}{\ell \sin\Lambda} + H_T^{(\alpha)} \cos\Lambda - \varphi_T^{(1)} \sin\Lambda = \text{angle of attack of the tip pod}$$

about an axis normal to the tip pod centerline at the elastic axis

$L =$ lift on the tip pod, in lb.

$M_{e.a.} =$ aerodynamic moment on the tip pod about an axis normal to the tip pod centerline at the elastic axis, in lb.-in.

Tip Pod Configuration	$L\alpha_T$	$M\alpha_T$
Case 3	$-0.0340(V_N/b_r\omega)^2$ -0.195 $-0.0791j(V_N/b_r\omega)$	$0.1575(V_N/b_r\omega)^2$ $+0.691$ $-0.0186j(V_N/b_r\omega)$
Case 4	$-0.0340(V_N/b_r\omega)^2$ -0.248 $-0.0883j(V_N/b_r\omega)$	$0.1691(V_N/b_r\omega)^2$ $+0.857$ $-0.0186j(V_N/b_r\omega)$

APPENDIX II

ON ANTISYMMETRIC NODAL LINES

For wings with heavy tip pods the first two coupled antisymmetric vibration modes may be determined quite accurately by considering only three uncoupled degrees of freedom: rigid body roll, first uncoupled cantilever bending, first uncoupled cantilever torsion.

It is noted in Section VI of the body of this report that the chordwise location of the point of intersection of the two nodal lines, corresponding to these two coupled modes for a particular configuration, bears some important relationship to the critical flutter speed of that configuration. It is obviously of interest to determine what basic mechanical properties of the wing are involved in locating this intersection point at its particular chordwise position. It is shown in this Appendix that, to a first approximation, this intersection point is primarily dependent on the location of the tip pod c.g.

The equation of motion for the roll degree of freedom is:

$$m_{75}\left[\frac{H_T^{(1)}}{b_r}\right] + m_{76}\left[H_T^{(\alpha)}\right] + m_{77}\left[1-\left(\frac{\omega_r}{\omega}\right)^2\right]\left[\frac{H_T^{(r)}}{b_r}\right] = 0 \tag{1}$$

or

$$\left[H_T^{(1)}\right] + \frac{m_{76}}{m_{75}}\,b_r\left[H_T^{(\alpha)}\right] + \frac{m_{77}}{m_{75}}\left[1-\left(\frac{\omega_r}{\omega}\right)^2\right]\left[H_T^{(r)}\right] = 0 \tag{2}$$

where, from Appendix I, p. 79,

$$m_{75} = \frac{1}{\pi\rho\,b_r^2\,\ell}\left\{W_T - S_T\left[\frac{\varphi_T^{(1)}}{H_T^{(1)}}\right]\sin\Lambda + \int_0^\ell\left[W\left(\frac{x}{\ell}\right) - \frac{\tan\Lambda}{\ell}S_\alpha\right]\left[h^{(1)}(x)\right]dx\right\}$$

$$m_{76} = \frac{1}{\pi\rho\,b_r^3\,\ell}\left\{S_T\cos\Lambda + \int_0^\ell\left[S_\alpha\left(\frac{x}{\ell}\right) - \frac{\tan\Lambda}{\ell}I_\alpha\right]\left[\alpha^{(1)}(x)\right]dx\right\}$$

$$m_{77} = \frac{1}{\pi\rho\,b_r^2\,\ell}\left\{W_T + \frac{I\varphi}{(\ell\cos\Lambda)^2} + \int_0^\ell\left[W\left(\frac{x}{\ell}\right)^2 - \frac{2\tan\Lambda}{\ell}S_\alpha\left(\frac{x}{\ell}\right) + \frac{\tan^2\Lambda}{\ell^2}I_\alpha\right]dx\right\},$$

and $\left(\dfrac{\omega_r}{\omega}\right)^2 \leqslant 0.09$ for the test cases. Thus, in first approximation,

$$\frac{m_{76}}{m_{75}} \approx \frac{S_T \cos \Lambda}{W_T b_r} = \eta_T = \text{non-dimensional tip pod c.g. location measured}$$

normal to the elastic axis,

$$\frac{m_{77}}{m_{75}} \approx 1 + \frac{l_{\varphi}}{W_T \ell^2 \cos^2 \Lambda} = \lambda ,$$

so that

$$\left[H_T^{(1)} \right] + \eta_T b_r \left[H_T^{(\alpha)} \right] + \lambda \left[H_T^{(r)} \right] = 0 . \tag{3}$$

Therefore

$$H_T^{(r)} = - \frac{H_T^{(1)} + \eta_T b_r H_T^{(\alpha)}}{\lambda} . \tag{4}$$

At any spanwise station, x, along the elastic axis, the perpendicular distance from the elastic axis to the nodal line in either of the two coupled modes is given by

$$\begin{aligned}
\bar{y}_i(x) &= - \frac{H_{T_i}^{(1)} h^{(1)}(x) + H_{T_i}^{(r)} h^{(r)}(x)}{H_{T_i}^{(\alpha)} \alpha^{(1)}(x) - \dfrac{\tan \Lambda}{\ell} H_{T_i}^{(r)}} \\[2ex]
&= - \frac{\left[\lambda h^{(1)}(x) - h^{(r)}(x) \right] H_{T_i}^{(1)} - \eta_T b_r h^{(r)}(x) H_{T_i}^{(\alpha)}}{\dfrac{\tan \Lambda}{\ell} H_{T_i}^{(1)} + \left[\lambda \alpha^{(1)}(x) + \dfrac{\tan \Lambda}{\ell} \eta_T b_r \right] H_{T_i}^{(\alpha)}} .
\end{aligned} \tag{5}$$

The value of x, i.e. $x = x_0$, for which $\bar{y}_1(x_0) = \bar{y}_2(x_0)$, is the spanwise location of the intersection point of the two coupled mode nodal lines.

~~CONFIDENTIAL~~

Thus

$$\bar{y}_1(x_o) = \bar{y}_2(x_o) = -\frac{\left[\lambda h^{(1)}(x_o) - h^{(r)}(x_o)\right] H_{T_1}^{(1)} - \eta_T b_r h^{(r)}(x_o) H_{T_1}^{(\alpha)}}{\frac{\tan\Lambda}{\ell} H_{T_1}^{(1)} + \left[\lambda \alpha^{(1)}(x_o) + \frac{\tan\Lambda}{\ell} \eta_T b_r\right] H_{T_1}^{(\alpha)}}$$

$$= -\frac{\left[\lambda h^{(1)}(x_o) - h^{(r)}(x_o)\right] H_{T_2}^{(1)} - \eta_T b_r h^{(r)}(x_o) H_{T_2}^{(\alpha)}}{\frac{\tan\Lambda}{\ell} H_{T_2}^{(1)} + \left[\lambda \alpha^{(1)}(x_o) + \frac{\tan\Lambda}{\ell} \eta_T b_r\right] H_{T_2}^{(\alpha)}} ,$$

from which

$$-\frac{\tan\Lambda}{\ell} \eta_T b_r h^{(r)}(x_o) \left[H_{T_2}^{(1)} H_{T_1}^{(\alpha)} - H_{T_1}^{(1)} H_{T_2}^{(\alpha)}\right]$$

$$= \left[\lambda \alpha^{(1)}(x_o) + \frac{\tan\Lambda}{\ell} \eta_T b_r\right]\left[\lambda h^{(1)}(x_o) - h^{(r)}(x_o)\right]\left[H_{T_2}^{(1)} H_{T_1}^{(\alpha)} - H_{T_1}^{(1)} H_{T_2}^{(\alpha)}\right] .$$

Therefore, $\bar{y}_1(x_o) = \bar{y}_2(x_o)$ when

$$\left[\lambda h^{(1)}(x_o) - h^{(r)}(x_o)\right] = -\frac{\eta_T \tan\Lambda \left(\frac{b_r}{\ell}\right) h^{(r)}(x_o)}{\left[\lambda \alpha^{(1)}(x_o) + \eta_T \tan\Lambda \left(\frac{b_r}{\ell}\right)\right]} , \qquad (6)$$

and from equation (6), the spanwise location of the intersection point of the two coupled mode nodal lines, x_o , is determined. By inserting equation (6) into equation (5), the chordwise location of the intersection point, in first approximation, is found to be

$$\bar{y}(x_o) = +\frac{\eta_T b_r h^{(r)}(x_o)}{\lambda \alpha^{(1)}(x_o) + \eta_T \left(\frac{b_r}{\ell}\right) \tan\Lambda} , \qquad (7)$$

or

$$\bar{y}(x_o) = +\frac{\eta_T b_r \left(\frac{x_o}{\ell}\right)}{\left[1 + \frac{I\varphi}{W_T \ell^2 \cos^2\Lambda}\right] \alpha^{(1)}(x_o) + \eta_T \left(\frac{b_r}{\ell}\right) \tan\Lambda} . \qquad (8)$$

Thus there is a fundamental dependence of $\bar{y}(x_o)$ on the tip pod c.g. location, η_T .

APPENDIX III

TABLE 10

SUMMARY OF MODEL CONFIGURATIONS
AND EXPERIMENTAL DATA

CASE	W_T lb.	S_T lb.-in.	I_T lb.-in.²	η_T	η_B	$\left(\dfrac{\omega h}{\omega_\alpha}\right)_{cant}$	n_1 cps	n_2 cps	V_{cr} mph	n_{cr} cps	$\dfrac{V_N}{b_r\omega}$	$\dfrac{V_N}{b_r(\omega_\alpha)_{cant}}$
						Cantilever Cases						
3	42.7	- 44.5	23040	-0.093	0.589	0.52	1.4	2.9	124	2.3	14	11.5
4	51.2	- 423	39520	-0.742	0.352	0.67	1.4	2.1	89	1.9	12	10.8
4A	61.0	- 412	46160	-0.606	0.430	0.67	1.3	1.9	90	1.7	13	12.1
10	33.2	- 320	15050	-0.866	-0.262	0.54	1.8	3.3	130	3.0	11	9.8
13	38.9	- 135	18770	-0.312	0.349	0.51	1.5	3.0	124	2.5	12	10.4
				Symmetric Cases: $W_F = 157.1$ lb., $S_F = +22$ lb.-in., $I_F = 88760$ lb.-in.²								
3	42.7	- 44.5	23040	-0.093	0.589	0.52	2.4	3.0	150	2.4	16	13.9
4	51.2	- 423	39520	-0.742	0.352	0.67	2.2	2.4	138	1.9	18	16.7
4A	61.0	- 412	46160	-0.606	0.430	0.67	2.0	2.3	139	1.8	19	18.6
12	34.9	- 214	17240	-0.551	0.146	0.53	2.5	3.1	120	2.8	11	9.6
22	36.3	- 767	31610	-1.898	-1.212	0.88	2.3	3.1	160	2.2	18	18.0
22A	50.3	-1257	48690	-2.245	-1.932	1.00	1.8	3.0	Above 257 mph			>34.6
33	52.6	+ 416	19820	+0.710	0.902	0.40	2.3	3.7	Above 155 mph			>13.3
100	24.2	- 267	10500	-0.991	-0.436	0.53	2.8	4.0	230	3.7	16	14.4
				Symmetric Case: $W_F = 155.7$ lb., $S_F = -1287$ lb.-in., $I_F = 88660$ lb.-in.²								
33A	52.6	+ 416	19820	+0.710	0.902	0.40	2.5	3.6	165	3.2	13	14.2
				Symmetric Case: $W_F = 155.7$ lb. - Pitch Locked								
33B	52.6	+ 416	19820	+0.710	0.902	0.40	1.3	3.6	175	2.6	17	15.1
				Symmetric Case: $I_F = 88660$ lb.-in.² - Translation Locked								
33C	52.6	+ 416	19820	+0.710	0.902	0.40	2.3	3.5	151.5	2.0	19	13.0
				Antisymmetric Cases: $I_\phi = 17130$ lb.-in.²								
15B	46.5	+ 166	21890	+0.321	0.780	0.46	2.1	5.6	107	1.7	16	9.7
18-1	41.2	- 468	12040	-1.020	-0.780	0.46	3.9	5.6	Above 221 mph			>14.9
				Antisymmetric Cases: $I_\phi = 33130$ lb.-in.²								
3	42.7	- 44.5	23040	-0.093	0.589	0.52	2.1	4.5	124	1.8	17	11.5
4	51.2	- 423	39520	-0.742	0.352	0.67	1.7	4.2	174	1.7	26	21.1
10	33.2	- 320	15050	-0.866	-0.262	0.54	2.8	4.6	Above 238 mph			>17.9
13	38.9	-.135	18770	-0.312	0.349	0.51	2.3	4.5	147	2.1	18	12.3
15	46.5	+ 166	21890	+0.321	0.780	0.46	---	---	108	1.7	16	9.8
18	41.2	- 468	12040	-1.020	-0.780	0.46	3.6	4.8	Above 271 mph			>18.2
19	41.2	- 282	8350	-0.614	-0.350	0.36	3.4	5.1	Above 229 mph			>12.9
19A	55.6	+ 52	15010	+0.084	0.410	0.37	2.3	4.7	132	1.8	18	9.9
22	36.3	- 767	31610	-1.898	-1.212	0.88	2.6	4.5	Above 262 mph			>28.4
28-1	55.6	- 133	18700	-0.215	0.250	0.43	2.2	4.5	137	1.9	18	11.5
31	21.8	- 180	7350	-0.742	-0.250	0.46	3.6	5.2	243	5.0	12	13.0
				Antisymmetric Cases: $I_\phi = 41470$ lb.-in.²								
18-2	41.2	- 468	12040	-1.020	-0.780	0.46	3.4	4.6	Above 242 mph			>16.3
28	55.6	- 133	18700	-0.215	0.250	0.43	2.2	4.2	147	1.8	21	12.3
				Antisymmetric Cases: $I_\phi = 57200$ lb.-in.²								
15A	46.5	+ 166	21890	+0.321	0.780	0.46	1.9	4.1	119	1.6	19	10.5
30	51.0	- 635	14690	-1.118	---	---	3.1	4.3	Above 265 mph			---